ABSTRACT

Title of dissertation: USING KINEMATIC VARIABLES TO EXTRACT INFORMATION FROM SEMI-INVISIBLE DECAYS OF HEAVY PARTICLES AT HADRON COLLIDERS

Doojin Kim, Doctor of Philosophy, 2013

Dissertation directed by: Professor Kaustubh S. Agashe
Department of Physics

We examine the ways of extracting information from semi-invisible decays of (new) heavy particles at hadron colliders, i.e., such heavy particles are assumed to decay into visible/Standard Model (SM) particles and invisible particles. As a concrete realization, we employ the models with the *stable* weakly interacting massive particle (WIMP), a well-motivated dark matter (DM) candidate. By definition, dark matter is *not* seen by the detectors, i.e., invisible. Typically, stability of dark matter is ensured by introducing a new (unbroken) symmetry under which the DM is *non*-trivially charged while the SM particles are *un*charged. Also, many new physics models contain other heavier particles which are charged under the same symmetry so that such heavier particles must decay into (invisible) DM particles along with the relevant visible/SM particles.

In particular, we study how to determine the masses of DM and heavy particles and the nature of the above-mentioned DM stabilization symmetries. For this

purpose we take three kinematic variables as the main toolkits. We first discuss the distribution of the invariant mass formed by the visible part in the associated decays. As the second variable, we include the invisible part in forming the invariant mass. Because we are not aware of the longitudinal momentum of invisible particles, such a quantity is constructed in the plane transverse to the beam pipe, which is therefore called "transverse" mass. This is typically suitable for a singly produced heavy particle. Since the DM stabilization symmetries lead to pair-production of heavier particles, we here consider the "stransverse/M_{T2}" type variable, a simple generalization of the transverse mass. Finally, we consider the energy spectrum of visible particle(s), which is *not* Lorentz-invariant at all even under longitudinal boosts. The relevant strategy is predicated upon the new observations that we shall make about physical implications of the peak position in such an energy spectrum. We emphasize that the relevant methods using the three observables are *complementary* to one another.

USING KINEMATIC VARIABLES TO EXTRACT INFORMATION FROM SEMI-INVISIBLE DECAYS OF HEAVY PARTICLES AT HADRON COLLIDERS

by

Doojin Kim

Dissertation submitted to the Faculty of the Graduate School of the
University of Maryland, College Park in partial fulfillment
of the requirements for the degree of
Doctor of Philosophy
2013

Advisory Committee:
Professor Kaustubh S. Agashe, Chair/Advisor
Professor Zackaria Chacko
Professor Nicholas J. Hadley
Professor M. Coleman Miller, Dean's representative
Professor Rabindra N. Mohapatra

Dedication

To my dear and loving dad who passed away in 2012

Acknowledgments

I extend my sincere gratitude to all the people who made this thesis possible.

Above all, I would like to thank my advisor, Professor Kaustubh Agashe for providing me with a precious opportunity to do research on intriguing and challenging projects over the past five years. He has always made himself available for not only unstinting help and advice in research but the wisdom of life. It has been a great pleasure to work with and learn from such an extraordinary individual.

I also would like to thank Professor Konstantin Matchev at the University of Florida for giving me an invaluable chance to collaborate with him and people there. He has been ready to discuss physics and I have learnt different perspective in physics to enrich my physical insights. Thanks are due to Professor Zackaria Chacko, Professor Nicholas Hadley, Professor Coleman Miller and Professor Rabindra Mohapatra for agreeing to be on my thesis committee and for sparing their invaluable time reviewing the manuscript.

All my collaborators, Professor Hooman Davoudiasl, Dr. Aleksandr Azatov, Dr. Chien-Yi Chen, Dr. Won Sang Cho, Dr. Roberto Franceschini, Dr. Andrey Kats, Dr. Myeonghun Park, Dr. Manuel Toharia, Dr. Devin Walker, Dr. Lijun Zhu and Kyle Wardlow have helped my research in many ways and deserve a special mention. In particular, the post-doctoral fellows cannot dedicate more effort to share their ideas, insights and techniques in various aspects with me. In addition, my interaction with Steven Cowen, Dr. Bhupal Dev, Hongsuk Kang, Rashmish Mishra, Matthew Severson and Dr. Young Soo Yoon has been very fruitful in

inspiring me.

I owe my deepest thanks to my family - my mother, father and wife who have always stood by me and guided me through my career, and have pulled me through against impossible odds at times. Special thanks are due to my twin boys, who were born last year, for cheering me with their angel smile whenever discouraged.

I would like to express my gratitude to the Maryland Center for Fundamental Physics for all accommodation and assistance in my graduate work. I also would like to acknowledge financial support from NSF Grant No. PHY-0968854 and the LHC Theory Initiative graduate fellowship that is funded through NSF Grant No. PHY-0969510 for some of the projects discussed herein.

It is impossible to remember all, and I apologize to those whom I have inadvertently left out.

Lastly, thank you all and thank God!

Table of Contents

List of Figures

List of Abbreviations

α	alpha
β	beta
γ	gamma
θ	theta
λ	lambda
ν	nu
χ	chi

DM	Dark Matter
WIMP	Weakly Interacting Massive Particle
SM	Standard Model
LHC	Large Hadron Collider
SUSY	Supersymmetry
KK	Kaluza-Klein
GUT	Grand Unified Theory

Chapter 1: Introduction

1.1 Motivation

There is a tremendous amount of evidence for the existence of dark matter (DM) in the universe [1]. A consensus picture of the nature of such a particle is provided by a lot of astrophysical and cosmological observations and the relevant experimental results. A viable DM candidate must be electrically neutral and colorless, non-relativistic, stable and give rise to the measured relic abundance of $h^2\Omega_{DM} = 0.1131 \pm 0.0034$ [2]. Additionally, a Weakly Interacting Massive Particle (WIMP) – with a mass being of order the weak scale – is a very well-motivated paradigm since it approximately has the correct relic density upon thermal freeze-out [1].

Moreover, such a DM candidate also often arises in extensions of the Standard Model (SM), most of which are motivated primarily as solutions to other problems in the SM such as the Planck-weak hierarchy problem. Typically, such extensions contain extra particles at the weak scale, some of which are charged under a new unbroken symmetry. Since SM particles are assumed neutral under such a symmetry in most cases, the lightest of such new particles cannot decay further into lighter particles to end up with the lightest stable particles like electron, proton, photon,

neutrino and so on. If the above-mentioned lightest particle is further SM-neutral, then it becomes a stable DM candidate in itself. In this sense, such a new symmetry is called the dark matter stabilization symmetry. In addition, if such stable WIMP dark matter is an ingredient for an extension of the SM, then it is likely to have (weak) interactions with SM particles. Therefore, This enables us to test the WIMP paradigm by direct detection via scattering off nuclei or indirect detection via its annihilation products.

Such a scenario also makes the idea of DM amenable for testing at the high-energy colliders, which is the main focus in this thesis. At a minimum, it is possible to produce DM particles directly at colliders, but then this does not leave any visible signature since (by construction) the DM particles will simply escape the detectors without interactions. We instead pay attention to a different scenario. As discussed above, many new physics models having stable WIMPs as the DM candidate also contain heavier particles which are also charged under the DM stabilization symmetry. Unlike the DM particle, however, they can have non-trivial color, electric or both charges, i.e., they are typically SM-*charged*. Therefore, such heavier particles (a.k.a. "mother" particles or "DM partners") can be produced first in collisions of SM particles via SM gauge interactions.[1] They then must decay into DM particle(s) with the relevant visible state due to the symmetry introduced in the models. In this context, the relevant events that we investigate are characterized by the visible part and the (large) missing transverse energy/momentum (MET) which is carried

[1] As opposed to this case, the production of DM only requires new interaction(s) because DM is assumed SM-neutral.

by invisible particle(s), and such a MET signature could be taken as *evidence* of the DM existence. But again it should be emphasized that we do not preclude invisible particles other than the DM candidates, i.e., the techniques/argument which we shall develop throughout this thesis are still applicable to the decay processes with generic invisible particles.[2]

1.2 Determination of dark matter properties

Once dark matter particles are produced at colliders, for example, the Large Hadron Collider (LHC), and in turn discovered, then one of the natural steps for studying dark matter is to determine its various properties such as mass, DM stabilization symmetries, spin, coupling constants, and so on, first two of which are main interests here.

1.2.1 Mass measurement

As obvious from the astrophysical and cosmological observations and the relevant theory arguments, the DM particle must have a non-zero mass, for example, $m_{DM} \sim 100$ GeV for the WIMPs as mentioned earlier so that it is important to measure the mass of the DM particle in experiment. To date, a large amount of effort has been made in order to determine the mass of the DM in the relevant processes involving the dark matter [4–39]. See also the reference [40] for a general review

[2]For example, a certain type of invisible particles could be collider-stable in that they decay *outside* the detectors so that effectively they behave like the DM particles in the relevant signals. See for example the reference [3].

on mass measurement. Typically, the mass measurement in most of the relevant studies involves reconstructing the associated decay chains so that it is also possible to determine the masses of the mother particle and the intermediate particle(s) as well as that of the DM particles. In this sense, we do not restrict ourselves to determination of the DM mass in this thesis. We again emphasize that the argument in mass measurement is, in general, applicable to the cases with any type of invisible particles including dark matter.

1.2.2 Distinction of dark matter stabilization symmetries

As briefly discussed earlier, in order to prevent the (massive) DM particle from decaying into lighter particles, the relevant models typically employ a new symmetry. However, surprisingly enough, most of the collider studies of the DM assume a Z_2/parity type symmetry to stabilize the DM candidate (henceforth called Z_2 models). This is because most of the popular models constructed under the framework of supersymmetry (SUSY), little Higgs and extra dimensions [41–47] ensure the stability of the DM particle by introducing a Z_2 stabilization symmetry. More importantly, these models have served as guide to expected signatures of dark matter at the LHC [48, 49].

In this thesis, we emphasize that any discrete or continuous global symmetry can be employed as the DM stabilization symmetries.[3] Furthermore, since all fundamental particles in nature are defined by the way in which they transform under

[3]Gauge symmetries alone cannot be used to stabilize dark matter. See the discussion in the reference [50]. For example of models with a non-Z_2 symmetry, see also references [51–53].

various symmetries, most of the popular (Z_2) models actually consider only one type of the DM candidate. It is therefore critical to determine *experimentally*, i.e., without any theoretical bias, the nature of the symmetry that stabilizes dark matter. In this context, we study how to distinguish models in which the DM becomes stable by a Z_2 discrete symmetry from ones in which the DM becomes stable by other symmetries. For definiteness and simplicity, we have focused on the models to introduce a Z_3 type symmetry (henceforth called Z_3 models) as the DM stabilization symmetry. However, we emphasize that the techniques in this thesis can be generalized to distinguishing most of the other DM stabilization symmetries from the parity type symmetry.

1.3 Z_3 symmetry: primer

Since the Z_3 symmetry is not as familiar as the Z_2 symmetry, we here briefly review some key features/observations to be used especially for distinguishing DM stabilization symmetries. As usual, Z_3 symmetry can be defined by the relevant transformation rule under which a particle/field ϕ transforms as

$$\phi \to \phi \exp\left(\frac{2\pi i q}{3}\right) \tag{1.1}$$

where Z_3 quantum number $q = 0$ (i.e., Z_3-neutral) or $q = +1, +2$ (non-trivial Z_3-charged). Suppose that the lightest of the Z_3-charged particles (labeled ϕ_0) has charge $q = +1$ (a similar argument goes through for charge $q = +2$ for ϕ_0). Clearly, its anti-particle ($\bar{\phi}_0$) has a (different) charge $q = -1$, which is equivalent to $q = +2$, and has the same mass as ϕ_0. Then, solely based on Z_3 charge conservation, all

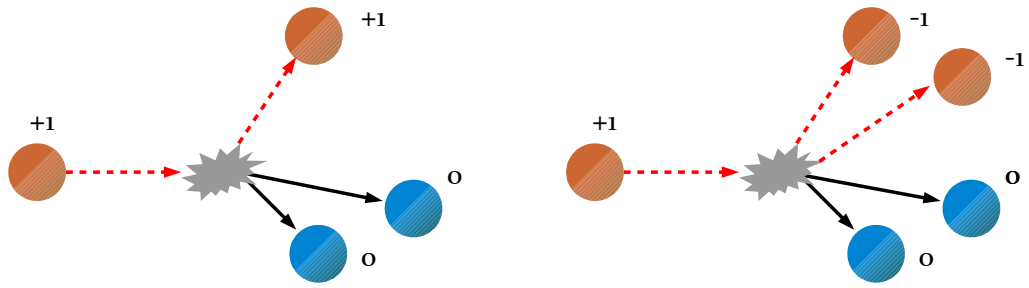

Figure 1.1: Two possible decay processes of a Z_3-charged heavier particles. The numbers denote Z_3 quantum numbers for each particle. The red dashed lines denote the particles having a non-trivial Z_3 charge whereas the black solid lines denote the particles having a neutral Z_3 charge.

other (heavier) Z_3-charged particles can decay into this lightest Z_3-charged particle (in addition to Z_3-neutral particles including SM ones). To be explicit, a heavier Z_3-charged particle with charge $q = +1$ can decay into either a single ϕ_0 or *two* $\bar{\phi}_0$'s along with Z_3-neutral particles (See Figure 1.1). Taking the CP conjugate of the preceding statement, we see that a heavier Z_3-charged particle with the other type of charge, namely $q = +2$, is allowed to decay into *two* ϕ_0's or a single $\bar{\phi}_0$. Of course, ϕ_0 cannot decay and thus is the (single) DM candidate in this theory. We denote this DM particle and its anti-particle by DM and $\overline{\text{DM}}$, respectively, throughout this thesis although we do not make this distinction in the text since DM and anti-DM particles are still degenerate.[4]

One noteworthy observation is that in Z_2 models it is possible to have only the diagram in the left-hand side of Figure 1.1, i.e., the decay of a mother particle into a

[4]Of course, which of the two particles is denoted as anti-DM is a matter of convention. Also, as a corollary, the DM particle should be a Dirac fermion or a complex scalar in a Z_3 model.

single dark matter particle along with the relevant visible state due to Z_2 quantum number conservation (again assuming that such a symmetry is not broken). In terms of the visible final state, of course, the left- and the right-hand sides in Figure 1.1 seem to be the same because one or two DM particles there are *not* visible in any case. Thus at the first glance it seems that there is "no" hope for distinction between them. Nevertheless, this simple difference in the number of DM particles remarkably does leave an impact on the kinematic variables to be discussed in this thesis so that determining the DM properties, in particular the DM stabilization symmetries, becomes more feasible.

1.4 Signal processes and kinematic variables

1.4.1 Signal processes

As discussed so far, in order for dark matter to become stabilized a certain new unbroken symmetry is needed, and this symmetry requires that the particles charged under this symmetry should be *pair*-produced since typically known particles/SM particles are assumed *un*charged under this new symmetry. Considering this requirement, the minimal situation that involves DM particles is the pair-production of DM particles. However, this is not interesting as indicated earlier because by construction DM particles are very unlikely to leave their visible trace in the relevant detectors so that nothing would be observed. Therefore, to ensure a non-trivial visible signature mother particles/DM partners are pair-produced first, and then each

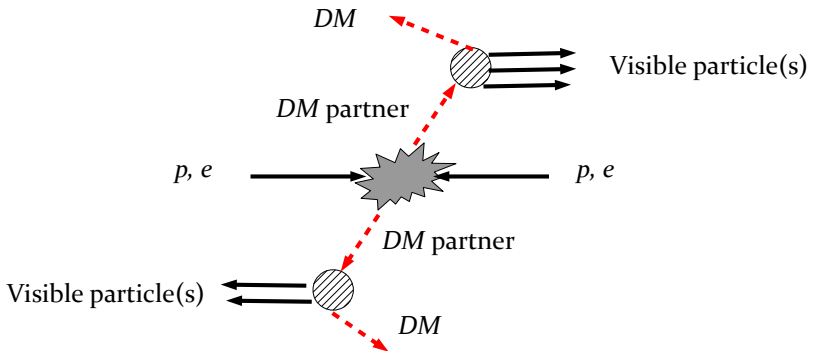

Figure 1.2: A schematic signal process at colliders.

of them should decay into DM particle(s) plus the associated visible particle(s).[5]

Figure 1.2 schematically demonstrates a possible signal process which would occur in the relevant collider experiment. In this picture, the blobs denote the intermediate states which might involve several new particles that are on shell or off shell depending on models. Here (and henceforth) *off*-shell intermediate particles typically imply that they are heavier than their mother particle unless specified. Although it is shown that each DM partner ends up with a single DM particle in Figure 1.2 for simplicity, we do not restrict our argument later to this simplest possibility, i.e., two DM particles can appear in each decay chain.

[5]Of course, as the next simplest situation one can consider the directly pair-produced DM particles along with extra jet/photon radiated from the initial state so that the resultant signal is featured by a large missing energy stemming from the (invisible) DM particles, i.e., this possibility also leaves a similar collider signature to the one we study here. But we do not consider this case in this thesis because of the difficulty in mass measurement.

1.4.2 Kinematic variables: the main toolkits

In order to analyze the signal processes described in the previous section and extract the physical properties of new particles including dark matter, suitable variables must be introduced. For this purpose we adopt three kinematic variables: invariant mass distribution, stransverse mass/M_{T2} distribution, and the peak position in the energy distribution. We delineate the main idea behind using these variables item by item.

1.4.2.1 Invariant mass

Given any Lorentz four momentum, the invariant mass can be obtained simply by taking the Lorentzian magnitude of it, and the resultant quantity is invariant by definition. This invariance is useful in the sense that the associated values are fixed in any

For invariant mass, the main strategy is that the final states and the "topology" of the decay of a mother particle are (in part) determined by the DM stabilization symmetry. Thus reconstructing the visible parts of these decay chains will allow us to differentiate a model of DM stabilized with a non-Z_2 symmetry from one where DM is stabilized with a Z_2 symmetry. The conclusions seem generic for most stabilization symmetries that are not parity symmetries as mentioned before; however, again for definiteness, we focus on the case of a Z_3 symmetry. When illustrating the signatures we will generically refer to any model stabilized with Z_2 and Z_3 stabilization symmetry simply as Z_2 and Z_3 models, respectively.

More specifically to see differences between Z_2 and Z_3 models, we focus on the *kinematic edges* and *shapes* of invariant mass distributions of the SM particles resulting from the decay of a *single* mother particle charged under the SM and the DM stabilization symmetries. We note the possibility of one or two DM particles in each decay chain being allowed by the Z_3 symmetry along with SM particles which can, in general, be different in the two decay chains as discussed earlier. Whereas, in Z_2 models, decays of a mother particle in the given SM final state cannot have two DM particles in the decay chain and hence typically has only one DM particle. Thus,

- If all the intermediate particles in the two decay chains are *off-shell* and the SM particles in the two decay chains are the *same*, then we show that there are two Z_3 kinematic edges in the invariant mass distribution of this SM final state at approximately $M_{\rm mother} - m_{\rm DM}$ and $M_{\rm mother} - 2\,m_{\rm DM}$. Models with Z_2 stabilized dark matter have only one endpoint approximately given by $M_{\rm mother} - m_{\rm DM}$.

In the case of on-shell intermediate particles, the decay of such a mother in a Z_3 model can similarly result in double edges due to the presence of one or two DM in the final state. However, in this case the endpoint also depends on the masses of intermediate particles. Thus it is possible to obtain multiple edges even from decay of a single mother particle in a Z_2 model due to different intermediate particles to the same final state. Hence, multiple edges are not a robust way to distinguish between Z_3 and Z_2 symmetries in the case of on-shell intermediate particles. For the case of on-shell intermediate particles, we thus use shapes of invariant mass

distributions instead of edges. In particular,

- We find a unique decay chain topology with two SM particles separated by a DM particle (along with another DM at the end of the decay chain) which is generally present for Z_3 models but absent for the Z_2 case. Based on pure kinematics/phase space, this topology leads to a "cusp" (i.e., derivative discontinuity) in the invariant mass distribution of the SM particles.

The idea of using the invariant mass variable can be generalized to the cases in which a heavy resonance decays into N_v visible particles and N_χ invisible particles. Without making any assumption on the underlying physics there naturally arise several basic questions: 1) How many invisible particles are in the final state? 2) What are their masses? 3) What is the exact topology (i.e., Feynman diagram) of such a decay process: are there any intermediate resonances, and if so, what are their masses?

In this context, here we do not hypothesize the specific decay topology including the number of invisible particles. Also we shall concentrate on the region near the peak rather than the kinematic endpoint of the invariant mass distributions, where the available statistics can be rather poor (in the sense that the most populated bins are rarely near the kinematic endpoint). The main idea is to derive the analytic formulae necessary to analyze the full shape of the invariant mass distributions of the visible particles including the location of the peak. For definiteness and simplicity, we begin this program of research with the simplest and most challenging case of $N_v = 2$ along with $N_\chi = 1, 2$. We shall then demonstrate how the relevant

results can be used to determine: 1) the number of missing particles, 2) their masses, and 3) the associated event topology.

1.4.2.2 Stransverse mass/M_{T2}

The basic idea behind distinguishing Z_3 from Z_2 models by utilizing stransverse mass/M_{T2} is again (like the invariant mass) that a

- *single* mother charged under a Z_3 symmetry is allowed (based simply on the symmetry) to decay into *one* or *two* DM candidates.

This is to be contrasted with the fact that mother particles charged under a Z_2 symmetry have only *one* DM candidate in the final state. As discussed in the previous section, decays of a *single* Z_3-charged mother particle generate a "double edge" in the invariant mass distribution of the *visible* (SM) particles. This is with the condition that the intermediate particles in the decay chains are off-shell and that the decay chains with one and two DM contain identical SM particles. For the case of on-shell intermediate particles, this invariant mass distribution has a "cusp" for certain decay topology (with two DM) of a Z_3 mother particle. In all, the analysis with the invariant mass distribution is focused on new features in observables from a single decay chain only.

Instead we consider the total inclusive event in order to glean even more information, recalling that there must be two such mother particles present. For example, consider the case where there is only one visible (SM) particle in the decay chain of a mother particle. Constructing the invariant mass of the visible particle of this decay

chain, as per the analysis using invariant mass, is not very useful for the purpose of reconstructing the mass of the mother particle: one might have to resort to including information about the invisible particle(s) in the same decay chain. Since we can only measure the *total* missing transverse momentum in the event which is *shared* between invisible particles from two mothers, we must use measurements from both sides. An option is to use "M_{T2}"-type observables/variables [4–27]. Another case where one of the analyses using the invariant mass distribution (based on single mother decay) might not work is when the visible/SM particles in the decay chains with one and two DM (of course for Z_3 model) are not identical (even if they is more than one). Thus, one does not obtain a double edge for the case of intermediate particles in the decay chains being *off*-shell.

With the above motivations in mind, in the relevant part,

- we develop techniques for distinguishing Z_3 models from Z_2 models using information from *both* mother decays and the *missing* (in addition to visible) energy/momentum in an event.

We especially study the above cases where the techniques with the invariant mass variable might not work – in this sense, our work with the stransverse mass/M_{T2} variable is *complementary* to that with the invariant mass variable.

- We show that shapes and edges of these M_{T2} distributions, along with the ratio of visible momentum/energy on the two sides of the event, act as powerful discriminants between Z_3 and Z_2 models (including the case of a neutrino, i.e., mass*less* invisible particle – in addition to DM, in the final state for Z_2

models).

1.4.2.3 Energy peak

The method using the energy peak, which is developed in this thesis, is primarily predicated upon the features of the energy distribution of the visible particle coming from purely two- and three-body decays. We remark that this is the first work to use the energy distribution of the the decay products to study the stabilization symmetry of the DM. In fact, other work has typically focused on using Lorentz invariant quantities or quantities that are invariant under boosts along the beam direction of the collider. This is the case for the invariant mass or the stransverse/M_{T2} distributions. In particular, the technique using the invariant mass variable used the endpoints of kinematic distributions to probe the stabilization symmetry of the DM whereas this method relies quite directly on peak measurements and only marginally on endpoint measurements. Additionally, we note that the methods using the invariant mass variable apply only to the case where there is more than one visible particle per decay. Therefore, this result for cases where there is only one visible particle per decay is complementary to the results from the invariant mass distribution.

Our basic strategy is explained in the following. It relies on a new result:

- Assuming massless visible decay products and the unpolarized production of the mother particles, we shall show that in a *three*-body decay the peak of the observed energy of a massless decay product is *smaller* than its *maximum* energy in the *rest* frame of the mother.

This observation can be used in conjunction with a previously observed kinematic characteristic of the two-body decay to distinguish the stabilization symmetry of the DM. Specifically, it was shown in references [54, 55] that

- For an unpolarized mother particle, the peak of the laboratory frame energy distribution of a massless daughter from a *two*-body decay *coincides* with its (fixed) energy in the *rest*-frame of the mother.

Clearly, to make use of these observations in distinguishing two from three-body decays, we need to measure the "reference" values of the energy that are involved in these comparisons. Moreover, the procedure that is to be used to obtain this reference value from the experimental data should be applicable to both two and three-body decays. To this end, we find that when the mother particles are pair-produced, as happens in hadronic collisions, the M_{T2} variable can be used. Thus, these observations make counting the number of invisible decay products possible by looking only at the properties of the single detectable particle produced in the decay. However, it is worth noting that our proof of the above assertion regarding the kinematics of two- and three-body decays is only valid with a massless visible daughter and an unpolarized mother. Therefore, care must be taken when discussing cases with a massive daughter or a polarized mother.

1.5 Outline of thesis

In Chapter 2, we discuss how to determine the DM properties using the invariant mass variable. We begin with the case of off-shell intermediate particles in a

decay chain followed by the case of on-shell intermediate particles. We there explicate the general strategies of distinguishing Z_2 from Z_3 models, i.e., "double-edge" and "cusp" signatures, respectively. For the latter, we show that the feature of the cusp is intact even in the presence of any generic spin correlations by a formal proof as well as some Monte Carlo simulation. Some possible extensions and challenging issues regarding the techniques proposed therein are also briefly discussed.

In the following section, we consider the generic decay of a heavy resonance without any prior assumptions about the decay topology or the number of invisible particles. Assuming that there are two visible particle in the final state, we show that there are two decay topologies with one invisible particle and seven decay topologies with two invisible particles. We then demonstrate how to analyze and contrast the invariant mass distribution in each of those nine cases. In particular, we provide the formulae for the shape, kinematic endpoint, the location of the peak, and the curvature of the peak. We also present the topology disambiguation diagram as a way of distinguishing the event topologies.

In Chapter 3, we begin with a review of the M_{T2} variable in Z_2 models. We present some important formulae such as the location of the maximum value of the M_{T2} distribution, and discuss some interesting features such as a "kink" in the maximum M_{T2} as a function of the "trial" DM mass in the case where more than one visible particle is involved in each decay chain. Once this review is done, we move on to the M_{T2} variable in Z_3 models. We define three different event types arising in Z_3 models based on the number of dark matter particles in the final state and provide their corresponding theoretical predictions of the maximum M_{T2}. In

particular, we discuss the conditions to have a kink in maximum M_{T2} as a function of trial DM mass for the cases where there exist more than two DM particles in the final state: such situations do not arise in Z_2 models. We further show some simulation results for M_{T2} distributions for the new types of events in Z_3 models and discuss some notable features to be used for distinguishing Z_3 models from Z_2 models.

In the following two sections, we provide detailed applications of our results of the previous two sections for distinguishing Z_3 from Z_3 models. First we consider the easier case where the decay chain with one DM contains visible/SM particle(s) which are *not* identical to the ones in the two DM decay chain mentioned above (in Z_3 models). Based on the theoretical considerations given in the first two sections, we provide ways of distinguishing Z_3 models from Z_2 models, as well as measuring the mother and DM masses. We do it for both the case of one visible/SM particle in the two decay chains and more than one visible/SM particle case. In the next section we deal with the case where one DM and two DM decay chains contain identical visible/SM particle(s), and discuss *additional* techniques required in this case to distinguish Z_2 and Z_3 models. In all of the examples above, we make the simplifying assumption that the intermediate particles in the decay chain are off-shell.

In Chapter 4, we first review the current theory about the peak position in the energy distribution of a visible particle coming from a two-body decay, and then move onto the derivation of new results about the energy spectrum of the decay products of two- and three-body decays. Once the discussion on the energy

spectrum is done, we quote some key results from Chapter 3. By comparing them with the peak position in the energy spectrum of visible particle(s), we invoke some noteworthy physical implications. They are then the foundation of the general technique presented in the following section for differentiating decays into one DM particle from those into two DM particles.

In the next section, we apply this technique to the specific case of bottom partners at the LHC. There we remark that the b quark is relatively light compared to the expected mass of the bottom partner, so that our theoretical observation for massless visible particles is expected to apply. Additionally, the production of bottom partners proceeds dominantly via QCD and is thus unpolarized. In this sense, the example of a bottom partner is well-suited to illustrate our technique. To be more realistic, we include the backgrounds to the production of bottom partners, and show that they are under control so that our technique works even in the presence of background.

Chapter 5 provides the conclusion to the thesis.

Chapter 2: Invariant mass

2.1 Overview

In this chapter, we discuss how to determine the physical properties of invisible particles using the invariant mass variable. We mostly study the decay of a *single* heavy particle, which is charged under the dark matter stabilization and SM symmetries, into dark matter candidate(s) and the relevant SM state *inside* the detector. In order to form the invariant mass variable, such a SM/visible state will be used in each event. In addition, such heavy particles are denoted by "mother" particles here and throughout this thesis. As discussed in Chapter 1, such mother particles must be produced in pairs due to the unbroken dark matter stabilization symmetry so that in each event there exist two decay chains. As mentioned before, we here consider each decay chain separately, i.e., the information coming from the other decay side is irrelevant, which will be dealt with in Chapter 3. In this context, it is assumed that we are aware which visible particle is emitted from which particle. Hence, it is understood that the visible products constructing the associated invariant mass variable belong to the same decay chain.

We first begin with *off*-shell intermediate particles. More specifically, we consider the possibility that a mother particle decays into two visible particles and *one*

or *two* DM particles via three- and four-body decay process, respectively. We point out that in Z_2 models the second scenario, i.e., the decay into two DM's, is absent while in Z_3 models both of them are possible. Therefore, if the visible states involving one or two DM particles are identical, for the Z_3 case it is anticipated to have a double edge signature in the relevant invariant mass distribution. In addition, the gap between the two edges can be a direct measurement of the DM mass.

On the other hand, in the case with intermediate particle(s) being *on*-shell the method of searching for a double-edge signal is *not* successful since even Z_2 models can easily fake such a signal by introducing intermediate particle(s) with different masses. Instead, we focus on a particular decay topology in which one of the two DM particles is located in-between the two visible particles. Obviously, this decay topology is absent in Z_2 models. It turns out that such a decay chain develops a "cusp", i.e., derivative discontinuity, in the middle of the relevant invariant mass distribution. We further verify that such a cuspy structure is actually invariant even in the presence of the effect of spin correlations.

Once consideration of those two cases is done, we further generalize the idea of extracting various information from the invariant mass distribution to more generic decay process of a heavy resonance. For simplicity we study the cases that there are two visible particles and one or two invisible particles in the final state. Here the invisible particles (in the final state) do not have to have the same mass. We provide analytic formulae for the overall shape, the kinematic (upper) endpoint, the location of the peak and the curvature around the peak in the invariant mass distribution of the two visible particles for each of the distinct decay topologies. We

demonstrate that the decay topologies, which are typically hypothesized in most of the relevant studies, can be distinguished using the endpoint, peak position and curvature. In each case, we provide the effective mass variables which can be extracted in experiment, and show for some cases the shape analysis is adequate to pin down the masses of the new particles, including the overall mass scale.

2.2 Off-shell intermediate particles

In this section we assume that all intermediate particles (if any) in this decay chain are *off*-shell, i.e., (here and henceforth) they are heavier than their mother particle.[1] This off-shell scenario has been frequently studied by the ATLAS and CMS collaborations [48, 49] for SUSY theories (which is an example of a Z_2 model).

We consider constructing the invariant mass distribution of the (visible) decay products. Unlike for the Z_2 case, for Z_3 models a mother particle A can decay into one or two DM particles along with (in general different) SM particles. We mostly assume, just for simplicity, that there exist two visible particles (a, b or c, d) in the final state as shown below (note however that the same argument is relevant to the general cases where more than two visible particles are emitted):
Here (and henceforth) the "blob" denotes intermediate particles in the decay which are off-shell. Also, upper-case letters/red/dashed lines denote particles charged under the DM symmetry (Z_3 or Z_2) and lower-case letters/black/solid lines denote

[1] In general, the off-shell state implies that the square of the relevant four momentum is not the same as its invariant mass, i.e., $p^2 \neq m^2$. However, we restrict ourselves to the case described here throughout this thesis.

(2.1)

SM (or "visible", as opposed to DM) particles, including, for example, a W boson. Such an unstable SM particle decays further into SM fermions, at least some of which are observed by the particle detector.

For simplicity, we assume that the SM (or visible) parts of the event can be completely reconstructed. Considering the invariant masses m_{ab} and m_{cd}, which are formed by the two SM particles a, b and c, d in each decay chain, one can easily derive the minimum and the maximum kinematic endpoints of the distributions of m_{ab} and m_{cd} which are given by [56]:

$$m_{ab}^{\min} = m_a + m_b, \tag{2.2}$$

$$m_{ab}^{\max} = M_{\text{mother}} - m_{\text{DM}} \qquad \Big(\text{Left process of Eq. (2.6)}\Big), \tag{2.3}$$

$$m_{cd}^{\min} = m_c + m_d, \tag{2.4}$$

$$m_{cd}^{\max} = M_{\text{mother}} - 2\,m_{\text{DM}} \qquad \Big(\text{Right process of Eq. (2.6)}\Big). \tag{2.5}$$

Physically, the lower limit corresponds to the case when the two visible particles a, b (and similarly c, d) are at rest in their center-of-mass frame so that they move with the same velocity in any Lorentz frame. The upper limit corresponds to the case in which the DM particle(s) are at rest in the overall center-of-mass frame of the final state. Both maxima are independent of the masses of the virtual intermediate particles. The point is that the upper endpoints in the two distributions are different.

2.2.1 Double edge

An especially striking/interesting case is when the SM particles in the two decay chains are identical:

(2.6)

As we show below, it is possible to obtain a *double* edge in the distribution of this SM final state. We begin with presenting a basic idea of this phenomenon, before going on to more details.

2.2.1.1 Basic idea

Taking into account the fact that the visible particles of both decays are the same and assuming that both subprocesses are allowed, the experimental distribution $(1/\Gamma)\ d\Gamma/dm_{ab}$ will contain events of both processes. In such a combined distribution, clearly, the endpoint of Eq. (2.5) – denoted now by $m'^{\max}_{ab}$ – will become an *edge* in the middle of the distribution, which along with the overall kinematic endpoint given by Eq. (2.3), will give rise to a *double edge* signal. Assuming the two edges are visible, it is interesting that we can determine *both* the DM and mother particle masses by simply inverting Eqs. (2.3) and (2.5):

$$m_{\rm DM} = m^{\max}_{ab} - m'^{\max}_{ab}, \tag{2.7}$$

$$M_{\rm mother} = 2m^{\max}_{ab} - m'^{\max}_{ab}. \tag{2.8}$$

In particular, the distance between the two edges is identified as the DM mass.

In contrast to the cases just considered, in Z_2 scenarios only one or three DM particles (i.e., not two) are allowed in a single decay chain due to Z_2-charge conservation (unless the process is triggered with an uncharged mother particle [37]). Independently of phase-space considerations, we note that in Z_2 models the decay chain with three DM particles should be highly suppressed with respect to the one DM case. The reason for such an expectation is that a decay with three DM in the final state requires a vertex with *four* (in general different) Z_2-charged particles which is typically absent, at least at the renormalizable level in most models.[2] Therefore with only one possible decay process (in terms of the number of DM particles in the final state) we can only observe a single kinematic endpoint in the invariant mass distributions in a Z_2 model.

2.2.1.2 Details

Of course the visibility of such a signal depends on the shapes of the distributions of each subprocess as well as their relative decay branching fractions. The solid curve and the dashed plot in the left panel of Figure 2.1 illustrate the generic shape of the distributions for the two processes of Eq. (2.6) based only on pure kinematics, i.e., no effects of matrix element and spin-correlations. (Such effects might be important and we will return to this issue in the context of specific models

[2]Compare this situation to the Z_3 case, where appearance of two DM in a decay chain comes from a vertex with *three* Z_3-charged particles which is more likely to be present, especially at the renormalizable level.

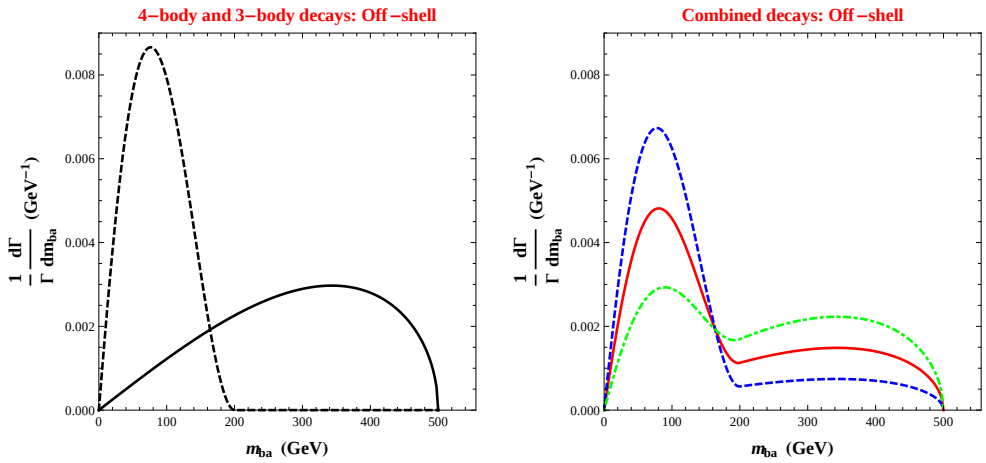

Figure 2.1: Invariant mass distribution $(1/\Gamma)\, d\Gamma/dm_{ab}$ for the processes of Eq. (2.6). The masses of the mother particle A and of the DM particles are $m_A = 800$ GeV and $m_{\rm DM} = 300$ GeV and the SM particles a and b are assumed to be massless. The solid and dashed curves on the left panel represent the distributions for the 3-body decay and the 4-body decay, respectively. On the right panel, blue/dashed (highest peaked), red/solid, and green/dot-dashed (lowest peaked) curves show the combined distributions with branching ratios of 3-body to 4-body given by 1:3, 1:1, and 3:1, respectively.

to show that multiple edges can still "survive" after taking these effects into consideration.) Because of the phase-space structure of the processes one realizes that the distribution in the case of 3-body decays is more "bent" towards the right (i.e., larger values of invariant mass) whereas for the 4-body decays the peak of the distribution leans more towards the left (i.e., smaller values of invariant mass). Because of this feature, the combination of the two distributions can give rise to two visible *edges* (as long as the relative branchings of the two decays are of comparable size). This is shown in the right panel of Figure 2.1 in which we show the combined invariant mass distribution of the two visible SM particles, for three different relative branching fractions of the two subprocesses. Based on the location of the *edges* in

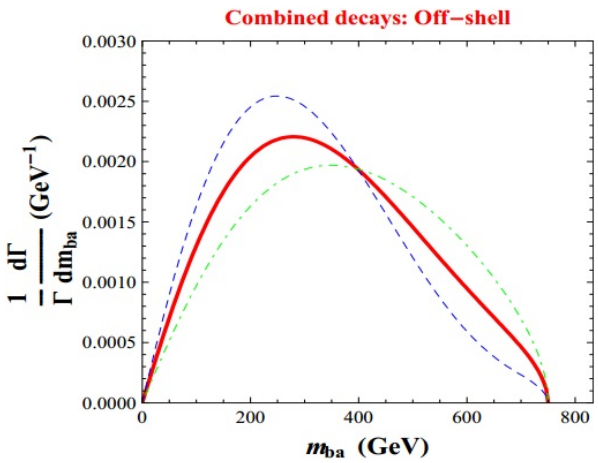

Figure 2.2: Same as the right panel of Figure 2.1 but using a smaller DM mass, $m_{\rm DM} = 50$ GeV. The *edge* in the middle of the distribution is no longer apparent.

right panel of Figure 2.1 and Eqs. (2.7) and (2.8), the mass of the DM particle must be about 300 GeV and the mass of the mother particle must be about 800 GeV, which are of course the masses used in the example.

Whether or not the double-edge signal is clear (and hence we can determine the DM and mother masses) also depends on the DM mass which must be relatively sizable compared to the mass of the mother particle. For example, if we take a DM mass of 50 GeV instead of 300 GeV that we assumed above, with the mother mass fixed at 800 GeV, we observe from Figure 2.2 that the plotted distribution does not provide a good measurement of $M_{\rm mother}$ and $m_{\rm DM}$.

Let us return to the issue of the relative branching fraction for each subprocess. The decay into two DM particles should be generically phase-space suppressed relative to the decay into just one DM particle, So, based on pure phase-space suppression, the branching ratio of the decay into two DM might be much smaller

than the decay into one DM (unlike what is chosen in the figures above). Hence, it might be difficult to observe a double-edge signal. However, in specific models this suppression could be compensated by larger effective couplings so that the two decays have comparable branching ratio, and therefore, the double-edge is visible as in Figure 2.1.

In fact, another possibility is that the two decay chains for the Z_3 case, i.e., with one and two DM particles, do *not* have *identical* SM final states, but there is some overlap between the two SM final states. For example, if we assume that particle

(2.9)

c is (at least approximately) massless, then the maximum kinematic endpoint of m_{ab} in the first of the above-given two reactions is still $M_{mother} - m_{DM} - m_c \approx M_{mother} - m_{DM}$. In this situation *both* the reactions have 4-body final states and hence could be easily have comparable rates, at least based on phase-space (*c.f.* Earlier we had 3-body vs 4-body by requiring the same two-body SM final state for the two reactions found in (2.6)). On the other hand, although the two rates are now comparable, it might actually be harder to observe a double edge because the shape of the two individual distributions are both peaked towards the left (i.e., smaller values of invariant mass) and even if they have different end-points, the combined distribution might not show as clearly a double edge as the earlier case where the

two shapes are apparently distinct.

2.2.2 Different edges in pair production

Finally, what if there are no common SM particles between the final states of the decay chains with one and two DM particles so that we do not obtain a double edge? In this case, one can consider another analysis, by making the further assumption that the same mother particle A is pair-produced in each event, and that the decay products of each A are now distinct and very light or massless, *i.e.*, here we have chosen three SM particles (a, b, c) in the decay chain with one DM

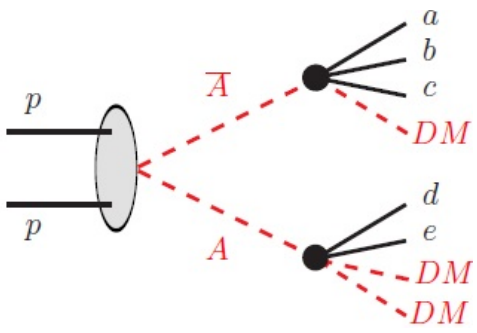

(2.10)

just so that both decay chains involve a 4-body final state. In this situation one can restrict to events with all five SM particles (a,...e) particles in the final state[3], but use both sides of the event, i.e., obtain the full invariant mass distribution of the visible particles of each (distinct) side. In the interpretation of these results in the context of a Z_3 model, the difference between the endpoints of each separate distribution will give the dark matter mass, and like before, the mass of the mother particle A

[3]If we include other events which have a, b, c or d, e on *both* sides, we still get the different edges that we discuss below, but as we will mention later, such events will not allow us to get rid of "faking" Z_2 models.

can be found using a combination of the two end-points, i.e., $m_{\rm DM} = m_{abc}^{\rm max} - m_{de}^{\rm max}$ and $M_{\rm mother} = 2m_{abc}^{\rm max} - m_{de}^{\rm max}$.

2.3 On-shell intermediate particles

In this section, we consider the case where the mother particle decays into SM and DM via intermediate particles which are all *on*-shell. Again, like in section 2.2 all particles are assumed to decay inside the detector. In this case, the endpoints of invariant mass distributions will depend on the masses of these intermediate states as well as the masses of the mother and the final state particles. Both in the Z_2 and Z_3 cases there will be more possibilities for the upper endpoints because of the possibilities of "Multiple topologies" and "Different Intermediate Particles" (to be explained below) for the same visible final state. Since even for the Z_2 case it is possible to obtain multiple edges, finding multiple edges is not any more a robust discriminator between Z_2 and Z_3 unlike the off-shell decay case. We then discuss a topology of the decay chain which does allow us to distinguish between the two models.

2.3.1 Additional sources of multiple edges

Here we discuss how it is possible to obtain multiple edges even if we do *not* combine decays of the mother particle into one and two DM particles.

2.3.1.1 Multiple topologies

For Z_3 models we can expect multiple endpoints from the decays of the same mother particle into a given SM final state by combining the two decay chains with one DM and two DM particles, respectively, just as in the case of the decays with off-shell intermediate particles. However, this is not the only way of obtaining multiple endpoints, i.e., such a combination of decay chains with one and two DM is not essential. The reason is that there are multiple possible topologies even with the completely identical final state if it contains *two* DM, due to the various possibilities for the locations of two DM particles relative to the other SM particles in a decay chain. For example, for the case of a 4-body decay process (i.e., two SM and two DM particles) there will be *three* different possibilities:

(2.11)

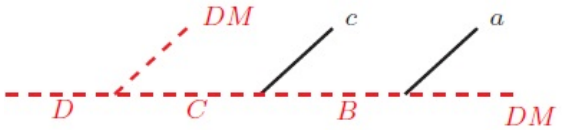

(2.12)

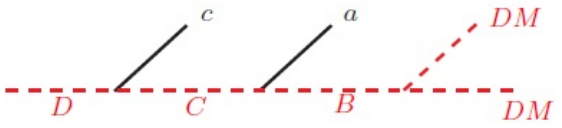

(2.13)

Note that (as above) decay cascades involve a "charged-charged-charged" (under Z_3 symmetry) vertex (in addition to "charged-charged-neutral" vertices) in order to contain two DM particles in the final state.

Assuming that the visible particles are massless, $m_a = m_c = 0$, the upper

endpoints for each topology are given by (see Chapter A for details.):

$$(m_{ca}^{\max})^2 = \frac{2(m_D^2 - m_C^2)(m_B^2 - m_{DM}^2)}{m_B^2 + m_C^2 - m_{DM}^2 - \lambda^{1/2}(m_C^2, m_B^2, m_{DM}^2)} \quad \Big(\text{for Eq. (2.11)}\Big) \quad (2.14)$$

$$(m_{ca}^{\max})^2 = \frac{(m_C^2 - m_B^2)(m_B^2 - m_{DM}^2)}{m_B^2} \quad \Big(\text{for Eq. (2.12)}\Big) \quad (2.15)$$

$$(m_{ca}^{\max})^2 = \frac{(m_D^2 - m_C^2)(m_C^2 - m_B^2)}{m_C^2} \quad \Big(\text{for Eq. (2.13)}\Big) \quad (2.16)$$

where λ is the well-known kinematic triangular function given in the form of

$$\lambda(x, y, z) = x^2 + y^2 + z^2 - 2xy - 2yz - 2zx. \quad (2.17)$$

The main point is that kinematic endpoints are functions of the masses of the mother, the DM and the intermediate particles, and moreover, this dependence changes according to different topologies. Thus, even if the intermediate particles involved in these decays of a given mother particle are the same, one will still obtain multiple endpoints.[4] Finally, if we combine decay chains with one and two DM in the final state (even if the latter has just one topology), the difference between the two endpoints will not lead to a direct measurement of the DM mass like in the off-shell decay case because again, the mass of intermediate particles is one of the main ingredients to determine the endpoints.

In Z_2 models the decay topologies must have a single DM particle and that too at the end of the decay chain because the vertices in the decay cascade are of the form "odd-odd-even" (under the Z_2 symmetry).[5] Nevertheless, there can still be different topologies because of different ordering of the visible states. For example: Obviously, the endpoints for a given invariant mass distribution, say m_{ca}, will be different for each of these two topologies, and actually they can be obtained from

[4]Of course, the different possible decay topologies can, in general, have different intermediate

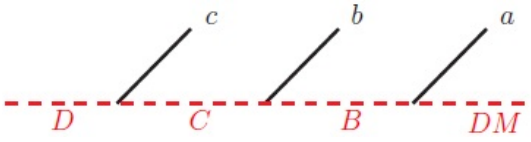

(2.18)

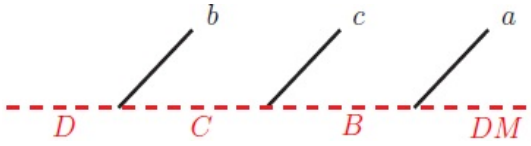

(2.19)

.
.
.

Eqs. (2.14) and (2.15) by just replacing m_{DM} in the denominator of Eqs. (2.14) by m_b and leaving Eqs. (2.15) unchanged (and where m_a and m_c are still assumed to vanish).

2.3.1.2 Different intermediate particles for same final state

In addition, even if the topology and the order of visible particles are the same, there is the possibility of multiple paths for the *same* mother particle to decay into the same (SM and DM) final state by involving different intermediate particles. We will obtain multiple endpoints in this case because of the dependence of the endpoints on the masses of intermediate particles (as mentioned above). This argument is valid for both the Z_2 and Z_3 models (and one or two DM for the latter case): for a final state with two SM and one DM, we can have the situation shown in Figure (2.20). For example, in SUSY, the decay chain $\chi_2^0 \to l^+ l^- \chi_1^0$ can proceed via intermediate right- or left-handed slepton. Since the masses of intermediate right-

states.

[5]Note that a similar argument applies to decay chains in Z_3 models with only *one* DM in the final state.

(2.20)

and left-handed sleptons are in general different, multiple endpoints are expected.

2.3.2 Cusp topology

So far, we have learned that for on-shell intermediate particle cases the multiple edge signal is not a good criterion to distinguish Z_3 from Z_2. Instead, we focus on the *shapes* of these distributions. Consider the topology which can be present in Z_3 models (but absent in the Z_2 case) with two visible SM particles separated by a DM particle[6], i.e.,

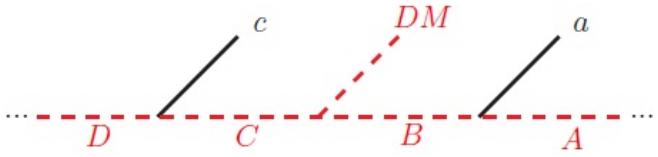

(2.21)

We assume massless SM particles (i.e., $m_a = m_c = 0$) and the mass hierarchy $m_D > m_C > m_B > m_A$. Also, we neglect spin-correlation effects in this section. We sketch the derivation of the distribution of the ac invariant mass here and refer the reader to the Chapter A for details. The differential distribution $\frac{1}{\Gamma}\frac{\partial\Gamma}{\partial m_{ac}^2}$ that we want to study can be obtained for this "new" topology easily by noting that

[6]Note that in general D might come from the decay of another Z_3-charged particle and similarly, at the end of the decay, A might not be the DM, that is, it could itself decay further into DM particles and other visible states as long as Z_3-charge conservation is respected. The "..." to the left of D and to the right of A signify this possibility.

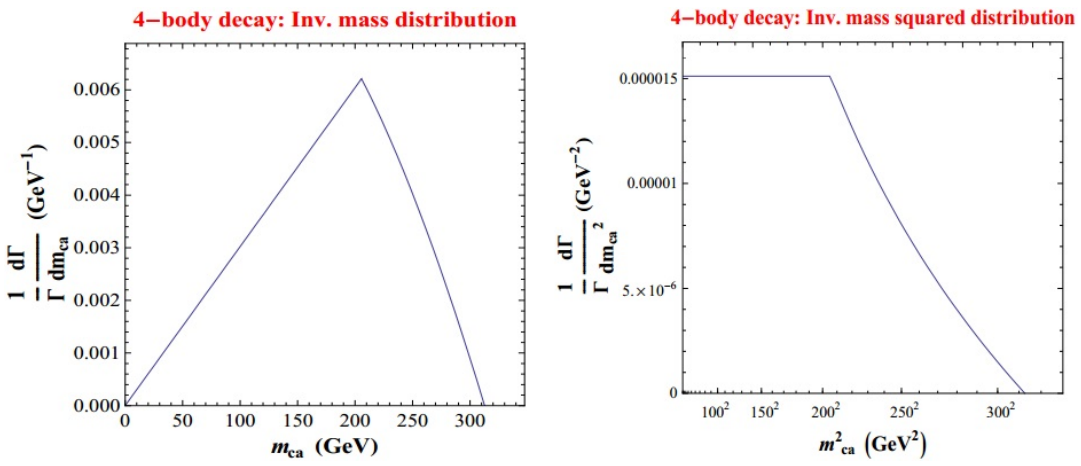

Figure 2.3: The panel on the left shows the distribution in m_{ca} while the right hand panel shows the distribution in m_{ca}^2 from the decay chain of Eq. (2.21). The masses of the mother particle, two intermediate particles, and DM particles are 800 GeV, 700 GeV, 400 GeV, and 200 GeV, respectively and the SM particles are assumed massless. A "cusp" due to the topology of Eq. (2.21) is clear in both distributions.

the differential distribution $\frac{1}{\Gamma}\frac{\partial^2\Gamma}{\partial u \partial v}$ must be flat, where the variables are defined as follows

$$u = \frac{1-\cos\theta_{c\,\mathrm{DM}}^{(C)}}{2} \qquad \text{and} \qquad v = \frac{1-\cos\theta_{ca}^{(B)}}{2}, \tag{2.22}$$

with $\theta_{ca}^{(B)}$ being the angle between c and a in the rest frame of B, and $\theta_{c\,\mathrm{DM}}^{(C)}$ being the angle between c and DM in the rest frame of C [57]. In addition, we have $0 < u, v < 1$. Thus, we can write

$$\frac{1}{\Gamma}\frac{\partial^2\Gamma}{\partial u \partial v} = \theta(1-u)\theta(u)\theta(1-v)\theta(v) \tag{2.23}$$

One further finds that

$$m_{ca}^2 = m_{ca}^{\max}(1-\alpha u)v, \tag{2.24}$$

where m_{ca}^{max} is given in Eq. (2.14) with m_{DM} in the numerator replaced by m_A, and so we can make a change of variables from the differential distribution of Eq. (2.23) and obtain the distribution $\frac{1}{\Gamma}\frac{\partial^2\Gamma}{\partial u \partial m_{ca}^2}$, which can then be integrated over u to finally obtain the distribution with respect to m_{ca} [7]:

$$\frac{1}{\Gamma}\frac{\partial\Gamma}{\partial m_{ca}} = \begin{cases} \dfrac{2m_{ca}}{(m_{ca}^{\max})^2\ \alpha}\ \ln\dfrac{m_C^2}{m_B^2} & \text{for}\quad 0 < m_{ca} < \sqrt{1-\alpha}\ m_{ca}^{\max} \\ \\ \dfrac{2m_{ca}}{(m_{ca}^{\max})^2\ \alpha}\ \ln\dfrac{(m_{ca}^{\max})^2}{m_{ca}^2} & \text{for}\quad \sqrt{1-\alpha}\ m_{ca}^{\max} < m_{ca} < m_{ca}^{\max} \end{cases} \tag{2.25}$$

where $m_{ca}^{\max}$ is given in Eq. (2.14) and

$$\alpha = \frac{2\lambda^{1/2}(m_C^2, m_B^2, m_{\rm DM}^2)}{m_B^2 + m_C^2 - m_{\rm DM}^2 + \lambda^{1/2}(m_C^2, m_B^2, m_{\rm DM}^2)}. \tag{2.26}$$

From these results we can easily see that the new topology introduces two different regions in the m_{ca} distribution with a "cusp" at the boundary connecting both regions, located at $\sqrt{1-\alpha}\ m_{ca}^{\max}$. Figure 2.3 shows the same distribution in both panels, but with respect to m_{ca} on the left panel and with respect to m_{ca}^2 on the right panel. As we will argue later, the second option seems better suited once spin correlations are taken into account, but in both plots, one observes that the cuspy feature is quite clear.

2.3.2.1 Two visible particles

Consider first the simple case of *only* two visible particles in a decay chain. In the Z_3 reaction of Eq. (2.21), D is then the mother particle and A is DM. Clearly, we would find a cusp in the invariant mass distribution of the two visible particles in

[7] Note that $\frac{1}{\Gamma}\frac{\partial\Gamma}{\partial m} = 2m\ \frac{1}{\Gamma}\frac{\partial\Gamma}{\partial m^2}$.

the Z_3 model, but not for the Z_2 model since the two visible particles must always be adjacent to each other in the latter case.[8] Thus, the presence/absence of cusp could be used to distinguish Z_3 and from Z_2 models.

2.3.2.2 Generalization to more than two SM particles in decay chain

Of course, in general in both Z_2 and Z_3 models there will be more than two visible particles with possibly some of them being identical, and this will undoubtedly complicate the analysis. For example, in the reaction of Eq. (2.21), a, c, or both can be produced at some other place of the same decay chain in addition to the locations shown there, e.g.,

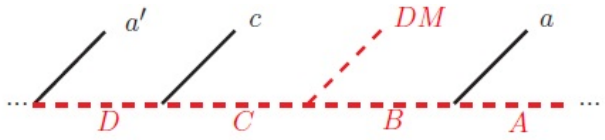

(2.27)

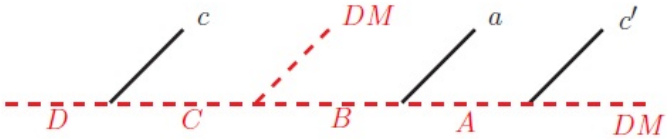

(2.28)

Here a', which is an identical particle to a, is assumed to come from the immediate left of D, and c', which is an identical particle to c, is assumed to come from the immediate right of A. Note that there is no DM between a' and c (unlike between a and c) in first reaction above (similarly between a and c' vs between a and c in second reaction above), and that a and a', and c and c' are identical. Therefore, in

[8] Note that we are considering decay of a Z_3 or Z_2-*charged* mother. A Z_2-uncharged, i.e., *even*, mother *is* allowed to decay into two DM and can give a cusp in the invariant mass of two visible particles from such a decay [37].

both these examples, it is clear that we will obtain a more complicated distribution in m_{ac} than the one studied previously.

Nevertheless, the method described previously to disentangle the Z_2 from the Z_3 cases (when having two visible particles), can still be generalized to the situation of many visible particles in a decay chain. For example, let us consider the case of *three* visible SM particles in the final state for both Z_3 and Z_2 models. We will obtain a cusp even in the Z_2 case when considering the invariant mass of two *not* "next-door neighbor" visible particles such as in m_{ac} for the decay process in Eq. (2.18). The reason is that, even though the precise topology of Eq. (2.21) is absent in a Z_2 model, a similar one is generated by the presence of a SM particle (i.e., b) in-between two other SM particles (i.e., a and c) as in Eq. (2.18). Thus the analysis performed earlier for Eq. (2.21) applies in this case, but with the DM mass set to zero (assuming SM particle b is massless).

However, this type of degeneracy between Z_2 and Z_3 can be resolved by considering all of the three possible *two-(visible) particle* invariant mass distributions. In the Z_3 case with two DM particles in the final state, two of these three invariant mass distributions will have cuspy features whereas only one such invariant mass distribution will have a cusp in the Z_2 case. The reason is again that in the Z_3 case, since one more particle is added to the decay products compared to the Z_2 case (i.e., we have two invisible and three visible particles), there will be final state particles (visible or not) in-between the two visible particles for two of the three pairings. This feature remains true for more visible particles, i.e., in general we will obtain more cusps in the invariant mass distributions in a Z_3 model than in a Z_2 model.

2.3.3 Spin correlations

Once spin correlations are involved, the derivative discontinuity (cusp) might appear unclear. Nevertheless, it may still be possible to distinguish a Z_3 model from a Z_2 model by employing the fitting method which we will show in the rest of this section. The basic idea is that the distribution $d\Gamma/dm_{ca}^2$ of three-body decays in Z_2 (i.e., one DM particle and two visible particles) can (almost) always be fitted into a quadratic function in m_{ca}^2, whereas the distribution of the new topology of Z_3 cannot be fitted into a single quadratic function, that is, two different functions are required for fitting each of the two sub-regions of the distribution. Let us see how this works for a Z_2 model (i.e., one DM and two visible particles) and a Z_3 model (i.e., two DM and two visible particles) in turn.

2.3.3.1 Z_2 case: 1 DM + 2 Visible

We can again make use of the same angular variables considered earlier for the case of this 3-body decay cascade, shown for example in Eq. (2.20). According to the references [57] and [58], the normalized distribution including spin-correlations is given by

$$\frac{1}{\Gamma}\frac{\partial\Gamma}{\partial t} = \theta(t)\theta(1-t)f(t) \tag{2.29}$$

where again we have defined the variable t as

$$t \equiv \frac{1-\cos\theta_{ba}^{(B)}}{2}. \tag{2.30}$$

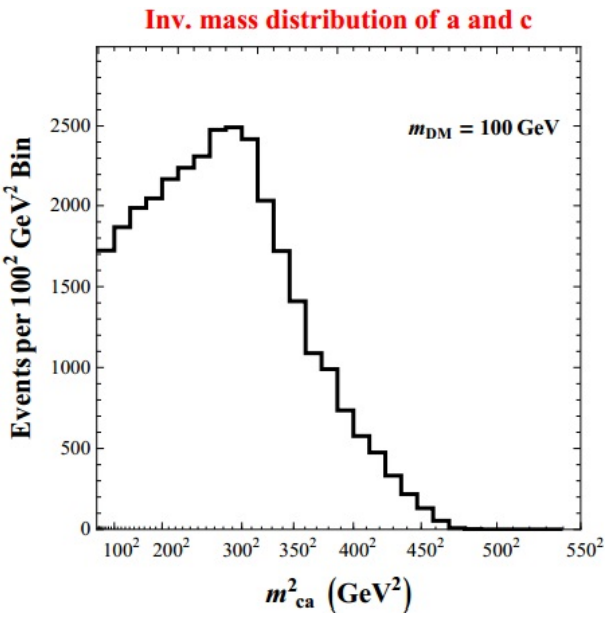

Figure 2.4: Invariant mass distribution of particles a and c, from the decay chain shown in Eq. (2.21), including spin correlations, and such that the intermediate particle C has spin 1 and the intermediate particle B has spin 1/2, and the couplings are chiral. The "cusp" in this distribution appears more defined than in Figure 2.3 where spin correlations were not considered.

Here $f(t)$ is a function of t and $\theta_{ba}^{(B)}$ is the angle between particles a and b of Eq. (2.20) in the rest frame of particle B. One then notes that $m_{ba}^2 = (m_{ba}^{\max})^2\ t$ which basically means that the distribution with respect to the invariant mass m_{ba}^2 (which is of our interest) is essentially the same as the one with respect to t above. This means that the distribution in m_{ba}^2 will have the functional form f. According to the reference [59], such spin correlation functions are just polynomials of $\cos\theta_{ba}$ (i.e., $(1-2t)$). Moreover, if we restrict our consideration to particles of spin-1 at most, the maximum order in t of the polynomial is two, which means that the most

general form of f will be

$$f(t) = c_1 + c_2 t + c_3 t^2. \tag{2.31}$$

In turn, the invariant mass distribution we are interested in must therefore take the form (in the region between the endpoints enforced by the θ-functions)

$$\frac{1}{\Gamma}\frac{d\Gamma}{dm_{ba}^2} = c_1' + c_2' m_{ba}^2 + c_3' m_{ba}^4. \tag{2.32}$$

With the experimental data we can construct the invariant mass distribution, and we will be able to determine the three constants c_1', c_2', and c_3' by fitting into a parabola in the m_{ba}^2 variable. In other words, for any 3-body decay chain, with or without spin-correlation, it is always possible to fit the invariant mass distribution $\frac{1}{\Gamma}\frac{d\Gamma}{dm_{ba}^2}$ into a curve quadratic in m_{ba}^2.

2.3.3.2 Z_3 case: 2 DM + 2 visible

We now consider the new topology of Eq. (2.21) including the possibility of spin correlations. As in Section 3.1, we use the same angular variables u and v. However, the normalized distribution with spin correlations become a little more complicated than before

$$\frac{1}{\Gamma}\frac{\partial^2\Gamma}{\partial u \partial v} = \theta(v)\theta(1-u)g(u)\theta(v)\theta(1-v)h(v) \tag{2.33}$$

where again

$$u \equiv \frac{1-\cos\theta_{c\,\mathrm{DM}}^{(C)}}{2},\ v \equiv \frac{1-\cos\theta_{ca}^{(B)}}{2}. \tag{2.34}$$

Like in the previous section, $g(u)$ and $h(v)$ are spin-correlation functions (cf. $g = h = 1$ without spin correlation discussed earlier) and again the invariant mass squared is given by

$$m_{ca}^2 = (m_{ca}^{\max})^2(1 - \alpha u)\ v. \tag{2.35}$$

where α is the same kinematical constant defined in Eq. (2.26). As in the analysis without spin correlations, the two types of θ-functions will split the entire region into two sub-regions, with a cusp at the separation point, whose location is independent of the spin correlation effects (since it depends on purely kinematical constants α and m_{ca}^{max}). But unlike the scalar case (i.e., with no spin correlations), we have now two functions $g(u)$ and $h(v)$ which can change the shape of the distribution and in principle affect the derivative discontinuity (the cusp).

In detail, by the chain rule the previous normalized distribution can be modified and partially integrated to obtain

$$\frac{1}{\Gamma}\frac{d\Gamma}{dm_{ca}^2} = \int_0^{u_{\max}} \frac{du}{(m_{ca}^{\max})^2(1-\alpha u)}\ g(u)\ h\left(\frac{m_{ca}^2}{(m_{ca}^{\max})^2(1-\alpha u)}\right) \tag{2.36}$$

where

$$u_{\max} = \text{Max}\left[1, \frac{1}{\alpha}\left(1 - \frac{m_{ca}^2}{(m_{ca}^{\max})^2}\right)\right]. \tag{2.37}$$

The two possible choices in the definition of $u_{\max}$ above arise when integrating $\frac{1}{\Gamma}\frac{\partial^2\Gamma}{\partial m_{ca}^2 \partial u}$ with respect to u due, in turn, to the integration limits enforced by the θ functions. This leads to two different regions for the differential distribution such that in the first sub-region, we have $0 < m_{ca} < \sqrt{1-\alpha}\ m_{ca}^{\max}$ and $u_{\max} = 1$, while for the second region, we have $\sqrt{1-\alpha}\ m_{ca}^{\max} < m_{ca} < m_{ca}^{\max}$ and $u_{\max} = \frac{1}{\alpha}\left(1 - \frac{m_{ca}^2}{(m_{ca}^{\max})^2}\right)$

[57]. So far, most of the steps are similar to the case of no spin correlations except for the presence of the factors of spin correlation functions, g and h.

It would seem that we need to know the *precise* form of g and h in order to proceed further, i.e., in order to perform the integration in Eq. (2.36). However, for the purpose of determining whether or not there is a cusp, we will show that it is sufficient to know the fact that those spin-correlation functions must be second order polynomials in their argument as mentioned in the analysis of the Z_2 case. Using this fact we can write down the above integrand as

$$\begin{aligned}\frac{1}{1-\alpha u}g(u)h\left(\frac{t}{1-\alpha u}\right) &= \frac{b_1}{(1-\alpha u)^3}t^2+\frac{1}{(1-\alpha u)^2}(b_2t+b_3t^2)\\ &\quad+\frac{1}{1-\alpha u}(b_4+b_5t+b_6t^2)+(b_7+b_8t)+b_9(1-\alpha u)\end{aligned} \tag{2.38}$$

where we have introduced the same variable $t \equiv m_{ca}^2/(m_{ca}^{\max})^2$ used for the 3-body decays and where the kinematical constants b_i will depend on the specific nature of the couplings and particles in the decay chain (*i.e.*, they must be calculated on a case by case basis). The terms of the integrand are organized as a power series in $(1-\alpha u)$ – instead of in u – because of the simplicity of the former form. Integrating then gives

$$\frac{1}{\Gamma}\frac{d\Gamma}{dt} = \begin{cases} b_1'+b_2't+b_3't^2 & \text{for} \quad 0<t<\sqrt{1-\alpha} \\ \\ b_1''+b_2''t+b_3''t^2+(b_4''+b_5''t+b_6''t^2)\,\log t & \text{for} \quad \sqrt{1-\alpha}<t<1 \end{cases} \tag{2.39}$$

where again, the kinematical constants b_i' and b_i'' are specific to each situation. Thus, even with spin correlations, the functional dependence on t ($\propto m_{ca}^2$) is quite simple; however, the crucial point is that it is different for each sub-region of the

distribution. In particular this simple dependence in the distribution of m_{ca}^2 (and *not* m_{ca}) suggests that it may be more appropriate to consider the distribution of m_{ca}^2 instead of the distribution of m_{ca}. In Figure 2.4 we show the m_{ca}^2 invariant mass distribution for the decay chain of Eq. (2.21), but in the special case where particle C has spin 1 and the intermediate particle B is a fermion, and some of the couplings are chiral. We used `MadGraph/MadEvent` [60] to generate events taking the particles a and c to be massless and taking $m_{DM} = 100$ GeV. One can compare the shape of this distribution with the one from the right panel of Figure 2.3 and see that in this case, including the spin correlation makes the cusp even more apparent.

One of the main differences between the two subregions is that the first one has no logarithmic dependence in t while the second (in general) does have it. Of course, from Eq. (2.38), we see that this logarithmic term could be suppressed for the case $b_4 = b_5 = b_6 \sim 0$. However, even in this special case we would still have to employ different sets of coefficients in the two sub-regions as follows. The functional forms in both the regions are now quadratic in t, i.e.,

$$\frac{1}{\Gamma}\frac{d\Gamma}{dt} = \begin{cases} b_7 + \frac{b_9}{2}(2-\alpha) + \left(\frac{b_2}{1-\alpha} + b_8\right)\, t + \left[\frac{b_1(2-\alpha)}{2(1-\alpha)^2} + \frac{b_3}{1-\alpha}\right]\, t^2 & \left(0 < t < \sqrt{1-\alpha}\right) \\ \\ \frac{1}{\alpha}\left[b_2 + b_7 + \frac{b_1+b_9}{2} - (b_2 - b_3 + b_7 - b_8)\, t - (b_3 + b_8 + \frac{b_1+b_9}{2})\, t^2\right] & \left(\sqrt{1-\alpha} < t < 1\right) \end{cases} \tag{2.40}$$

Considering just the constant terms, we see that it is possible to obtain identical functions in the two regions only if $\alpha = 1$ and $b_1 = b_2 = 0$. However, using Eq. (2.17) and Eq. (2.26), it can be shown that α is always (strictly) less than 1. In other words, it is impossible that the distribution in each sub-region can be fitted successfully to the same polynomial of order two in t; the cusp will thus survive even in this case.

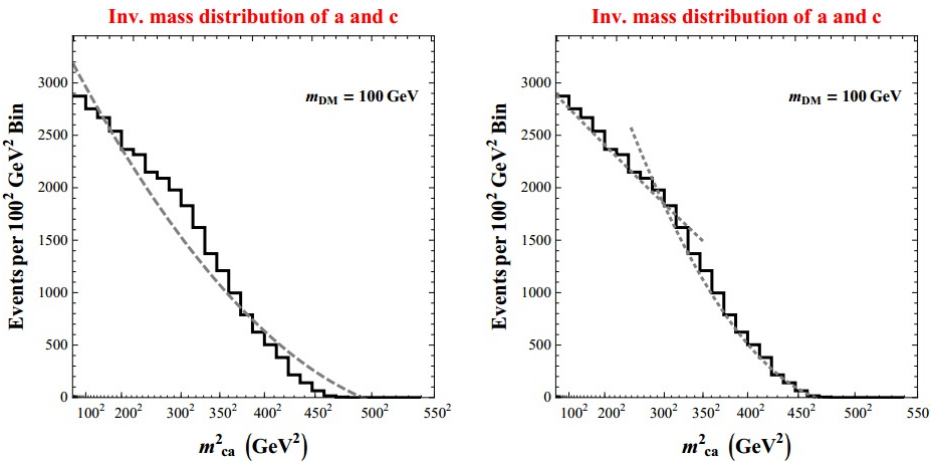

Figure 2.5: Invariant mass distribution of particles a and c, as in Figure 2.4, but with different chiral couplings. The cusp position is less apparent in this case but one can see (left panel) that a fit to a polynomial of second order as shown in Eq .(2.32) is not very good (that is, the Z_2 interpretation). On the right panel we show the same distribution, with a different fitting function for the left side of the distribution and the right side (see Eq. (2.39)), consistent with the existence of a cusp, *i.e.*, the Z_3 interpretation.

In Figure 2.5 we show the distribution (again obtained with `MadGraph/MadEvent` [60]) for the same decay chain as in Figure 2.4, but where the chiral structure of some couplings has been modified from before. We see that the cusp feature is now less apparent, but one also sees that a full fit to a polynomial of order two (left panel) is not as good as a *multiple-region* fit (right panel), where the first part of the distribution is fitted to a polynomial of order two (see first line of Eq. (2.39)), and the right side of the distribution is fitted to the functional form (with a logarithm) given in the second line of Eq. (2.39).

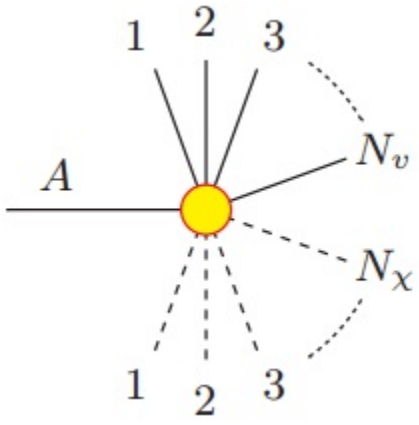

Figure 2.6: The generic decay topology under consideration.

Table 2.1: The number of inequivalent event topologies as a function of $1 \leq N_v \leq 4$ and $1 \leq N_\chi \leq 5$.

	N_χ				
N_v	1	2	3	4	5
1	1	2	4	8	16
2	2	7	20	55	142
3	4	20	78	270	860
4	8	55	270	1138	4294

2.4 Shape analysis

As advertised in Chapter 1, the analysis with the invariant mass variable can be generalized to more generic decay of a heavy resonance (denoted by A) into N_v visible particles and N_χ invisible particles, which is schematically illustrated in Figure 2.6. We consider the generic decay from Figure 2.6 without any prior assumptions about the decay topology or the number of invisibles. As seen in Table 2.1, the number of inequivalent decay topologies proliferates very quickly as we increase the number of particles in the final state. Let us begin with the simplest and most challenging case of $N_v = 2$, postponing $N_v > 2$ to a future study [61]. According to Table 2.1,

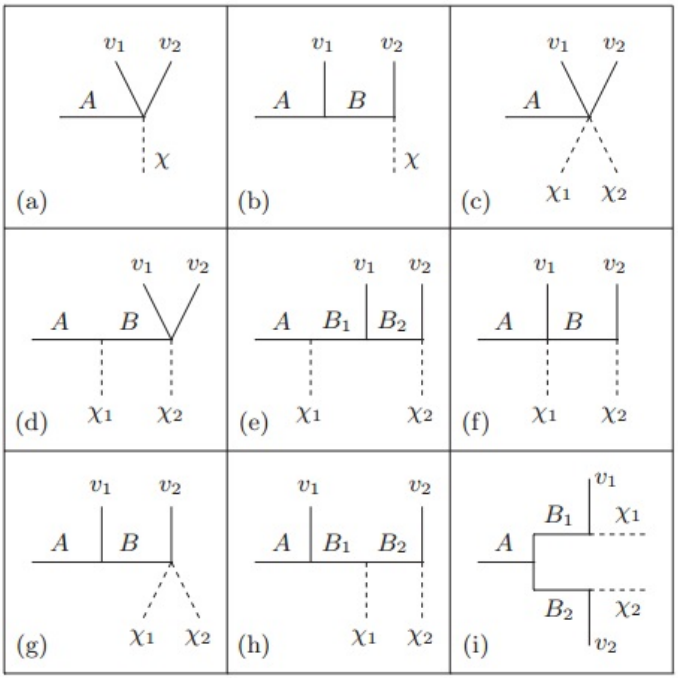

Figure 2.7: The nine $N_v = 2$ topologies with $N_\chi \leq 2$.

there are 2 topologies with $N_\chi = 1$, shown in Figure 2.7(a,b), and 7 topologies with $N_\chi = 2$, shown in Figure 2.7(c-i). Our main goal is to analyze and contrast the invariant mass distribution formed by the two visible particles v_1 and v_2[9] in each of those nine cases.

The differential distribution of the invariant mass $m \equiv m_{v_1 v_2}$ will be described by an analytical formula

$$\frac{dN}{dm} \equiv f(m; M_A, M_{B_i}, M_{\chi_j}), \tag{2.41}$$

[9]We note that the resonance A is in general allowed to be produced fully inclusively, with an arbitrary number of *additional* visible or invisible particles recoiling against A in the event. This precludes us from using the $\not{E}_T$ measurement, since it will be corrupted by the invisible recoils, which leaves us with $m_{v_1 v_2}$ as the only viable observable to study. The related combinatorial problem of partitioning the visibles in the event was addressed in [62, 64, 65, 81].

which is a function of the unknown masses. Given the general formula (2.41) for $f(m)$, we can easily obtain its kinematic endpoint

$$E \equiv \max\{m\} \tag{2.42}$$

and the location P of the peak of the $f(m)$ distribution

$$f(m = P) \equiv \max\{f(m)\}\,. \tag{2.43}$$

Let us also define the dimensionless derivative ratios

$$R_n \equiv -\left(\frac{m^n}{f(m)}\frac{d^n f(m)}{dm^n}\right)_{m=P}. \tag{2.44}$$

By definition, $R_1 = 0$, as long as $f(m)$ is continuously differentiable at $m = P$, while R_2 parametrizes the curvature of $f(m)$ at $m = P$.

The parameters E, P and R_n are in principle all experimentally measurable from the distribution (2.41). Traditional studies [66, 67] have always concentrated on measuring just the endpoint E, failing to utilize all of the available information encoded in the distribution $f(m)$. The endpoint approach gives a single measurement (2.42), which is clearly insufficient to determine the full spectrum of resonances involved in the decay chain of Figure 2.6. Here we propose to invoke the full shape (2.41) in the analysis. We envision that in practice this will be done by performing unbinned maximum-likelihood fits of (2.41) to the observed data. In order to illustrate the power of the method here, it is sufficient to consider just the additional individual measurements of P and R_2. Since they are obtained from the most populated bins near the peak, we can expect that they will be rather well measured. More importantly, the additional information about P and R_2 might be sufficient

to completely determine the mass spectrum (see Eqs. (2.52,2.53) below). But first we need to present our results for (2.41-2.44) in each of the nine cases in Figure 2.7.

The topology of Figure 2.7(a). For a three body decay to massless visible particles, one has

$$f(m; M_A, M_\chi) \sim m\, \lambda^{1/2}\left(m^2, M_A^2, M_\chi^2\right). \tag{2.45}$$

In this case

$$E = M_A - M_\chi, \tag{2.46}$$

$$P = \left[2M_A M_\chi \left(2 - \sqrt{1+3\alpha^2}\right)/(3\alpha)\right]^{1/2}, \tag{2.47}$$

$$R_2 = 6\left[1 + \left(1+3\alpha^2\right)^{-1/2}\right]^{-1}, \tag{2.48}$$

where

$$\alpha \equiv 2M_A M_\chi/(M_A^2 + M_\chi^2). \tag{2.49}$$

Contrary to popular belief, one can now solve for both masses M_A and M_χ, given two of the three measurements (2.46-2.48). For example, using the peak location P and the endpoint E, we find

$$M_A = \frac{E}{2}\left(\frac{P}{E}\sqrt{\frac{2-3(P/E)^2}{1-2(P/E)^2}} + 1\right), \tag{2.50}$$

$$M_\chi = \frac{E}{2}\left(\frac{P}{E}\sqrt{\frac{2-3(P/E)^2}{1-2(P/E)^2}} - 1\right). \tag{2.51}$$

Eqs. (2.50,2.51) offer a new method of determining *both* M_A and M_χ, which is a simpler alternative to the M_{T2} kink method of [7], since here we do not rely on the $\not{E}_T$ measurement at all, and do not require to reconstruct the decay chain on the other side of the event.

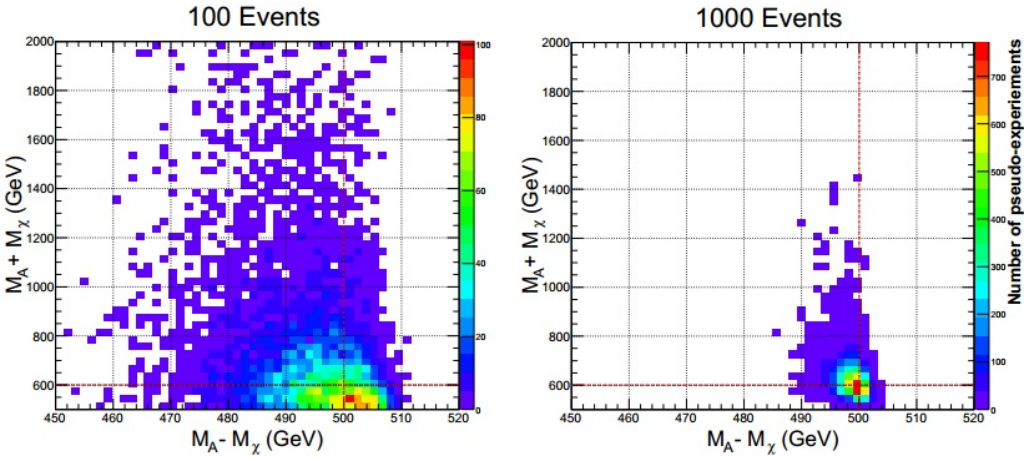

Figure 2.8: Distribution of M_A and M_χ found by a maximum-likelihood fit to Eq. (2.45) in 10,000 pseudo-experiments with 100 signal events (left) or 1000 signal events (right). The input study point has $M_A = 550$ GeV and $M_\chi = 50$ GeV.

In fact, one does not even need an endpoint measurement, since the peak location P and the curvature R_2 are sufficient for this purpose:

$$M_A = \frac{P}{\sqrt{2}}\left(\frac{6-R_2}{4-R_2} + \sqrt{\frac{12-R_2}{4-R_2}}\right)^{1/2}, \tag{2.52}$$

$$M_\chi = \frac{P}{\sqrt{2}}\left(\frac{6-R_2}{4-R_2} - \sqrt{\frac{12-R_2}{4-R_2}}\right)^{1/2}. \tag{2.53}$$

To the best of our knowledge (2.52,2.53) represent the first and only method in the literature which is capable of determining the complete mass spectrum in a short SUSY-like decay chain, without relying on any kinematic endpoint measurements.

In order to get a rough idea of the precision of these mass determinations, in Figure 2.8 on the left (right) we show the results from 10,000 pseudo-experiments with 100 (1000) signal events each. In each pseudo-experiment, the two masses M_A and M_χ are extracted from a maximum-likelihood fit of the simulated data to the full distribution (2.45). Figure 2.8 shows that, as expected, the mass difference is

measured quite well, at the level of $\sim 1\%$ with just 100 events. At the same time, the mass sum (or equivalently, the absolute mass scale) is also being determined, albeit less precisely: at the level of $\sim 30\%$ ($\sim 10\%$) with 100 (1000) events.

The topology of Figure 2.7(b). Here one obtains the celebrated triangular shape

$$f(m) \sim m, \tag{2.54}$$

$$E = P = \sqrt{(M_A^2 - M_B^2)(1 - M_\chi^2/M_B^2)}\,, \tag{2.55}$$

$$R_2 = \infty. \tag{2.56}$$

Unfortunately, the masses enter the shape (2.54) only through the combination (2.55), which is the single effective mass parameter accessible experimentally.

The topology of Figure 2.7(c). The shape is more conveniently given in integral form, which is easy to code up:

$$f(m) \sim m \int_{(M_{\chi_1}+M_{\chi_2})^2}^{(M_A-m)^2} \frac{ds}{s} \sqrt{\lambda(M_A^2,m^2,s)\lambda(s,M_{\chi_1}^2,M_{\chi_2}^2)}, \tag{2.57}$$

$$E = M_A - M_{\chi_1} - M_{\chi_2}. \tag{2.58}$$

The explicit formulas for P and (2.57) will be shown in [61]. The important point is that in principle all three masses M_A, M_{χ_1} *and* M_{χ_2} can be simultaneously determined from a fit of Eq. (2.57) to the data, just like in Figure 2.8 [61].

The topology of Figure 2.7(d). The invariant mass distribution of the visible particles v_1 and v_2 is not affected by the emission of invisible particles upstream and so this case is equivalent to the topology of Figure 2.7(a). The corresponding results can be obtained from (2.45-2.48) with the substitution $A \to B$, since now the role

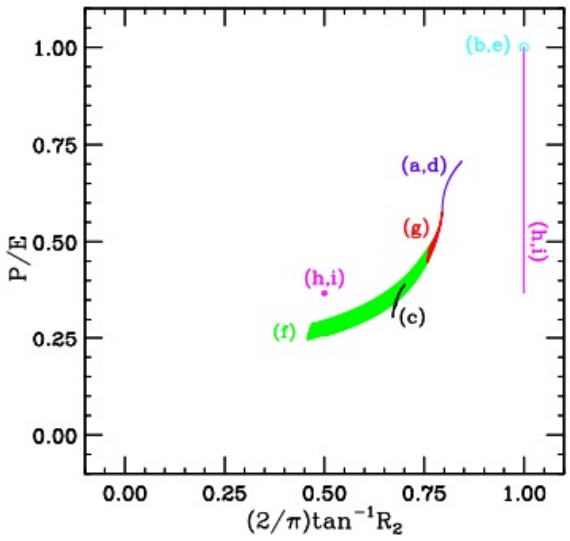

Figure 2.9: The topology disambiguation diagram. The different color-coded regions delineate the range of values for R_2 and P/E spanned by each decay topology from Figure 2.7.

of the parent resonance is played by the intermediate particle B. One would then be able to determine independently M_B and M_{χ_2}, while M_A and M_{χ_1} would remain unknown.

The topology of Figure 2.7(e). Similarly, this case is equivalent to Figure 2.7(b), with the substitutions $A \to B_1$, $B \to B_2$ and $\chi \to \chi_2$. Once again, the emission of the invisible particle χ_1 upstream is not observable. The only measurable parameter in this case will be the endpoint E.

The topology of Figure 2.7(f). We find

$$\begin{aligned} f(m) &\sim m\int_{M_B^2(1+\frac{m^2}{M_B^2-M_{\chi_2}^2})}^{(M_A-M_{\chi_1})^2} \frac{ds}{s}\sqrt{\lambda(s,M_A^2,M_{\chi_1}^2)} \\ &\sim -m\left[K_+K_- + \ln\left(\frac{K_++K_-}{K_+-K_-}\right)^{\frac{1}{2}(X_+^2+X_-^2)}\right. \\ &\qquad \left. + \ln\left(\frac{X_-K_+ - X_+K_-}{X_-K_+ + X_+K_-}\right)^{X_+X_-}\right], \end{aligned} \tag{2.59}$$

where

$$X_\pm \equiv M_A \pm M_{\chi_1}, \quad K_\pm \equiv \sqrt{X_\pm^2 - K^2(m)}, \tag{2.60}$$

$$K^2(m) \equiv M_B^2\left(1+\frac{m^2}{M_B^2-M_{\chi_2}^2}\right), \tag{2.61}$$

$$E = \sqrt{((M_A-M_{\chi_1})^2 - M_B^2)(1-M_{\chi_2}^2/M_B^2)}. \tag{2.62}$$

In this case, out of the 4 input masses entering the topology of Figure 2.7(f), one can measure three independent degrees of freedom, e.g. M_A/M_B, M_{χ_1}/M_B and $M_B^2 - M_{\chi_2}^2$.

The topology of Figure 2.7(g). The shape is described by

$$f(m) \sim m\int_{(M_{\chi_1}+M_{\chi_2})^2}^{M_B^2(1-\frac{m^2}{M_A^2-M_B^2})} \frac{ds}{s}\sqrt{\lambda(s,M_{\chi_1}^2,M_{\chi_1}^2)} \tag{2.63}$$

and it is easy to see that the results are obtained from (2.59-2.62) with the substitution $M_A \leftrightarrow -M_{\chi_2}$. In particular, the three measurable parameters in this case can be taken as M_{χ_1}/M_B, M_{χ_2}/M_B and $M_A^2 - M_B^2$.

The topology of Figure 2.7(h). This is the "sandwich" topology studied in

Section 2.3. The shape is given by

$$f(m) \sim \begin{cases} \eta\, m, & 0 \le m \le e^{-\eta}\, E, \\ m \ln\left(E/m\right), & e^{-\eta}\, E \le m \le E, \end{cases} \tag{2.64}$$

$$\eta \equiv \cosh^{-1}\left(\frac{M_{B_1}^2 + M_{B_2}^2 - M_{\chi_1}^2}{2M_{B_1}M_{B_2}}\right), \tag{2.65}$$

and

$$E = \left[e^{\eta}(M_A^2 - M_{B_1}^2)(M_{B_2}^2 - M_{\chi_2}^2)/(M_{B_1}M_{B_2})\right]^{1/2}, \tag{2.66}$$

$$P = \begin{cases} Ee^{-\eta}, & \eta < 1; \\ Ee^{-1}, & \eta \ge 1; \end{cases} \qquad R_2 = \begin{cases} \infty, & \eta < 1; \\ 1, & \eta \ge 1. \end{cases} \tag{2.67}$$

The distribution (2.64) exhibits a cusp at the non-differentiable point $m = e^{-\eta}E$. In this case, there are 5 mass inputs: M_A, M_{B_1}, M_{B_2}, M_{χ_1} and M_{χ_2}, but only two independent measurable parameters: η and E.

The topology of Figure 2.7(i). This is the "antler" topology which was studied in [37] for the symmetric case of $M_{B_1} = M_{B_2}$ and $M_{\chi_1} = M_{\chi_2}$. Here we generalize the result in [37] to arbitrary masses and find that $f(m)$ is given by the same expression (2.64), only this time

$$\eta \equiv \cosh^{-1}\left(\frac{M_A^2 - M_{B_1}^2 - M_{B_2}^2}{2M_{B_1}M_{B_2}}\right), \tag{2.68}$$

$$E = \left[e^{\eta}(M_{B_1}^2 - M_{\chi_1}^2)(M_{B_2}^2 - M_{\chi_2}^2)/(M_{B_1}M_{B_2})\right]^{1/2} \tag{2.69}$$

and identical expressions (2.67) for P and R_2. Just like the case of Figure 2.7(h), out of the 5 mass inputs, η and E are the only two measurable mass parameters. Table 2.2 summarizes the final tally of input particle masses and independent measurable parameters for each topology.

Table 2.2: The number of mass inputs N_m for each topology in Figure 2.7 and the number of independent measurable parameters N_p in the definition of $f(m)$.

Topology	(a,d)	(b,e)	(c)	(f,g)	(h,i)
N_m	2	3	3	4	5
N_p	2	1	3	3	2

Each topology from Figure 2.7 also maps onto a restricted region in the $(R_2, P/E)$ plane, as shown in Figure 2.9 (for convenience, instead of $R_2 \in (0, \infty)$, in the figure we plot $\frac{2}{\pi} \tan^{-1} R_2 \in (0, 1)$). For example, the cyan circle at $(1, 1)$ marks the prediction for the two topologies of Figure 2.7(b,e), while the magenta dot at $(0.5, 0.37)$ and the magenta vertical line correspond to the two topologies of Figure 2.7(h,i). The blue (red, green, black) points refer to the topologies of Figure 2.7(a,d) (Figure 2.7(g), Figure 2.7(f), Figure 2.7(c)). Figure 2.9 demonstrates that with the three measurements E, P and R_2, one can already begin to constrain qualitatively the allowed event topologies.

Chapter 3: Stransverse mass/M_{T2}

3.1 Overview

In this chapter, we investigate the way of determining the physical properties of invisible particles using the stransverse mass/M_{T2} variable. Again, like the previous chapter we examine the decay of (pair-produced) heavy particles, which are charged under the dark matter stabilization and SM symmetries, into DM candidate(s) plus the associated SM/visible particles (inside the detector). Therefore, the M_{T2} variable will be constructed by the full information of all relevant visible decay products along with the overall missing transverse energy/momentum. In other words, for each event all available information on the transverse plane from the two decay chains comes into play to give rise to a M_{T2} value. We emphasize that in this sense the M_{T2} method can be complementary to the invariant mass method discussed in Chapter 2, e.g., the case with only a *single* visible particle in a decay chain, in which the information from the invariant mass is of no more interest.

We first begin with a short review of the stransverse mass/M_{T2} variable for the Z_2 case, and then apply the same idea to the Z_3 case. Since the Z_3 symmetry allows two DM particles from the decay of a single mother particle, we categorize each event according to the number of total DM particles in the final state (i.e.,

two, three or four DM particles). Nevertheless, we expand the relevant argument hypothesizing that there exists only a single DM particle in each decay side. We then demonstrate that three M_{T2} distributions are available and their kinematic endpoints provide independent pieces of information, i.e., richer structure than that in Z_2 models. We also provide the conditions to give rise to a kink structure in the plot of the maximum M_{T2} value versus the trial DM mass for the cases with more than two DM particles in the final state: obviously, such situations are absent in Z_2 models.

Once the general theory consideration is completed, we move onto the detailed applications. As the first example, we consider the easier case where the decay chains with two DM particles involve a different SM/visible state from those with one DM particle. In Z_3 models, typically three *separate* M_{T2} distributions can be obtained whereas in Z_2 models, only one distribution is available. Also we mention the way of measuring the masses of the mother and the DM particles based on the theory argument previously. On the contrary, once the visible state associated with two DM particles is *in*distinguishable from that associated with one DM particle, even in Z_3 models only a single M_{T2} distribution is available. We therefore come up with another technique to separate each type of events, which enables us to distinguish Z_2 and Z_3 models. In all examples above, we make the simple assumption that the intermediate particles in the decay process are *off*-shell.

3.2 A review of M_{T2} for Z_2 models

For simplicity, in this chapter

- we consider pair-production of a *single* type of mother particle which is charged under the DM stabilization symmetry.

We also assume that the *total* transverse momentum of the two mother particles produced in an event is zero, for example, we neglect any initial/final state radiation. In Z_2 models, each such mother decays into SM/visible particle(s) and one DM/invisible particle[1]. Furthermore, it is assumed

- we know which *visible* particle(s) originate from which decay chain.[2] For example, if the pair-produced mother particles are boosted sufficiently, their decay products are likely to be collimated so that the visible particles coming from the same decay chain are detected in the same hemisphere in the collider. For alternate methods of determining the correct assignment of visible particles to the two decay chains, see reference [64].

The M_{T2} variable [4] is a generalization of the transverse mass[3] to this case. Specifically, for each event, it is defined to be a minimization of the maximum of the two transverse masses in each decay chain under the constraint that the sum of all the

[1]We assume that there is only one type of the DM particle in this (and similarly the Z_3) model so that the invisible/DM particles in each decay chain are identical.

[2]Of course, for Z_3 models, we do not know which decay chain emits one or two DM particles.

[3]Of course, the usual transverse mass assumes only a single mother particle.

transverse momenta of the visible and invisible particles vanishes [4]:

$$M_{T2} \equiv \min_{\mathbf{p}_T^{v(1)}+\mathbf{p}_T^{v(2)}+\tilde{\mathbf{p}}_T^{(1)}+\tilde{\mathbf{p}}_T^{(2)}=0} \left[\max\left\{M_T^{(1)},\ M_T^{(2)}\right\}\right] \tag{3.1}$$

where $\mathbf{p}_T^{v(i)}$ denote the vector *sum* of visible transverse momenta and $\tilde{\mathbf{p}}_T^{(i)}$ denote the transverse momentum of the invisible particle in the ith decay chain ($i = 1,\ 2$): the minimization is performed over the latter momenta. $M_T^{(i)}$ is the usual transverse mass:

$$\left(M_T^{(i)}\right)^2 = \left(m_T^{v(i)}\right)^2 + \tilde{m}^2 + 2\left(E_T^{v(i)}\tilde{E}_T^{(i)} - \mathbf{p}_T^{v(i)} \cdot \tilde{\mathbf{p}}_T^{(i)}\right) \tag{3.2}$$

where $E_T^{v(i)}$ and $m_T^{v(i)}$ are (respectively) the transverse energy and transverse mass formed by all visible particles belonging to the same decay chain. The variables with a tilde represent the corresponding quantities formed by the invisible particle in the same decay chain. Note that the mass of the invisible particle $\tilde{m}$ should be regarded as a unknown/free parameter because we are not aware of it in advance, and henceforth we call it "trial" DM mass. In this sense M_{T2} should be considered to be a function of the trial DM mass $\tilde{m}$, and its maximum value among many events (which will be used extensively in the following) is defined as

$$M_{T2}^{\max}(\tilde{m}) = \max_{\text{many events}} \left[M_{T2}(\tilde{m})\right]. \tag{3.3}$$

Obviously $M_{T2}^{\max}(\tilde{m})$ is also a function of the trial DM mass (see Chapter B for details). An important result to be noted is that if there are a sufficient number of events and the actual DM mass is substituted into $\tilde{m}$, then the above-given $M_{T2}^{\max}$ becomes the actual mass of the pair-produced mother particles [4]:

$$M_{T2}^{\max}(\tilde{m} = m_{DM}) = M \tag{3.4}$$

where M and m_{DM} indicate the true masses of the mother and the DM particles, respectively.

In order to see how this M_{T2} analysis is applied to realistic situations, we first take the case where there exists a single visible/SM particle in each decay chain, and then move on to the case where there exist more than one visible/SM particle in each decay chain. A similar analysis can be done for mixed case, i.e., one visible particle on one side and more than one on the other.

3.2.1 One visible/SM particle in each decay chain

In this case the upper edge in M_{T2} distribution is obtained by the "balanced" [4, 7] solution (see Chapter B for details).

$$M_{T2}^{\max} = M_{T2}^{\max,bal} = \sqrt{\frac{(M^2 - m_{DM}^2)^2}{4M^2}} + \sqrt{\frac{(M^2 - m_{DM}^2)^2}{4M^2} + \tilde{m}^2} \tag{3.5}$$

Here (and henceforth)

- we assume that all visible particles are massless for simplicity.

As mentioned earlier, the above-given upper edge is a function of the trial DM mass $\tilde{m}$ and one can see that it reduces to the true mother mass M with $\tilde{m}$ equal to the true DM mass m_{DM}. The left panel of Figure 3.1 shows the above theoretical prediction for the location of maximum M_{T2} for Z_2 models as a function of the trial mass $\tilde{m}$. We used 400 GeV and 100 GeV as mother and DM particle masses. As expected from Eq. (3.5), the curve in the figure "smoothly" increases with $\tilde{m}$ (cf. the following section), and that the $M_{T2}^{\max}$ value corresponding to $\tilde{m} = m_{DM}$ (where

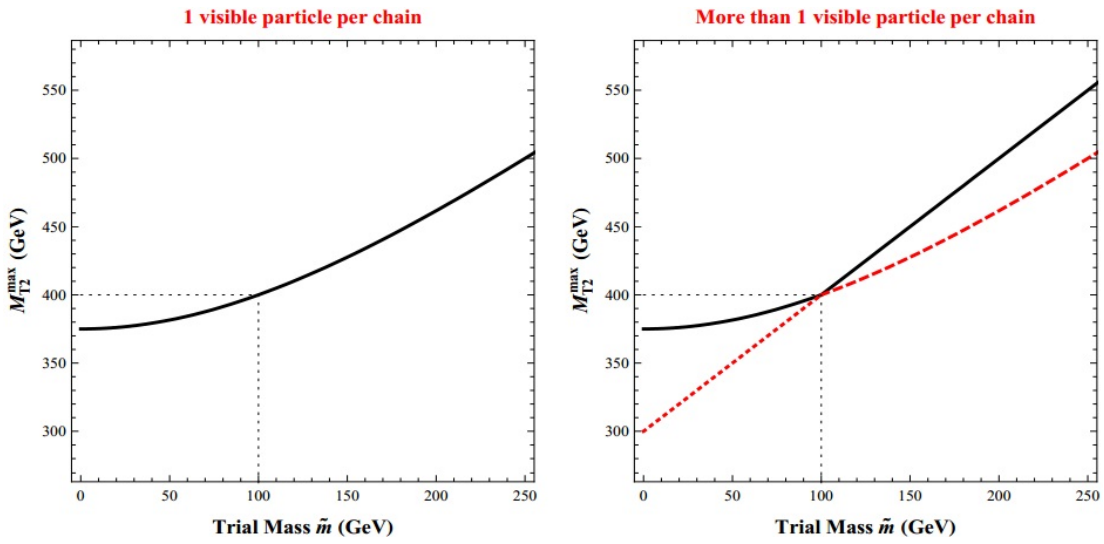

Figure 3.1: Theoretical expectation of $M_{T2}^{\max}$ versus the trial mass $\tilde{m}$ for Z_2 events. The masses of the mother and the DM particles are 400 GeV and 100 GeV, respectively. The left panel shows the case where there exists only a single visible particle per chain.The right panel shows the case where there exist more than one visible particle per decay chain. In both panels, the solid black curve represents the overall/net upper edge, $M_{T2}^{\max}$. In the right panel, the dotted straight line which extends into the right-hand part of the solid line is the $M_{T2}^{\max}$ for the unbalanced solution, whereas the dashed line which extends into the left-hand part of the solid line is that for the balanced solution.

here $m_{DM} = 100$ GeV) is the same as the true mother particle mass (where here $M = 400$ GeV: see the black dotted lines).

3.2.2 More than one visible/SM particle in each decay chain

Once there exists more than one visible particle per decay chain, another type of solution to M_{T2}, denoted by "unbalanced" [4, 7], arises. If

- we assume that the intermediate particles in the decay chains are *off*-shell

(as we will for most of this chapter), the balanced solution in this case is still given by Eq. (3.5), and the unbalanced solution is as follows[4]:

$$M_{T2}^{\max,unbal} = M - m_{DM} + \tilde{m}. \tag{3.6}$$

Hence the overall upper edge in the M_{T2} distribution is determined by a "competition" between balanced and unbalanced solutions:

$$\begin{aligned} M_{T2}^{\max} &= \max\left[M_{T2}^{\max,bal},\ M_{T2}^{\max,unbal}\right] \\ &= \begin{cases} M - m_{DM} + \tilde{m} & \text{for } \tilde{m} \geq m_{DM} \\ \sqrt{\frac{(M^2-m_{DM}^2)^2}{4M^2}} + \sqrt{\frac{(M^2-m_{DM}^2)^2}{4M^2} + \tilde{m}^2} & \text{for } \tilde{m} \leq m_{DM}. \end{cases} \end{aligned} \tag{3.7}$$

Note that the $M_{T2}^{\max}$ shows different functional behaviors depending on the relative size of the trial DM mass to the true DM mass. As a result, $M_{T2}^{\max}$ is no longer smoothly increasing with $\tilde{m}$ in contrast to the case with one visible/SM per decay chain. Instead, there arises a "kink" at the location of the actual DM mass, with the corresponding $M_{T2}^{\max}$ being the actual mother mass [7][5]. This is illustrated in the right panel of Figure 3.1 where the upper edges for the two possible types of solutions $M_{T2}^{\max,unbal}$ and $M_{T2}^{\max,bal}$ are shown by a straight line (i.e., the dotted line, which extends into the right-hand part of the solid line) and a dashed curve (which

[4]Of course, in general, one can find the expressions for both the balanced and the unbalanced solutions in the case of *on*-shell intermediate particles [7].

[5]A similar kink also appears for the case of *one* visible particle in each decay chain *if* the total transverse momentum of the two mother particles is *non*-zero, for example, in the presence of initial/final state radiation (see first and second references in [9]), but (as mentioned earlier) we neglect this possibility for simplicity.

extends into the left-hand part of the solid curve), respectively. The upper edge in the M_{T2} distribution is given by the larger of these two values, i.e., the black solid curve, and shows a kink (indicated by the black dotted lines), at $\tilde{m} = 100$ GeV and $M_{T2}^{\max} = 400$ GeV (as expected).

3.3 M_{T2} for Z_3 models

For Z_3 models, each mother particle can emit either one or two DM particles so that there exist two, three, or four DM particles in the final state (for pair-production of the mother particles) while there are only two DM particles for Z_2 models. We therefore expect richer structures in the M_{T2} distribution for Z_3 models. Here

- we take as an ansatz only a *single* DM particle in each decay chain for the sole purpose of defining M_T, even if there could be two DM particles in either or both of the two decay chains.

We do so for the following two reasons. Firstly, in the real collider experiment, there is (a *priori*) no clear information on the number of invisible particles involved in the decay process of interest so that each individual decay chain with only one DM is a natural (starting) assumption. Moreover, one can naturally expect (and we will show) that decay events from Z_3 models will show different features in the M_{T2} analysis compared with those for Z_2 models. Therefore, starting with a Z_2 assumption and deriving a "contradiction" in the M_{T2} analysis, we can distinguish Z_3 models from Z_2 ones (which is our primary goal here). In this context, we call

such an analysis imposing one-DM-per-chain assumption the "naive" M_{T2} analysis.

For a more systematic consideration let us define the three different events having the different number of DM particles as E_2, E_3, and E_4-type, respectively, i.e., each subscript on E simply implies the total number of DM particles in the final state: see Figure 3.2, where $\mathrm{SM}_{1,\,2}$ denote the visible/SM final states (irrespective of the actual number of particles in the state) in the decay chains with one and two DM (respectively)[6]. Here the red dashed lines denote any particles charged under dark matter stabilization symmetry (in this section Z_3 symmetry) while the black solid lines/arrows denote any visible/SM particles. One should note that E_4 type events represent the case with 2 DM particles in each decay chain. Also, both decay chains (with one and two DM) might not exist for a *specific* mother so that all three types of events might not occur. Like in Z_2 models, we start with the case with one visible/SM particle in each decay chain, and we consider the case with more than one visible/SM particle in each decay chain in the following subsection. While doing so, we see how the M_{T2} analysis applied to Z_3 models contrasts with Z_2 models.

3.3.1 One visible/SM particle in each decay chain

In this case the upper edge in the (naive) M_{T2} distribution is determined only by the balanced solution like Z_2 models, and the analytic expressions for the three

[6]These two SM final states might not or might be identical: we will return to these two possibilities in the next two sections (respectively).

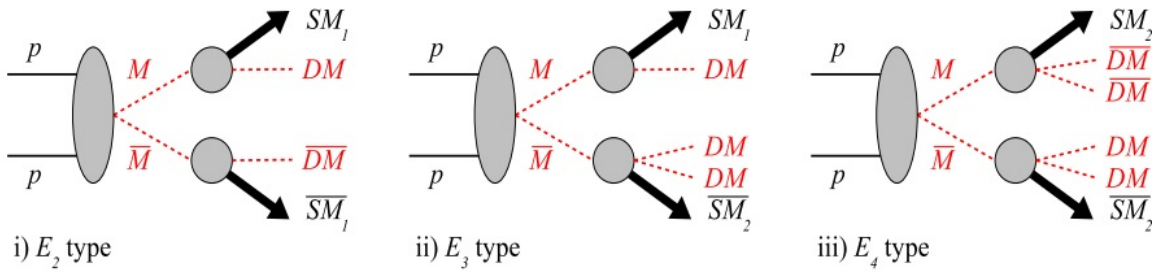

Figure 3.2: The three types of events in Z_3 models, based on the total number of DM in the event. "M" denotes the mother particle. Each SM final state can have more than one particle. Note that, based simply on the Z_3 symmetry, if a mother decays into DM, then the *same* mother decays into two *anti*-DM in the other decay chain. Since DM and anti-DM have same mass and are *not* detected, we neglect this distinction between the two henceforth (we already did so thus far). For simplicity, we will also henceforth not differentiate between SM and $\bar{\text{SM}}$ or between M and $\bar{M}$.

type events are given as follows (see Chapter B for details):

$$M_{T2,E_2}^{\max} = M_{T2,E_2}^{\max,bal} = \sqrt{\frac{(M^2 - m_{DM}^2)^2}{4M^2}} + \sqrt{\frac{(M^2 - m_{DM}^2)^2}{4M^2} + \tilde{m}^2} \quad \text{for } E_2 \quad (3.8)$$

$$M_{T2,E_3}^{\max} = M_{T2,E_3}^{\max,bal} = \sqrt{\frac{(M^2 - m_{DM}^2)(M^2 - 4m_{DM}^2)}{4M^2}} + \sqrt{\frac{(M^2 - m_{DM}^2)(M^2 - 4m_{DM}^2)}{4M^2} + \tilde{m}^2} \quad \text{for } E_3 \quad (3.9)$$

$$M_{T2,E_4}^{\max} = M_{T2,E_4}^{\max,bal} = \sqrt{\frac{(M^2 - 4m_{DM}^2)^2}{4M^2}} + \sqrt{\frac{(M^2 - 4m_{DM}^2)^2}{4M^2} + \tilde{m}^2} \quad \text{for } E_4 \quad (3.10)$$

As a reminder, the events with E_2, E_3 and E_4 represents events with two, three and four dark matter candidates. Note that Eq. (3.8) has the same form as Eq. (3.5) in Z_2 models because E_2 type events also contain two DM particles in the final state (just like Z_2 models) whereas the other two types of events do *not* appear in Z_2

models so that the corresponding Eqs. (3.9) and (3.10) (and similar ones later) are new/do not appear in previous literature. Substituting $\tilde{m} = m_{DM}$ in Eq. (3.8) gives the true mother mass M for the value of $M_{T2}^{\max}$ (as expected), but the other two equations give a combination of the true mother and DM masses rather than the true mother mass. Actually, this is not surprising because we have used the naive M_{T2} variable for the $E_{3\,4}$-type events in Z_3 models, whereas the actual physics is different from the physics under which our M_{T2} variable is defined. For example, for E_3 type events there is an asymmetry between the final states of the two decay chains, which is caused by adding one more DM to either of the two decay chains. For E_4 type events, even though the two decay chains have symmetric final states, the "effective" DM mass is twice the true DM mass so that the true mother mass (for the value of $M_{T2}^{\max}$) is in fact obtained by setting $\tilde{m} = 2m_{DM}$ instead as clearly seen from Eq. (3.10).

All of the theoretical predictions mentioned above are demonstrated in the left panel of Figure 3.3. Again, we used 400 GeV and 100 GeV as mother and DM masses. The black solid, the red dashed, and the blue dot-dashed curves represent the theoretical expectations of $M_{T2}^{\max}$ for E_2, E_3, and E_4 type events, respectively (the curve for E_2-type events is of course the same as in right-hand side of Figure 3.1). As discussed above, the $M_{T2}^{\max}$ for E_2 type events corresponds to the true mass of the mother particle (here 400 GeV) with the trial DM mass equal to the true DM mass (here 100 GeV) whereas E_4 type events do it for twice the DM mass (here 200 GeV), as shown by the dotted/black lines.

In addition, there are a couple of features to be noted; there is no kink arising

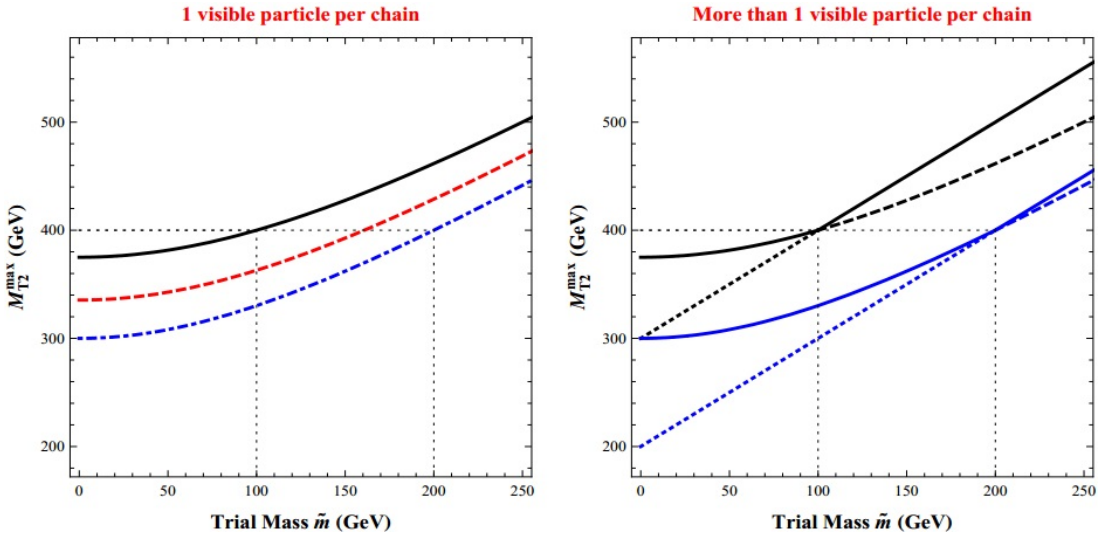

Figure 3.3: Theoretical expectation of $M_{T2}^{\max}$ versus the trial mass $\tilde{m}$ for Z_3 model. The masses of the mother and the DM particles are 400 GeV and 100 GeV, respectively. The left panel shows the case where there exists only a single visible particle per chain. The black, red, and blue curves are showing the corresponding $M_{T2}^{\max}$ values to E_2, E_3, and E_4 type events over $\tilde{m}$, respectively. The right panel shows the case where there exist more than one visible particle per decay chain. The overall upper edges, $M_{T2}^{\max}$ for E_2 and E_4 type events, are given by the solid black and blue curves, whereas the balanced and unbalanced solutions are denoted by the dashed and dotted curves (respectively) which merge into the solid curves on the right (left)-hand part. The corresponding plot for E_3 type events can be found in the next figure.

in the $M_{T2}^{\max}$ curves for $E_{3,4}$ -type events just like the case of a single visible particle per decay chain in Z_2 models (or E_2-type event in Z_3 models). Secondly for any given $\tilde{m}$, the $M_{T2}^{\max}$ values form a hierarchy of

$$M_{T2,E_2}^{\max} > M_{T2,E_3}^{\max} > M_{T2,E_4}^{\max}. \tag{3.11}$$

3.3.2 More than one visible/SM particle in each decay chain

Once more visible particle(s) are added in each decay chain, one could naturally expect that a kink appears like in Z_2 models. The reason is that, just like for Z_2 models, the maximum unbalanced solutions take part in determining the overall upper edge in the M_{T2} distribution together with the balanced solutions. It turns out, however, that this expectation is true only for E_2 and E_4 type events which we discuss to begin with. Again, assuming the intermediate particles are *off*-shell the maximum values of the balanced solutions for E_2 and E_4 type events are simply given (as for the one visible particle case) by Eqs. (3.8) and (3.10), respectively, and those of the unbalanced solutions are given as follows:

$$M_{T2,E_2}^{\max,unbal} = M - m_{DM} + \tilde{m} \qquad \text{for } E_2 \tag{3.12}$$

$$M_{T2,E_4}^{\max,unbal} = M - 2m_{DM} + \tilde{m} \qquad \text{for } E_4. \tag{3.13}$$

Here Eq. (3.12) is of exactly the same form as Eq. (3.6) due to the similarity between the decay structures for Z_2 models and E_2 type events while Eq. (3.13) for E_4-type events is relevant only for Z_3 models, i.e., it is not present in Z_2 models. More quantitatively, the above-given two equations differ by m_{DM} for any given $\tilde{m}$ because one more DM particle is emitted in both decay chains for E_4 type events compared with E_2 type events (see Eqs. (B.16) and (B.36) in the Chapter B).

As mentioned for Z_2 models, the maximum M_{T2} values are given by the larger of the balanced and unbalanced solutions: for E_2 type events as in Eq. (3.7), and

for E_4 type events by:

$$
\begin{aligned}
M_{T2,E_4}^{\max} &= \max\left[M_{T2,E_4}^{\max,bal},\ M_{T2,E_4}^{\max,unbal}\right] \\
&= \begin{cases} M - 2m_{DM} + \tilde{m} & \text{for } \tilde{m} \geq 2m_{DM} \\ \\ \sqrt{\frac{(M^2-4m_{DM}^2)^2}{4M^2}} + \sqrt{\frac{(M^2-4m_{DM}^2)^2}{4M^2} + \tilde{m}^2} & \text{for } \tilde{m} \leq 2m_{DM}. \end{cases}
\end{aligned}
\tag{3.14}
$$

Note that there is also a kink for E_4-type events as seen from Eq. (3.14), but at $\tilde{m} = 2m_{DM}$ (i.e., not m_{DM}), because the effective DM mass for E_4 is given by $2m_{DM}$.

The right panel of Figure 3.3 illustrates the above theoretical considerations for E_2 and E_4 type events (of course the curve for E_2-type events is same as right-hand side of Figure 3.1). As before, the two straight dotted lines which extend into the right-hand parts of the solid lines indicate the maximum values of the unbalanced solutions while the two dashed curves which extend into left-hand parts of the solid curve indicate the maximum values of the balanced solutions. The actual upper edge in the M_{T2} distribution for any $\tilde{m}$ is given by the black (for E_2 type events) or blue (for E_4 type events) solid curves. Identifying the location of the kink in E_2-type events and its corresponding $M_{T2}^{\max}$ enables us to determine the masses of the mother and the DM particles separately (just like in Z_2 models). The figure also shows the kink for E_4-type events, but located at $\tilde{m} = 200$ GeV (i.e., $2m_{DM}$, as expected) and $M_{T2}^{\max} = 400$ GeV. This observation can be used as a cross-check for the determination of M and m_{DM} based on E_2-type events (again, this feature is new in Z_3 models relative to Z_2).

On the other hand, as far as E_3 type events (which are absent in Z_2 models)) are concerned, whether or not there exists a kink depends on the mass hierarchy between mother and DM particles (see Chapter. C for details). Again, assuming *off*-shell intermediate particles the maximum balanced solution is simply given by Eq. (3.9) (just like the case of one visible particle per decay chain), whereas the maximum unbalanced solution has the same form as that for E_2 type events because one of the two decay chains still emits a single DM particle in the final state (see Eqs. (B.16) and (B.36) in the Chapter B).

$$M_{T2,E_3}^{\max,unbal} = M - m_{DM} + \tilde{m} \qquad \text{for } E_3 \tag{3.15}$$

If the ratio of the DM mass to the mother mass is larger than $(\sqrt{3}-1)/2$, it turns out that the maximum unbalanced solution given in Eq. (3.15) is always bigger than the maximum balanced solution given in Eq. (3.9) so that

$$\begin{aligned} M_{T2,E_3}^{\max} &= \max\left[M_{T2,E_3}^{\max,bal},\ M_{T2,E_3}^{\max,unbal}\right] = M - m_{DM} + \tilde{m} \\ &\text{for } \frac{m_{DM}}{M} \geq \frac{\sqrt{3}-1}{2} \text{ and for all } \tilde{m}. \end{aligned} \tag{3.16}$$

The left panel of Figure 3.4 clearly confirms our expectation (based on above equation) that there occurs no kink in the upper edge of M_{T2} as a function of the trial DM mass, i.e., the upper edge in the M_{T2} distribution is always determined by the unbalanced solution (black solid line), not by the balanced solution (red dashed curve). Here we adopted $M = 400$ GeV and $m_{DM} = 150$ GeV, and thus the ratio between them is obviously larger than $(\sqrt{3}-1)/2$.

On the other hand, once the ratio of the DM to the mother mass is smaller than $(\sqrt{3}-1)/2$, the competition between the balanced and the unbalanced solutions

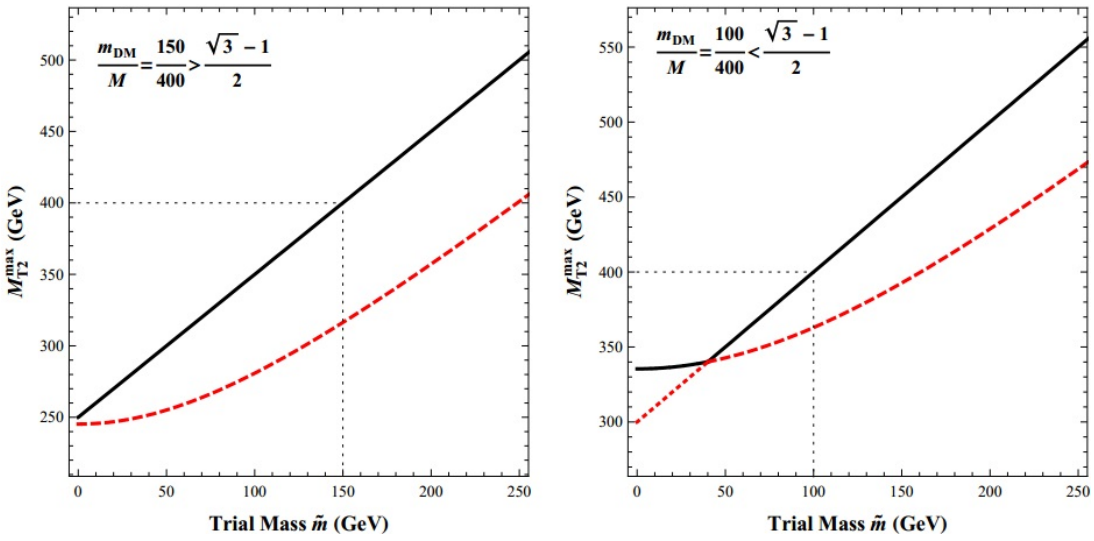

Figure 3.4: Theoretical expectation of $M_{T2}^{\max}$ versus the trial mass $\tilde{m}$ for E_3 type events. The mass of the mother particle is 400 GeV for both cases, but the masses of the DM particle to be used are 150 GeV and 100 GeV for the left panel and the right panel, respectively. For both cases, the black solid lines give the maximum of M_{T2}, whereas the dashed curves give the maximum for the balanced solution. The maximum for the unbalanced solution coincides with the solid line on the left panel, whereas on the right panel, it is given by the dotted straight line (which extends into the right-hand part of the solid line).

results in

$$
\begin{aligned}
M_{T2,E_3}^{\max} &= \max\left[M_{T2,E_3}^{\max,bal},\ M_{T2,E_3}^{\max,unbal}\right] \\
&= \begin{cases} M - m_{DM} + \tilde{m} & \text{for } \tilde{m} \geq m' \\ \sqrt{\frac{(M^2-m_{DM}^2)(M^2-4m_{DM}^2)}{4M^2}} + \sqrt{\frac{(M^2-m_{DM}^2)(M^2-4m_{DM}^2)}{4M^2} + \tilde{m}^2} & \text{for } \tilde{m} \leq m' \end{cases} \\
&\quad \text{and for } \frac{m_{DM}}{M} \leq \frac{\sqrt{3}-1}{2}
\end{aligned}
\tag{3.17}
$$

where

$$
m' = \frac{(M - m_{DM})\left(\sqrt{(M^2 - m_{DM}^2)(M^2 - 4m_{DM}^2)} - M(M - m_{DM})\right)}{2M(M - m_{DM}) - \sqrt{(M^2 - m_{DM}^2)(M^2 - 4m_{DM}^2)}}. \tag{3.18}
$$

We see that there is a kink at $\tilde{m} = m'$. Here m' is *not* simply the true DM mass but it is given by a combination of the true mother and DM masses (in fact, it is smaller than the true DM mass), which is clearly different from that in Z_2 models. The functional behavior of $M_{T2}^{\max}$ for this case is shown in the right panel of Figure 3.4. Here we took $m_{DM} = 100$ GeV which makes the ratio smaller than $(\sqrt{3}-1)/2$. As before, the maximum M_{T2} for the balanced and unbalanced solutions are shown by the dashed and dotted curves (which extend into the black solid curve to the RHS and LHS). The final maximum M_{T2} is given by the larger of these two solutions (black solid curve) which clearly shows a kink at a value of $\tilde{m}$ which is different from the actual DM mass $m_{DM} = 100$ GeV (shown by the vertical black dotted line) as expected based on above discussion. Of course, we can still evaluate the masses of the mother and the DM particles (using E_3-type events only) by obtaining $M_{T2}^{\max}$ and m' from the above M_{T2} analysis, substituting them into Eqs. (3.17) and (3.18), and solving those two equations about M and m_{DM}.

Next, let us investigate the hierarchy among the three $M_{T2}^{\max}$ values for E_2, E_3, and E_4 type events. Although a bit more complicated than the one visible particle case, it is nonetheless straightforward to derive this hierarchy based on above equations, We have a following hierarchy among the $M_{T2}^{\max}$ values for the three types (cf. the one visible particle case shown in Eq. (3.11)):

$$\begin{aligned} M_{T2,E_2}^{\max} = M_{T2,E_3}^{\max} > M_{T2,E_4}^{\max} \qquad & \text{for } \tilde{m} \geq m_{DM} \\ M_{T2,E_2}^{\max} > M_{T2,E_3}^{\max} > M_{T2,E_4}^{\max} \qquad & \text{for } \tilde{m} \leq m_{DM}. \end{aligned} \tag{3.19}$$

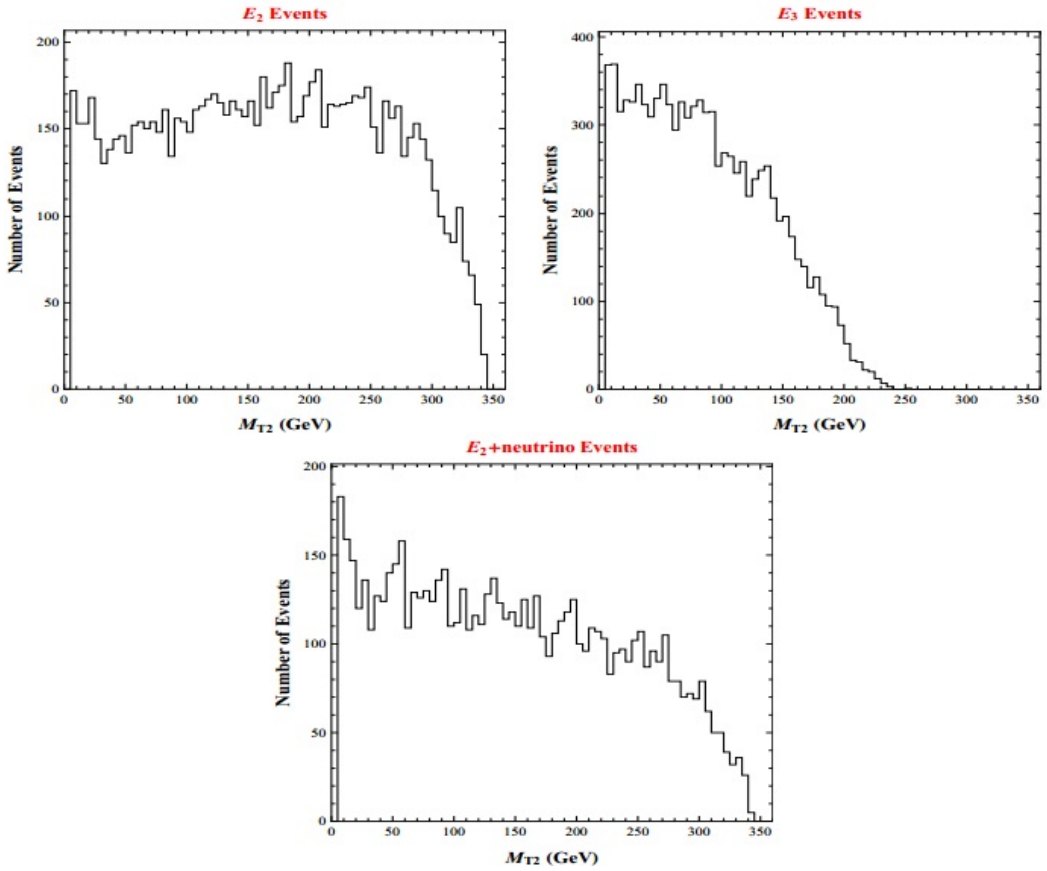

Figure 3.5: The M_{T2} distributions for E_2 (top left) and E_3 (top right) type events and $E_2+\nu$ events (bottom). The mother and the DM particle masses are 400 GeV and 150 GeV, respectively, and the trial DM mass to be used is 6 GeV.

3.3.3 Shapes of M_{T2} distributions

Before closing the present section, let us examine the shape of the M_{T2} distributions for Z_3 cases. For this purpose we simulated events using `MadGraph/MadEvent` [60]. Here and in sections 3.5.1.1 and 3.5.1.2, we make the following assumptions (mostly for simplicity): (a) effects of spin correlations are neglected; (b) the beam is proton-proton with 14 TeV total energy in the center of mass frame (motivated by

the LHC parameters); (c) the non-colored scalar mother particles are pair-produced via s-channel and finally (d) only the *relative* values of the number of events (on vertical scale) are meaningful.

For all the simulations in *this* section, the masses of the mother and the DM particles used in the (toy) model are 400 GeV and 150 GeV, respectively, we took a *single* visible particle per decay chain for simplicity. The upper left panel of Figure 3.5 demonstrates the M_{T2} distribution for E_2 type events. Obviously, this is similar to the M_{T2} distribution for events in Z_2 models [4, 7], which is not surprising because E_2 type events also has only two dark matter particles in the final state like Z_2. The (naive) M_{T2} distribution for E_3 type events illustrated in the upper right panel of Figure 3.5 has two notable features. As expected from the analytic expressions given before, first of all, the location of the upper edge is clearly lower than that for E_2 type events (or for Z_2 models). Secondly, the shape of M_{T2} distribution for E_3 type events shows a long tail near the upper edge compared with E_2 type events (which have relatively sharp upper edge): this is because more physical constraints (e.g., rapidity) between decay products should be satisfied in E_3 type events in order that they form a kinematic configuration to give maximum M_{T2}, thereby reducing the corresponding number of events near $M_{T2}^{\max}$.

This feature of a (relatively) long tail is also true for a special case in Z_2 models with three invisible particles in the full event one of which is a (massless) SM neutrino, i.e., with one DM in one decay chain, but one DM and a neutrino in the other (henceforth we call it $E_2 + \nu$ events)[7]. The bottom panel of Figure 3.5

[7] M_{T2} distributions for such events have been studied in second and third references of [4] and

demonstrates the M_{T2} distribution for $E_2+\nu$ events, assuming intermediate particles are off-shell [8]. At the upper edge it shows a tail which is longer than that for E_2 type events (or neutrino-less events in Z_2 models), but which is not as long as that for E_3 type events[9]. Such a shape is not surprising because the additional invisible particle (neutrino) in $E_2 + \nu$ vs. E_2-type events is massless so that $E_2 + \nu$ events can be understood as a transitional type between E_2 and E_3 type events. However, it is crucial to note that the location of the upper edge for the $E_2 + \nu$ events is the *same* as that for usual (i.e., neutrino-less) events in Z_2 models with only a single massive invisible particle per decay chain, because the effective DM mass in former decay chains is also m_{DM}. We can therefore distinguish the $E_2 + \nu$ events from the E_3-type events in Z_3 models by observing the location of the upper edge: the latter events will have a smaller edge.

3.4 Applications: non-identical visible particles in the two decay chains

Next, we apply the theoretical observations on the M_{T2} technique for Z_2 and Z_3 models, which are described in the previous sections, for distinguishing Z_3 models from Z_2 ones in some *specific* cases. Like in the previous sections, we assume (for

in [68].

[8] As for the events with three (or more) DM, we assume here that there is a single (massive) invisible particle in each decay chain for the purpose of defining M_T.

[9] This feature of a long tail in $E_2 + \nu$-type events is valid even for the case of more than one visible particles in each decay chain.

simplicity) pair-produced (same) mother particles and that all visible particles are massless and use the naive M_{T2} analysis for all events. As mentioned earlier, in Z_3 models each mother particle can decay into either one or two dark matter particles along with visible/SM particle(s). Here,

- we consider a mother particle in a Z_3 model for which *both* these decay chains (with one and two DM, respectively) exist.

Similarly, in Z_2 models the mother particles can only decay into a single dark matter particle along with visible/SM particle(s). Here, we assume two such decay chains for a Z_2-mother which have the same visible final states as the above two Z_3-mother decay chains (respectively). The idea behind this choice is that such a Z_2 model could easily counterfeit a Z_3 model (at least based on the identity of the visible states). This motivates us to distinguish these two types of the DM stabilization symmetry using the M_{T2} variable.

For later convenience, we divide the discussion into two cases based on whether or not the visible state in the decay chain with one DM is identical to the one in the decay chain with two DM in the Z_3 model. We begin with the case where the SM final states in the two decay chains are not identical (this includes the case of partial overlap between these final states). Following the notation of previous section, let us denote $\mathrm{SM}_{1,\,2}$ to be these SM final state particles – whether they consist of one or more SM particles – in the two decay chains. And, for the Z_3 model, assume that SM_1 comes with one DM particle and SM_2 is associated with

two DM particles.[10] We thus have three *distinct* (based simply on identity of visible states) types of events in both the Z_3 and Z_2 models, denoted by SM_{11}, i.e., SM_1 on each side/from each mother and similarly $\mathrm{SM}_{12,\,22}$. Clearly, for Z_3 models, these three types of events correspond (respectively) to $E_{2,3,4}$-type events mentioned in the previous section and shown in Figure 3.2 (with $\mathrm{SM}_1 \neq \mathrm{SM}_2$). Hence, we can apply the formulae for the theoretical predictions of $M_{T2}^{\max}$ for E_2, E_3, and E_4 type events derived in the previous section to the $\mathrm{SM}_{11,\,12,\,22}$ events.

3.4.1 One visible/SM particle in each decay chain

As a further subcase, we assume that $\mathrm{SM}_{1,2}$ consist of only one particle. Clearly, the upper edges of the M_{T2} variable for SM_{11}, SM_{12}, and SM_{22} are given by Eqs. (3.8), (3.9), and (3.10), respectively. As is obviously seen from the left panel of Figure 3.3 or equivalently Eq. (3.11), the location of the upper edge for SM_{12} or SM_{22} is lower (for *all* trial DM mass $\tilde{m}$: cf. the case of more than one visible particles below) than that for SM_{11} (for the same mother and DM masses). In contrast, in Z_2 model we have the same expression for $M_{T2}^{\max}$ given by Eq. (3.5) for *all* of SM_{11}, SM_{12}, and SM_{22} because they all involve two DM particles in the final state. Thus,

- different edges for the $\mathrm{SM}_{11,\,12,\,22}$ events (in particular, larger for SM_{11}) can be evidence for Z_3 models, i.e., they provide discrimination between Z_2 and Z_3 models[11].

[10] Since a Z_2 model does not allow 2 DM particles in each decay chain, SM_1 and SM_2 are both emitted with only 1 DM in the final state in this model.

[11] unless multiple mother particles in the Z_2 models decay into the identical final state.

We can be further quantitative:

- for Z_3 models we can measure the masses of the mother and the DM particles separately as follows (in spite of the absence of a kink in the left panel of Figure 3.3).

Note that the theoretical formulae for $M_{T2}^{\max}$ in Eq. (3.8) through Eq. (3.10) – considered as a function of trial mass $\tilde{m}$ – have a structure of $\sqrt{C} + \sqrt{C + \tilde{m}^2}$ where C is a constant. So, the idea is to choose an arbitrary trial mass, then calculate the corresponding $M_{T2}^{\max}$ from the *experimental* data and thus determine the above-defined C. Also, in our specific case where visible particles are assumed massless, the *theoretical* formula for each C is written only in terms of the mother mass and the DM mass:

$$\frac{(M^2 - m_{DM}^2)^2}{4M^2} = \frac{\left((M_{T2,E_2}^{\max})^2 - \tilde{m}^2\right)^2}{4(M_{T2,E_2}^{\max})^2} \equiv C_{E2} \tag{3.20}$$

$$\frac{(M^2 - m_{DM}^2)(M^2 - 4m_{DM}^2)}{4M^2} = \frac{\left((M_{T2,E_3}^{\max})^2 - \tilde{m}^2\right)^2}{4(M_{T2,E_3}^{\max})^2} \equiv C_{E3} \tag{3.21}$$

Solving the above-given two equations, we obtain *both* mother and DM masses [12]:

$$M = \frac{2}{3\sqrt{C_{E2}}}(4C_{E2} - C_{E3}) \tag{3.22}$$

$$m_{DM} = \frac{2}{3\sqrt{C_{E2}}}\sqrt{(4C_{E2} - C_{E3})(C_{E2} - C_{E3})} \tag{3.23}$$

This situation is somewhat like the double edge signal for single mother decay discussed in Chapter 2, where it was again possible to obtain mother and DM masses from the two edges in invariant mass distribution of visible/SM final state.

[12] The upper edge from SM_{22} provides redundant information, but of course can be a cross-check.

On the other hand, for Z_2 models, we obtain only a *combination* of the mother and the DM masses from the (single) measurement of $M_{T2}^{\max}$, given by

$$\frac{(M^2 - m_{DM}^2)^2}{4M^2} = \frac{((M_{T2}^{\max})^2 - \tilde{m}^2)^2}{4(M_{T2}^{\max})^2} \equiv C, \tag{3.24}$$

and thus it is *not* possible to determine mother and DM masses separately.

3.4.2 More than one visible/SM particle in each decay chain

In this case, there is more interesting behavior of $M_{T2}^{\max}$ than in the case of one visible particle per chain [13]. The upper edges of M_{T2} for $\mathrm{SM}_{11,\,12,\,22}$ events are now obviously given by Eqs. (3.7), (3.16), (3.17) and (3.14), respectively. As discussed in Eq. (3.19), the upper edge for SM_{12} is the *same* as that for SM_{11} (cf. one visible particle case above) for $\tilde{m} > m_{DM}$, but is lower for $\tilde{m} < m_{DM}$ than that for SM_{11}. And, the upper edge for SM_{22} events always lower than SM_{11}. This fact enables us to *distinguish* Z_3 models from Z_2 ones because in Z_2 models the upper edges for $\mathrm{SM}_{11,\,12,\,22}$ coincide for *all* $\tilde{m}$ (just like the case with one visible particle in each decay chain).

Moreover, there occurs a kink in the upper edge of M_{T2} as a function of the trial DM mass as discussed in the previous sections. Due to the existence of this kink structure, SM_{11} itself is sufficient for the purpose of determining mother and

[13] In the SM_{12} events, the endpoints of the *visible* invariant mass distributions for the two sides of the event/decay chains will be different in Z_3 models, i.e., in E_3-type events (vs. being the same in Z_2 models), already providing a discrimination between the two types of models. However, developing another technique for distinguishing Z_3 from Z_2 models based on M_{T2} can still be useful.

DM masses (again, unlike one visible case): the trial mass which gives rise to a kink is the true DM mass and its corresponding $M_{T2}^{\max}$ is the true mother mass. (Of course this is how one can measure the masses of the mother and the DM particles separately even in Z_2 models.) Such a direct measurement of the mother and the DM masses leads us to

- a *prediction* (cf. one visible case) on the location of the upper edges for the *other* two types of events, namely SM_{12} and SM_{22}, a confirmation of which can provide evidence for Z_3 symmetry as underlying physics[14].

For SM_{12}, i.e., E_3-type events, actually, there are more interesting aspects of the kink structure in $M_{T2}^{\max}$ due to the dependence on the ratio of the DM and the mother masses: as discussed in section 3.3, the critical ratio is given by

$$\frac{m_{DM}}{M} = \frac{\sqrt{3}-1}{2}. \tag{3.25}$$

The kink is present only when the ratio of the DM and the mother masses is less than the above-given critical ratio. In this case, the kink location can be predicted by substituting mother and DM masses measured from the kink in SM_{11} into Eq. (3.18) so that it can provide a *further* verification for Z_3 symmetry[15].

Finally, note that another way to distinguish Z_3 from Z_2 models in this case was discussed in Chapter 2. The idea is to use SM_{12}, i.e., E_3-type, events in Z_3

[14]We can also predict (and then verify) location of kink in SM_{22} events. Alternatively, we can use kink in SM_{22}, i.e., E_4-type events to determine the mother and DM masses and then make predictions.

[15]Alternatively, this kink can be used to determine mother and DM masses, which are then used to predict edges/kinks in other events.

models, where edges in invariant mass distributions of *visible* particles on each side are different, i.e., $(M - m_{DM})$ and $(M - 2\, m_{DM})$ (vs. the two edges being the same for Z_2 models).

3.4.3 Signal fakes by an (effective) 2nd DM particle

In the two previous sections we have focused on decay processes with a single type of the DM particle in the final state (for both Z_3 and Z_2 models). The crucial observation for the sake of discriminating Z_3 from Z_2 models is that Z_3 models have more event-topologies (i.e., E_2, E_3, and E_4 type events with different upper edges in M_{T2} distributions) than the case of Z_2 (which has a single upper edge), regardless of the number of visible/SM particles in each decay chain. In turn, this contrasting feature is due to the different possibilities in *each* decay chain in Z_3 models, i.e., presence of one or two DM (unlike only one DM in Z_2 case).

However, Z_2 models can also acquire such different possibilities for decay chains (and thus fake Z_3 signals in the M_{T2} analysis) if we assume that there is a *second* DM (obviously Z_2-odd) particle (with larger mass) denoted by DM$'$ into which the Z_2-mother can decay, i.e., there are actually two (absolutely) stable DM particles in a Z_2 model [69–72]. Clearly, even with only one DM in a Z_2 model, a similar effect can arise from a mother decaying into an (Z_2-odd) *on*-shell color/electrically neutral particle which *decays* (into DM particle and SM, possibly visible), but outside the detector (i.e., there exists a Z_2-odd particle – other than the DM – which is stable and invisible as far as detector is concerned). Another related possibility is that

there is a Z_2-odd (on-shell) neutral particle which decays *in*side the detector, but invisibly, i.e., into DM and invisible SM, for example, neutrino. A classic example of the last type is found in supersymmetry where sneutrino decaying into neutrino and lightest neutralino (which is assumed to be the lightest supersymmetric particle, i.e., DM). Even in the latter two cases, there is "effectively" (i.e., as far as the collider analysis is concerned) a second "DM" and so we will denote it also by DM$'$. In particular, in the last case mentioned above, i.e., even if there is an (on-shell) neutral particle decaying invisibly inside the detector, the theoretical prediction of the M_{T2} variable is same as with a DM$'$ of same mass as this neutral mother particle.

Here, we note that the reference [17] has studied such (asymmetric) events using an M_{T2} type analysis, in particular, variants of the usual M_{T2} variable have been developed. As before, we will instead apply the naive/usual M_{T2} variable, i.e., assume (again, just for the purpose of constructing M_{T2}) that there is a single and same DM in both decay chains.

In more detail, the above case in Z_2 models give rise to "Z_3-faking" signals is as follows. As before, consider pair production of single mother such that decay chains with DM and DM$'$ are both allowed. Consequently, we obtain three distinct decay topologies for the full event: two DM, one DM and one DM$'$ and two DM$'$. We will denote these three types of events by E_2', E_3', and E_4' since they obviously resemble (and thus can fake) E_2, E_3, and E_4 type events being found in Z_3 models, respectively. In particular, we can expect three different upper edges for M_{T2} in E_2', E_3', and E_4'-type events[16]. Explicitly, the maximum balanced M_{T2} solutions for

[16] An extreme case is when DM$'$ is massless, for example, SM neutrino. However, in this case,

them (for both the cases with one visible particle per decay chain and more than one visible particle per decay chain) are simply given as follows:

$$\begin{aligned} M_{T2,E_2'}^{\max,bal} &= \sqrt{\frac{(M^2-m_{DM}^2)^2}{4M^2}} \\ &+ \sqrt{\frac{(M^2-m_{DM}^2)^2}{4M^2}+\tilde{m}^2} \qquad \text{for } E_2' \end{aligned} \tag{3.26}$$

$$\begin{aligned} M_{T2,E_3'}^{\max,bal} &= \sqrt{\frac{(M^2-m_{DM}^2)(M^2-m_{DM}'^2)}{4M^2}} \\ &+ \sqrt{\frac{(M^2-m_{DM}^2)(M^2-m_{DM}'^2)}{4M^2}+\tilde{m}^2} \qquad \text{for } E_3' \end{aligned} \tag{3.27}$$

$$\begin{aligned} M_{T2,E_4'}^{\max,bal} &= \sqrt{\frac{(M^2-m_{DM}'^2)^2}{4M^2}} \\ &+ \sqrt{\frac{(M^2-m_{DM}'^2)^2}{4M^2}+\tilde{m}^2} \qquad \text{for } E_4', \end{aligned} \tag{3.28}$$

and the maximum unbalanced M_{T2} solutions (only for the case with more than one visible particle per decay chain) are given as follows:

$$M_{T2,E_2'}^{\max,unbal} = M - m_{DM} + \tilde{m} \qquad \text{for } E_2' \tag{3.29}$$

$$M_{T2,E_3'}^{\max,unbal} = M - m_{DM} + \tilde{m} \qquad \text{for } E_3' \tag{3.30}$$

$$M_{T2,E_4'}^{\max,unbal} = M - m_{DM}' + \tilde{m} \qquad \text{for } E_{4'}. \tag{3.31}$$

Here $m_{DM}'(> m_{DM})$ denotes the mass of the second DM-like particle. Again, all three types actually contains *two* DM/DM-like particles, i.e., the subscripts on E' do not imply the number of DM particles in a full decay chain but rather indicate the respective topologies in Z_3 models which they fake. Note that if we set $m_{DM}' = 2m_{DM}$, then the above edges are exctly the ones in a Z_3 model (see Eqs. (3.8)

as mentioned in section 3.3.3, the upper edges for E_3' (denoted by $E_2 + \nu$ event in section 3.3.3) and E_4'-type events will be *same* as for E_2'-type events. Thus this case can be easily distinguished from Z_3 models.

through (3.10) and Eqs. (3.12), (3.13), and (3.15) from previous sections. This feature is as expected since for $E_{3,\,4}$-type events (in Z_3 models) which are at the edge of the respective M_{T2} distributions, the two DM from *same* mother are collinear so that their invariant mass is $2m_{DM}$, i.e., the decay chain with two DM effectively has *single* DM of this mass as far as M_{T2}-edge is concerned.

Despite the fact that such Z_2 events with second DM-like particle can introduce three decay topologies, we can still differentiate Z_3 and Z_2 models. However, the strategies to be applied depend on the number/identity of visible particles in each decay chain. In this section, we consider the case where the visible particles in decay chain with DM (denote by SM_1, following the notation used earlier) is different than the visible particles (denoted by SM_2) that in decay chain with DM$'$ in Z_2 model or two DM (in Z_3 model). Thus, the three types of events SM_{11}, SM_{12} and SM_{22}, i.e., distinguishable from the identity of SM visible particles, have different edges since they correspond to the E_2', E_3', and E_4'-type events in a Z_2 model or (as mentioned in previous section) E_2, E_3, and E_4-type events in a Z_3 model. This case can be further sub-divided into one and more than one visible particles in each decay chain.

In the case with one visible particle per decay chain, one may distinguish Z_2 and Z_3 models by examining the *shape* of the above three M_{T2} distributions. The idea is that, as explicitly mentioned above, E_2', E_3', and E_4' all have only *two* DM/DM-like particles, i.e., two DM, one DM and one DM$'$, and two DM$'$, and therefore, they have a similar shape of the M_{T2} distribution as the E_2-type event. The implication of this observation is E_2', E_3', and E_4' all give a sharp upper edge in the M_{T2} distribution. On the other hand, in the decay chain with two DM in

$E_{3,\,4}$-type events of Z_3 models, in general (i.e., away from edge of M_{T2}), the two DM are not collinear so that their invariant mass of two DM is not $2m_{DM}$, in fact, this invariant mass is not even fixed. Thus, even if the above three M_{T2}-*edges* for Z_3 models are identical to those for Z_2 models with two different DM (with the second one being twice as heavy as first one), the shapes are not expected to be similar. In fact, E_3 and E_4 type events in Z_3 models give a (relatively) longer tail as already discussed in section 3.3.3. Hence, if one of the M_{T2} distributions for $\mathrm{SM}_{11,\,12,\,22}$ events – again, corresponding to the three different topologies – has a sharp upper edge and two of which have a longer tail, then it is likely that such events originate from Z_3 models.

On the other hand, once there exists more than one visible particle in each decay chain, the shape is no longer a useful discriminator. The reason is that, in general, clear sharp edges in the M_{T2} distributions are not expected here (unlike the cases with one visible particle per decay chain), i.e., the number of events/statistics at the M_{T2}-upper edge is small in this case: in turn, this feature is due to more constraints which need be satisfied (see section 3.3). Instead, we can take the advantage of "kink" in the plot of $M_{T2}^{\max}$ versus the trial DM mass, which allows us to determine the masses of mother and DM particles separately. Using the SM_{11} events, one can evaluate M and m_{DM} as mentioned in the previous section, *assuming* that it is a Z_3 model. Then we predict the locations of upper edge and the locations of kink for the $\mathrm{SM}_{12,\,22}$ events. If the underlying physics is a Z_2 model (with two different DM particles) instead, then these predictions do not match with the experimental results from the associated M_{T2} analysis. This is because, in general, the mass of

the second DM-like particle, m'_{DM} is not equal to twice of the DM mass, $2m_{DM}$. In other words, the cross-checking of mother and DM masses between SM_{11} and $\mathrm{SM}_{12,\,22}$ events enables us to separate Z_3 models from Z_2.

3.5 Applications: identical visible particle(s) in the two decay chains

Next, we consider the case of the visible particle(s) in the two decay chains with one and two DM (for Z_3 models) being the same. In this case, in the Z_3 models, we can not separate $E_{2,3,4}$ type events using simply the identities of the visible particles, i.e., $\mathrm{SM}_1 = \mathrm{SM}_2$ in Figure 3.2 (unlike in the previous section). Obviously, we add the three (i.e., E_2, E_3, and E_4-type) distributions of M_{T2}, whose behaviors were discussed above (for non-identical case), to obtain the observable M_{T2} distribution in Z_3 models. Of course, for Z_2 models (which could potentially fake the Z_3 models), there are then only E_2-type and possibly $E_2 + \nu$ events that we discussed earlier.

If we have only one visible particle in each decay chain, the M_{T2} distribution for the E_3 type events *always* (i.e., for all $\tilde{m}$, cf. more than one visible case discussed below) has a lower $M_{T2}^{\max}$ than for the E_2 type events (see the left panel of Figure 3.3), so that in principle their addition/combination would give rise to a "kink" in the M_{T2} distribution[17] (again for Z_3 model, but not for Z_2 model).[18] It turns out,

[17] Such a kink in the M_{T2} *distribution* is not to be confused with that in the plot of $M_{T2}^{\max}$ as a function of $\tilde{m}$.

[18] Adding events of E_4 type, i.e., two DMs in each decay chain, will introduce another, but even less visible, kink.

however, that the visibility of this kink is not clear because the M_{T2} distribution for E_3 type events has a longer tail (that for E_2-type events) as discussed in section 3.3 (see the right panel of Figure 3.5). It also turns out that the kink will get further smeared out once uncertainties in measurements are taken into account. In other words, this kink is not evidence for Z_3 models since it could be faked by statistical fluctuations in the distribution or experimental errors.

On the other hand, if there exists more than one visible particle in each decay chain, the M_{T2} distribution for Z_3 model shows somewhat different behavior. As discussed in detail in section 3.4.2, for trial DM mass above the true DM mass, the upper edge of M_{T2} distribution for E_2 and E_3 type events are the same. However, the upper edge of M_{T2} distribution for E_3 type events is *increasingly* lower than that for E_2 type for trial DM mass below the true DM mass[19]. We therefore expect a "moving" kink (as we vary $\tilde{m}$) in the M_{T2} distribution – such a kink starts to appear for trial mass below the true DM mass (i.e., no kink would appear in the total M_{T2} distribution for larger trial masses) and the gap between the kink position (i.e., corresponding to the E_3 edge) and the overall upper (i.e., E_2) edge is increasing as the trial mass becomes smaller[20]. This "moving" feature of the kink in the total M_{T2} distribution can be a further (i.e., beyond simply *existence* of kink) evidence for the existence of E_3 type events and thus a proof of Z_3 models. However, even

[19]To be more precise, the gap between the two edges *relative* to mother/DM masses increases.

[20]In the one visible particle case, the gap between the edges in $E_{2,\,3}$-type events, again relative to mother/DM masses, is roughly constant with trial mass so that kink in M_{T2} distribution does not move.

though the kink is "moving", it is still hard to identify it in the M_{T2} distribution, and thus we do not rely on these kinks as a way to distinguish between Z_2 and Z_3 models.

These observations motivate us to introduce new methods to separate E_3 type events from E_2 type events.[21] In the following (two) subsections, we develop such a method, and then we apply them to the two specific cases (i.e., one visible particle and more than one visible particles in each decay chain), and see how to use them to distinguish between Z_2 and Z_3 models.

3.5.1 Separating E_2 and E_3 type events using P_t/H_t ratio

To separate E_2 and E_3 types of events, we can utilize the fact that E_2 type events have one DM per decay chain, and E_3 type events have one DM in one decay chain and two DMs in the other decay chain. In other words, for E_3 type events, the visible particle(s) in the decay chain having two DMs in the final state carry less momentum/energy (than in the other decay chain). Thus the ratio between the momentum/energy of visible particle(s) on the two decay chains are expected to be (relatively) sizeable on average (compared to E_2 type events). In order to find out how this intuition plays out in real situations, we begin with the case where there

[21] Once we separate these two types, we can repeat the program described in detail in section 3.4, i.e., either determine the masses of the mother and the DM particles from the the upper edges of M_{T2} in these two types of events for the case of one visible particle in each decay chain or *predict* the upper edge for E_3-type events (using measurements in E_2-type events) for the more than one visible particle case.

exists only a single visible particle per decay chain, and then move on to the case where there exist more than one visible particles per decay chain.

3.5.1.1 One visible/SM particle in each decay chain

For the case with one visible particle per decay chain, we consider the P_t ratio of the two visible particles as follows:

$$R_{P_t} = \frac{P_t^{\max}}{P_t^{\min}}, \tag{3.32}$$

where $P_t^{\max}$ is the larger P_t of the two visibles coming from two separate decay chains, and $P_t^{\min}$ is the smaller one. From our physical intuition mentioned above, we expect the R_{P_t} for E_3 type events to be larger (on average) than that for E_2 type events[22]. To verify this expectation, we did a simulation using `MadGraph/MadEvent` for a (toy) model with mother mass $M = 400$ GeV and DM mass $m_{DM} = 150$ GeV. The R_{P_t} distributions for E_2 and E_3 type events are shown in Figure 3.6. We can see clearly that R_{P_t} for E_3 type events is generally larger than that for E_2 type events. For comparison, we also included the R_{P_t} distribution for $E_2 + \nu$ events (i.e., two DM particles and an extra invisible, but massless, particle in the full event) in Figure 3.6. One can easily see that the $E_2 + \nu$ events have on *average* larger R_{P_t} than that for pure E_2 type events, but smaller R_{P_t} than that for E_3 type events. This observation agrees with our expectation: in the $E_2 + \nu$ events, we have only one extra *massless* invisible particle (relative to E_2-type events), while in E_3 type events, we have one extra *massive* invisible particle so that the disparity between

[22] We neglect E_4-type events and comment on this issue later.

the visible particle momenta on the two sides in the former case should be relatively smaller.

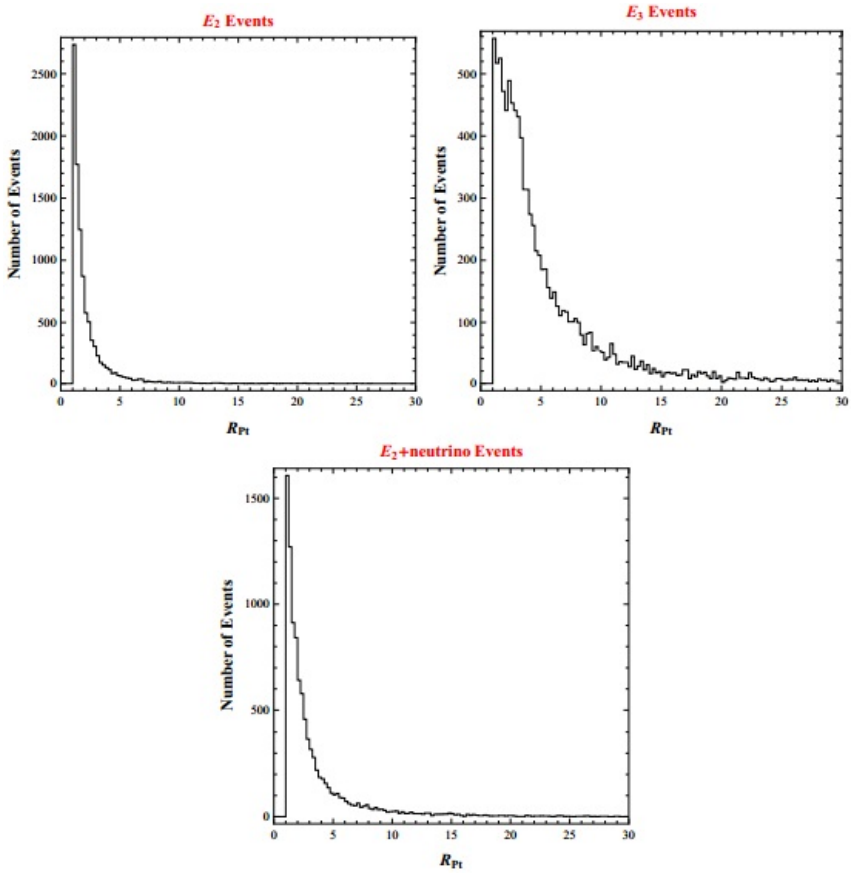

Figure 3.6: R_{P_t} distributions for E_2 type events (upper-left panel), E_3 type events (upper-right panel) and $E_2 + \nu$ events (lower panel) for the case with one visible particle on each decay chain. The mother mass is $M = 400$ GeV, the DM mass is $m_{DM} = 150$ GeV.

Due to different R_{P_t} distributions of E_2 and E_3 type events, we can try to distinguish them by doing a cut $R_{P_t} > R_{P_t}^{\min}$. The percentage of "surviving" events in E_2 and E_3 type events according to different choice of $R_{P_t}^{\min}$ are shown in Table 3.1. For comparison, we also include $E_2 + \nu$ events in Table 3.1. We can see that the survival rates for E_2 type events are fairly independent of the mother and the DM

Table 3.1: The percentage of surviving events in E_2, E_3 and $E_2 + \nu$ events for different choice of $R_{P_t}^{\min}$ for the case with one visible particle per decay chain. The mother mass is $M = 400$ GeV and the DM mass is $m_{DM} = 150$ GeV.

$R_{P_t}^{\min}$	2	3	4	5	6	7	8	9
E_2	0.3375	0.1629	0.0957	0.0612	0.0413	0.0285	0.0225	0.0178
E_3	0.7929	0.6105	0.4649	0.3696	0.303	0.2525	0.21	0.1774
E_2+ν	0.5366	0.3323	0.2319	0.1733	0.1342	0.1101	0.0887	0.0738

masses, since in this type of events the energies of the visible particles in two decay chains are always comparable. Therefore,

- if the survival rates for the events (after the R_{P_t} cut) are much larger than that of E_2 values shown in Table 3.1, then we can conclude that the events are *not* purely E_2 type, i.e., it is an evidence for existence of another/third invisible particle (whether massless or massive).

In general, the survival rates for E_3 type events are much larger than those of E_2 type events, but the survival rates of E_3 type events depend on the mother and DM masses. In addition, the survival rates for $E_2 + \nu$ events are larger than that of E_2 type events as well (even though they are generally smaller than that of E_3 type events). In this sense, an observation of large survival rates might not (by itself) provide a strong support that there exist E_3 type events in the sample.

To get further confirmation of E_3-type events (and thus to distinguish Z_2 and Z_3 models), we can employ the R_{P_t} cut as above and then study the M_{T2} distribution of the *surviving* events. The key idea is to compare the upper edges of the M_{T2} distributions before and after the R_{P_t} cut. If the underlying physics model is Z_2 type, then clearly we can only obtain E_2 type events (or $E_2 + \nu$) events before and

after the cut, and the upper edge of its M_{T2} distribution is not altered. However, if the underlying physics model is Z_3, then (before the cut) the total events are an *admixture* of E_2 and E_3 type. Since the upper edge of E_3 (and E_4)-type events is smaller than those of E_2-type events, the upper edge of M_{T2} distribution (again before the R_{P_t} cut) should be that of E_2 type events. On the other hand, *after* the cut the upper edge of M_{T2} distribution should be lower than before since the surviving events are mostly of E_3 type.

To illustrate this technique, we apply the analysis outlined above to the previously simulated events using a model with $M = 400$ GeV, $m_{DM} = 150$ GeV, and we pick the trial mass to be $\tilde{m} = 25$ GeV. Based on the survival rates shown in Table 3.1, we choose $R_{P_t}^{\min} = 5$. Before we do the analysis, we need to investigate whether the $R_{P_t} > 5$ cut is "biased", i.e., does the cut tend to remove more events with a high M_{T2} value?[23] For this we consult Figure 3.7, which shows *separately* the M_{T2} distributions for both pure E_2 and E_3 type events before and after the R_{P_t} cut. By comparing the left panels and right panels in Figure 3.7 we can easily see that the upper edges for both E_2 and E_3 type events do not get modified after the R_{P_t} cut, which suggests that the R_{P_t} cut is not "biased" [24]. In addition, we see that these upper edges in simulated events approximately agree with the theoretical predictions (shown by vertical lines)[25].

[23] If the answer is affirmative, then $M_{T2}^{\max}$ after the cut will be reduced even for *purely* E_2-type events.

[24] But a choice of larger $R_{P_t}^{\min}$ would introduce bias in the cut.

[25] But note that in experiments these predictions are *a priori* unknown since we do not know the masses of the mother and DM separately.

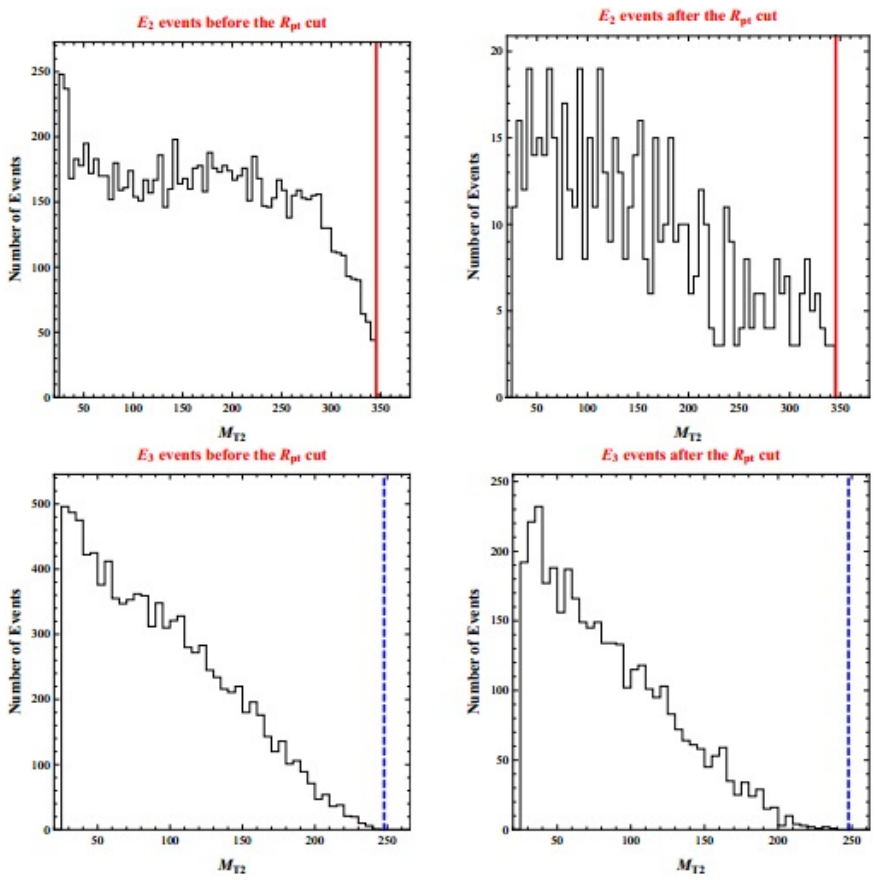

Figure 3.7: M_{T2} distribution for E_2 (top two panels) and E_3 type events (lower two panels) for simulated events using a model with $M = 400$ GeV and $m_{DM} = 150$ GeV and one visible particle per decay chain. The trial mass is chosen to be $\tilde{m} = 25$ GeV. The left panels are the M_{T2} distributions before the R_{P_t} cut, and the right panels are the M_{T2} distributions after the R_{P_t} cut. The solid red (dashed blue) lines are the theoretical prediction for the upper edges of M_{T2} distribution for E_2 and E_3 type events, respectively.

Now we can demonstrate how to distinguish Z_2 and Z_3 models using a *combination* of R_{P_t} cut and M_{T2} distributions. First we consider a Z_3 model, where we assume that the branching ratio for the mother to decay into one DM (and visible particle) and into two DMs (and visible particle) are both 50%.[26] Since we assumed

[26]In general, the decay into two DM should be phase-space suppressed relative to the decay into

that the visible particles in these two decays are identical, we have to combine the M_{T2} distributions for E_2 and E_3 type events in a 1 : 2 ratio to get the *total* M_{T2} distribution. The result is shown in the left panel of Figure 3.8. As expected, we can see from this figure that the combined E_2 and E_3 type events have an upper edge in M_{T2} distribution that agrees with the theoretical expectation for E_2 type events (the red solid line). As discussed earlier, we can also see that the total M_{T2} distribution has a kink near the theoretical $M_{T2}^{\max}$ for E_3 type events, but it is hard to identify such a kink because of statistical fluctuations. The right panel of Figure 3.8 shows the M_{T2} distribution for the combined events *after* the R_{P_t} cut. It can be seen clearly that the upper edge of M_{T2} distribution gets reduced. In fact, the new edge agrees with the theoretical expectation of the $M_{T2}^{\max}$ of E_3 type events (the blue solid line). This confirms our expectation that the R_{P_t} cut discards most E_2 type events while retaining a sizeable fraction of E_3 type events, i.e., the events which pass the R_{P_t} cut are mostly E_3 type.

Of course, we do not know *a priori* where the $M_{T2}^{\max}$ for E_3 type events (solid blue line) lies due to the lack of knowledge of the mother and DM masses. Rather the idea is that we can simply *measure* the upper edge in M_{T2} distributions after the R_{P_t} cut (again, this approximately correspond to that of E_3-type events). Combining this edge with that before the cut (i.e., corresponding to E_2-type event) then allows us to evaluate the masses of the mother and the DM particles as described in detail

one DM. However, in some specific models, this suppression (for the decay chain with two DM) could be compensated by larger effective couplings in that chain so that the two decay processes can have comparable branching ratio as assumed here.

in section 3.4.1[27]. A complication arises (as follows) in obtaining the $M_{T2}^{\max}$ for events after the R_{P_t} cut. As can be seen in the right panel of Figure 3.8, there are still some events beyond the theoretical value of $M_{T2}^{\max}$ for E_3 type events (the blue solid line in the plot), for example from (a small number of) E_2-type events which passed the cut. So we need an algorithm to get rid of those "background" events and do a fit to the M_{T2} distribution in order to find $M_{T2}^{\max}$. The details of the method we employed are discussed in Chapter D. We apply the above techniques to the simulated events. The values of the mother and the DM masses we obtained from this analysis are 394 ± 8 GeV and 142 ± 13 GeV, which agree quite well with the theoretical values (400 GeV and 150 GeV). However, we expect that uncertainty in energy measurements would introduce additional errors so that a more thorough analysis taking into account these effects (which is beyond the scope of this thesis) is needed in order to be more realistic.

For comparison, we consider now Z_2 models. In these models, we have either E_2 or $E_2 + \nu$ events. For pure E_2 type events, we have already shown in the upper panels of Figure 3.7 that the upper edge of M_{T2} distribution is not reduced after the R_{P_t} cut (note that this would not be true if the R_{P_t} cut is "biased"). For completeness, we also consider Z_2 models where the mother can decay into one DM or one DM plus neutrino, with the visible particle in the two decay chains being identical. We again assume that both branching ratios are 50%. Thus, we will obtain a *combination* of $E2$ and $E_2 + \nu$-type events. The M_{T2} distributions in this case are shown in Figure 3.9. The left panel shows that before the R_{P_t} cut, the upper

[27]Note that this cannot be done in Z_2 models as discussed in section 3.4.1.

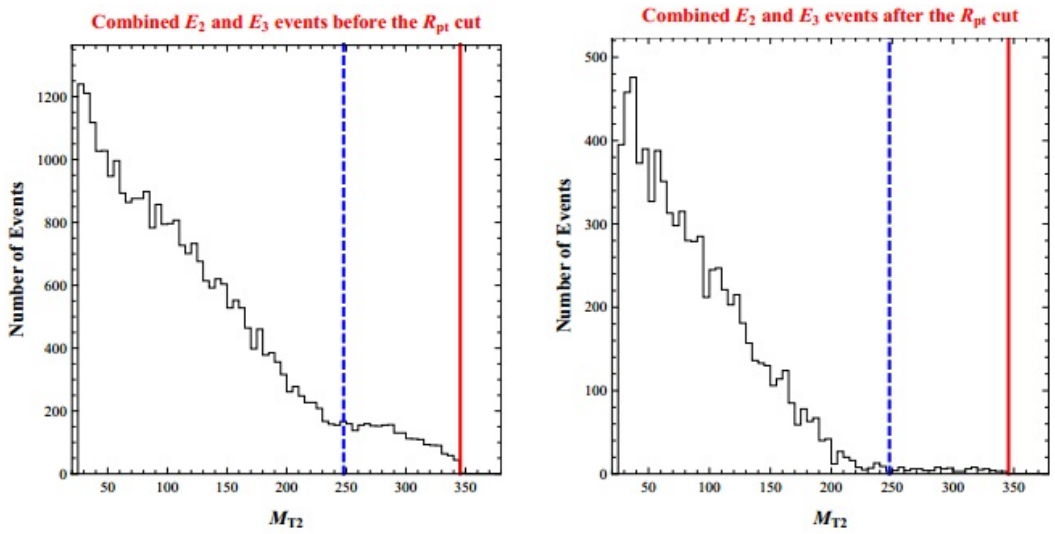

Figure 3.8: M_{T2} distribution for combined E_2 and E_3 type events ($1:2$ ratio) before (left panel) and after (right panel) the $R_{P_t} > 5$ cut for the case with one visible particle per decay chain. The mother mass is $M = 400$ GeV and the DM mass $m_{DM} = 150$ GeV. The trial mass is chosen to be $\tilde{m} = 25$ GeV. The solid red (dashed blue) lines represent the theoretical predictions for the upper edges of M_{T2} distributions for E_2 and E_3-type events, respectively.

edge of M_{T2} distribution agrees with the theoretical prediction of E_2 type events and does not have a kink. And, by comparing with the right panels of this figure (i.e., after the R_{P_t} cut, when mostly $E_2 + \nu$-type events survive) we can see that the location of the upper edge for M_{T2} distribution also does not change. These two observations are easily explained by the fact that, as discussed earlier, the $M_{T2}^{\max}$ for $E_2 + \nu$-type events is *same* as for (purely) E_2-type events. Based on the above discussions for Z_2 and Z_3 models, we conclude that

- by observing whether the upper edge of M_{T2} distribution changes (in particular, reduces) *after the* R_{P_t} *cut*, we can distinguish between Z_2 (including those with neutrino appearing in decay of a mother) and Z_3 models.

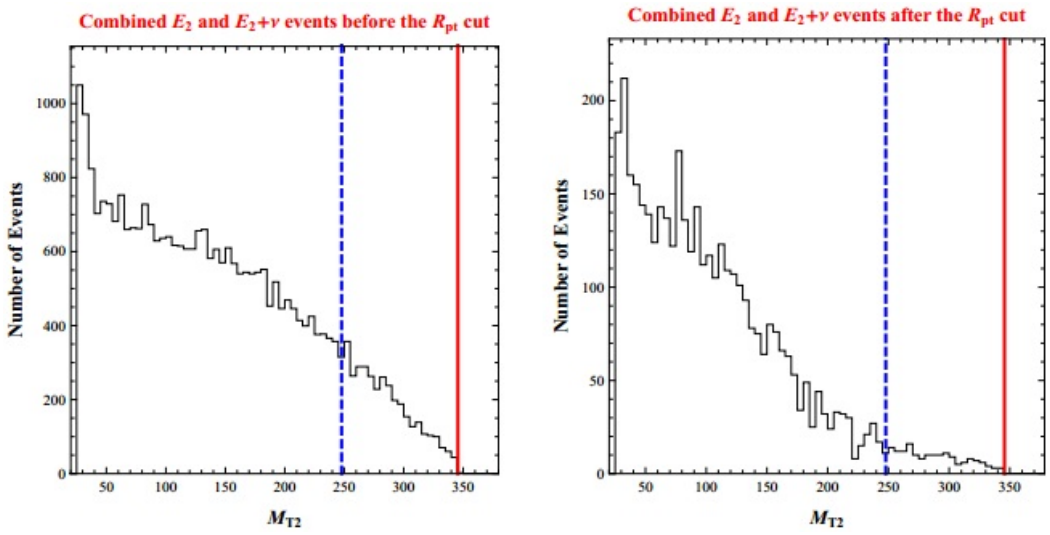

Figure 3.9: M_{T2} distribution for combined E_2 and $E_2 + \nu$ events (1 : 2 ratio) before (left panel) and after (right panel) the $R_{P_t} > 5$ cut for the case with one visible particle per decay chain. The mother mass is $M = 400$ GeV and the DM mass $m_{DM} = 150$ GeV. The trial mass is chosen to be $\tilde{m} = 25$ GeV. The solid red (dashed blue) lines represent the theoretical predictions for the upper edges of M_{T2} distributions for E_2 and E_3-type events, respectively.

3.5.1.2 More than one visible/SM particles in each decay chain

Next let us consider the case with more than one visible/SM particles per decay chain[28] To be specific, we consider the case with two visible particles per decay chain. A similar analysis can be done if there are more than two visible particles. To separate E_2 and E_3 type events, we consider the ratio of H_t, where $H_t^i = \sum_a |P_t^{v_a^i}|$ is the scalar sum of P_t's of visible particles in the same decay chain

[28]Note that in this case, we will get a double-edge in the visible invariant mass distribution from a *single* mother decay, which can already be used to distinguish Z_3 from Z_2 models in Chapter 2. However, it is always useful to have more techniques – such as the one, using decays of *both* mothers in the event, that we are developing here – for such discrimination.

(assuming we know which particles come from which decay chain), and $i = 1,\ 2$ is the index for the decay chains. H_t gives a measure of how energetic the visible particles are in each decay chain. We define the H_t ratio as follows

$$R_{H_t} = \frac{H_t^{\max}}{H_t^{\min}}, \tag{3.33}$$

where $H_t^{\max} = \max(H_t^1, H_t^2)$ and $H_t^{min} = \min(H_t^1, H_t^2)$. From similar reasons to the one visible particle case discussed above, we expect R_{H_t} for E_3 type events to be larger than that for E_2 type events on average. To illustrate this feature, we simulate E_2, E_3 and $E_2 + \nu$ events for a model with $M = 400$ GeV and $m_{DM} = 150$ GeV using `MadGraph/MadEvent`. The results for the R_{H_t} distribution for different types of events are shown in Figure 3.10. It can be seen that these distributions are very similar to the R_{P_t} distributions for the one visible particle case shown in Figure 3.6. The R_{H_t} for E_3 type events is on average larger than that of $E_2 + \nu$ events, which in turn is on average larger than that for E_2 type events. The survival rates for E_2, E_3 and $E_2 + \nu$ events for the cut $R_{H_t} > R_{H_t}^{\min}$ with different choices of $R_{H_t}^{\min}$ are shown in Table 3.2. As in the one visible case discussed before, if the survival rates for the observed events are much larger than the E_2 value shown in Table 3.2, then we can conclude that the events cannot be purely of the E_2 type. But large survival rates alone cannot be used as a convincing evidence for Z_3 models.

Just like in the case with one visible particle per decay chain, we again use a combined analysis of R_{H_t} cut and upper edges of M_{T2} distributions to distinguish between Z_2 and Z_3 models. However, there is one major difference between the case with two visible particles per decay chain and the case with one visible particle

Table 3.2: The percentage of survival events in E_2, E_3 type events and $E_2+\nu$ events for different choice of $R^{\rm min}_{H_t}$ for the case with two visible particles per decay chain. The mother mass is $M = 400$ GeV and the DM mass is $m_{DM} = 150$ GeV.

$R^{\rm min}_{H_t}$	2	3	4	5	6	7	8	9
E_2	0.1542	0.0401	0.0142	0.0065	0.0028	0.0015	0.0009	0.0006
E_3	0.7990	0.5181	0.3103	0.1905	0.1228	0.0838	0.0583	0.0422
$E_2+\nu$	0.3086	0.1192	0.0551	0.0279	0.0166	0.0104	0.0074	0.0052

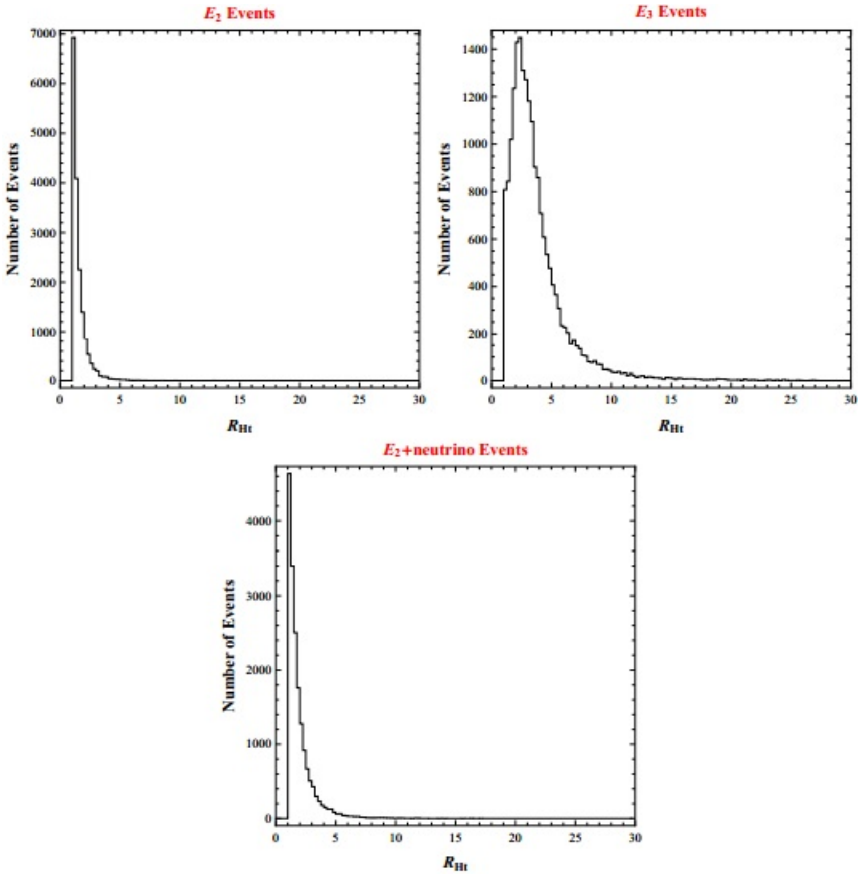

Figure 3.10: R_{H_t} distributions for E_2 type events (upper-left panel), E_3 type events (upper-right panel) and $E_2 + \nu$ events (lower panel) for the case with two visible particles on each decay chain. The mother mass is 400 GeV, the DM mass is 150 GeV.

per decay chain. In the latter case, we cannot find the mother and DM mass just based on the M_{T2} upper edges for events before R_{P_t} cut. On the other hand, in the

case at hand, there is a kink structure in the $M_{T2}^{\max}$ vs $\tilde{m}$ plot for E_2-type events events which tells us both the mother and the DM masses (see section 3.2). And, as mentioned for the one visible particle case, $M_{T2}^{\max}$ for E_3 type events is always smaller than that of E_2 type events, so that, before the R_{H_t} cut, $M_{T2}^{\max}$ for the *combined* events is given by that of E_2-type events. Therefore, in the present scenario, we can find out the mother and DM masses before we do any R_{H_t} cut. We can then *predict* the edge in M_{T2} for E_3-type events, i.e., after the R_{H_t} cut (again, the events surviving the cut will be mostly E_3-type).

We now demonstrate an application of the general strategy outlined above. Based on the survival rates shown in Table 3.2, we choose $R_{H_t}^{\min} = 3$ in this case. Figure 3.11 shows the M_{T2} distributions for the simulated pure E_2 and E_3 type events before and after the R_{H_t} cut. The trial DM mass is chosen to be 9 GeV. By comparing the left and the right panels in Figure 3.11, we can see that R_{H_t} cut does not alter the upper edge of M_{T2} distribution for both E_2 and E_3 type events. Therefore the R_{H_t} cut is not "biased" [29]. We then consider a Z_3 model where the branching ratios of the mother particle decaying into two DM particles (plus two visible particles) and into one DM particle (plus two visible particles) are both 50%. We show the M_{T2} distributions for the combined events before (left panel) and after (right panel) the $R_{H_t} > 3$ cut in Figure 3.12. As expected, we see that before the R_{H_t} cut, the upper edge of M_{T2} distribution agrees with the theoretical prediction of E_2 type events (shown by the red line). And, the upper edge for the M_{T2} distribution gets reduced after the R_{H_t} cut, which can serve as an evidence

[29] However, a choice of higher $R_{H_t}^{\min}$ will give rise to bias.

for Z_3 model (cf. discussion of Z_2 model below). In addition, as mentioned earlier, knowing the mother and DM masses from the kink in the plot of $M_{T2}^{\max}$ before the cut as a function of trial DM mass , we can predict (shown by the blue line) the upper edge for the M_{T2} distribution for the events that passed the R_{H_t} cut (it is just the theoretical $M_{T2}^{\max}$ for E_3 type events). From the right panel of Figure 3.12 we see that

- the observed $M_{T2}^{\max}$ for events that passed the R_{H_t} cut does agree with the *prediction* (cf. one visible particle case above), thus providing additional evidence that the underlying physics model is Z_3.

We can compare the above result with Z_2 models. If we just have pure E_2 type events, then the R_{H_t} cut does not change the upper edge of M_{T2} distribution, as already seen in the upper panels of Figure 3.11. As in the one visible particle case, we can also consider the case where there are $E_2 + \nu$ events in addition to E_2 events: we assume that the branching ratios for mother to decay into one DM plus neutrino (plus two visible particles) and into one DM (plus two visible particles) are both 50%. We show the M_{T2} distribution before (left panel) and after (right panel) the R_{H_t} cut for this case in Figure 3.13, from which we can see that the upper edge of M_{T2} distribution before the cut agrees with the theoretical prediction for E_2-type events and that it again does not change after the cut (as expected: see the similar discussion for the one visible particle case).

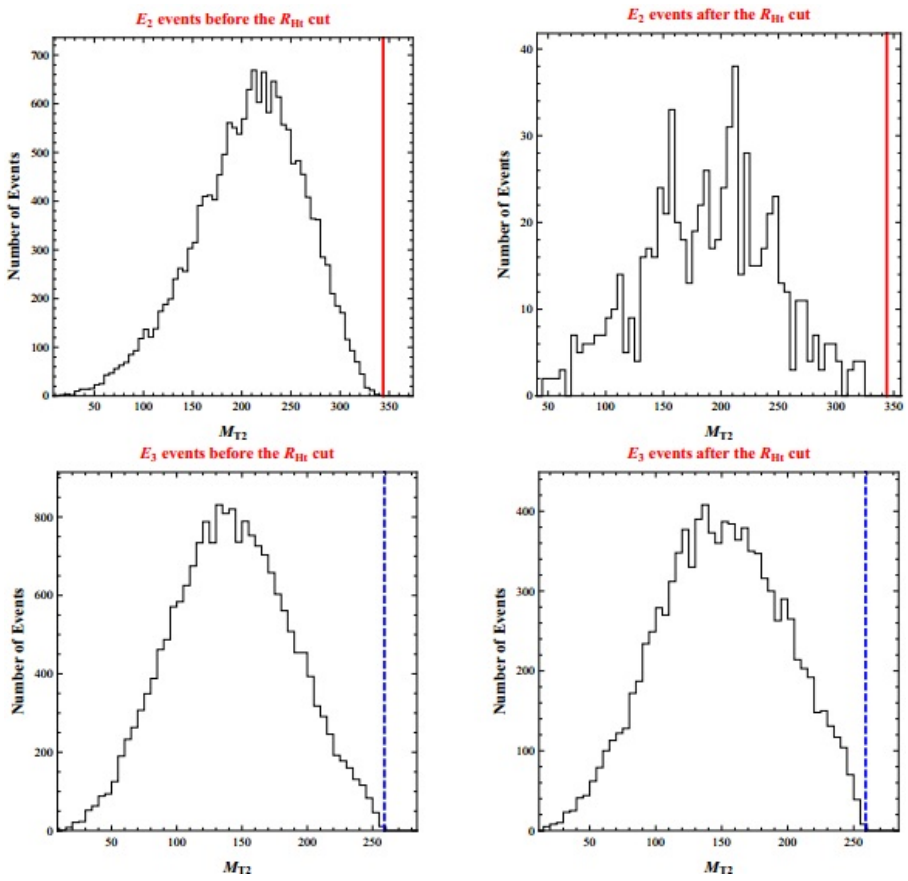

Figure 3.11: M_{T2} distribution for E_2 (top two panels) and E_3 type events (lower two panels) for simulated events using a model with $M = 400$ GeV and $m_{DM} = 150$ GeV and two visible particles per decay chain. The trial mass is chosen to be $\tilde{m} = 9$ GeV. The left panels are the M_{T2} distributions before the $R_{H_t} > 3$ cut, and the right panels are the M_{T2} distributions after the $R_{H_t} > 3$ cut. The solid red (dashed blue) lines are the theoretical predictions for the upper edges of M_{T2} distribution for E_2 and E_3 type events.

3.5.2 A summary of the analysis and its limitations

Now we summarize the analysis needed to be carried out to distinguish between Z_2 and Z_3 models when the visible particles on each decay chain are identical.

For the case with one visible particle per decay chain:

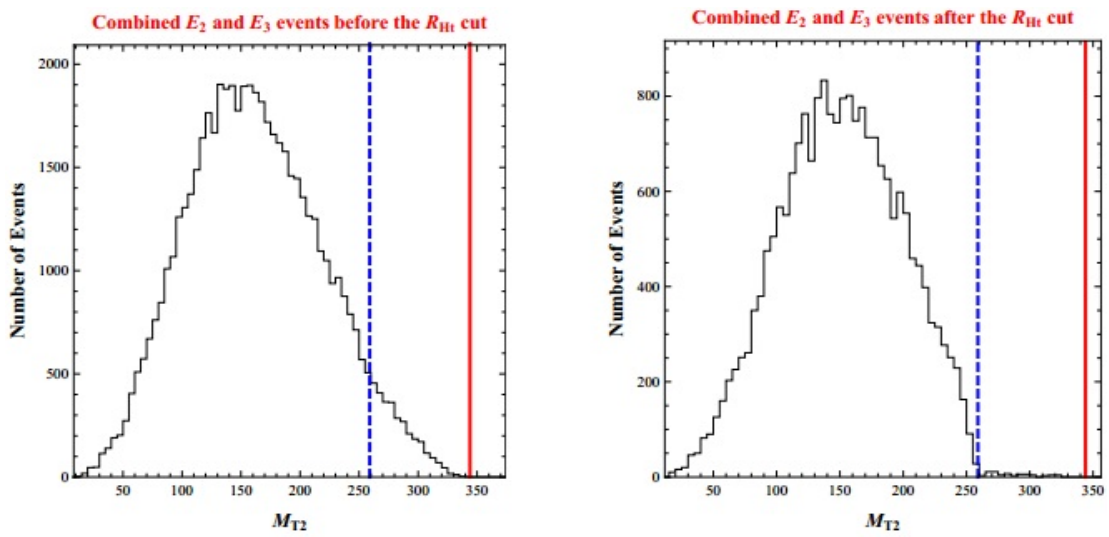

Figure 3.12: M_{T2} distribution for combined E_2 and E_3 type events ($1:2$ ratio) before (left panel) and after (right panel) the $R_{H_t} > 3$ cut for the case with two visible particles per decay chain. The mother mass is $M = 400$ GeV and the DM mass $m_{DM} = 150$ GeV. The trial mass is chosen to be $\tilde{m} = 9$ GeV. The solid red (dashed blue) lines represent the theoretical predictions for the upper edges of M_{T2} distributions for E_2 and E_3-type events, respectively.

- We first find $M_{T2}^{\max}$ with different trial DM masses ($\tilde{m}$) for *all* the events. We can then substitute this value into $\sqrt{C_{E_2}} + \sqrt{C_{E_2} + \tilde{m}^2} = M_{T2}^{\max}$ to find the parameter C_{E_2} (see the details in section 3.4.1).

- We apply the cut $R_{P_t} > 5$ and find $M_{T2}^{\max}$ with different trial masses ($\tilde{m}$) for the events that passed the cut. If we observe that the $M_{T2}^{\max}$ is reduced *after* the R_{P_t} cut (as compared to before), then we can conclude that the underlying physics model is Z_3 type, otherwise it is Z_2 type. On the other hand, if the $M_{T2}^{\max}$ is not changed after the R_{P_t} cut, then we conclude that the underlying physics model is Z_2 type.

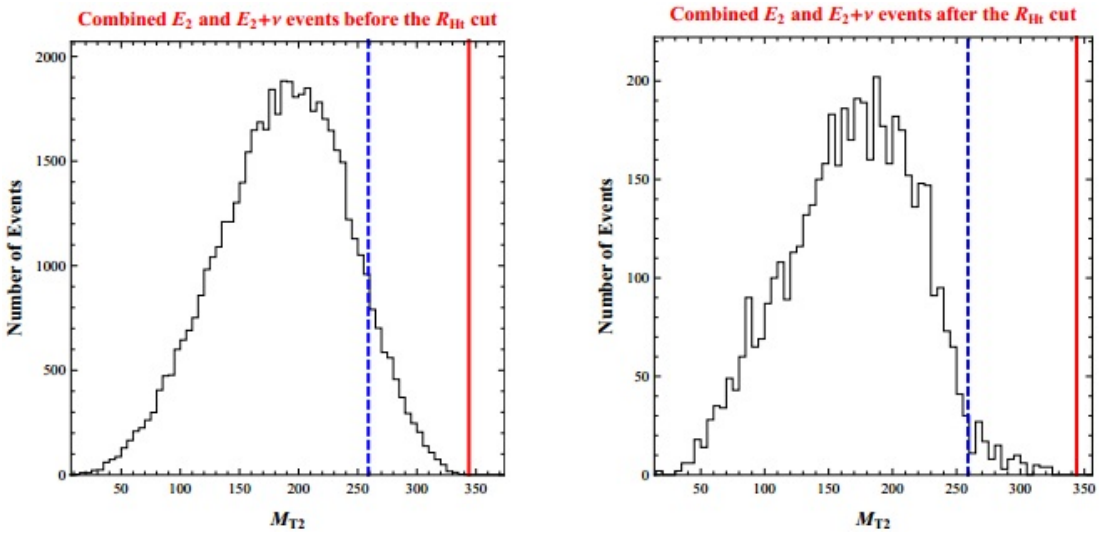

Figure 3.13: M_{T2} distribution for combined E_2 and $E_2 + \nu$ events ($1 : 2$ ratio) before (left panel) and after (right panel) the $R_{H_t} > 3$ cut for the case with two visible particles per decay chain. The mother mass is $M = 400$ GeV and the DM mass $m_{DM} = 150$ GeV. The trial mass is chosen to be $\tilde{m} = 9$ GeV. The solid red (dashed blue) lines represent the theoretical predictions for the upper edges of M_{T2} distributions for E_2 and E_3-type events, respectively.

- If we confirmed (as above) that the physics model is Z_3, we can then substitute the $M_{T2}^{\max}$ (for various trial DM masses) for events after the R_{P_t} cut into $\sqrt{C_{E_3}} + \sqrt{C_{E_3} + \tilde{m}^2} = M_{T2}^{\max}$ to find the parameter C_{E_3}. Based on the values of C_{E_2} and C_{E_3}, we can find the mother and DM masses simultaneously (again see the details in section 3.4.1).

  For the case with two visible particles per decay chain:

- We first find $M_{T2}^{\max}$ with different trial masses ($\tilde{m}$) for all events. We then draw a $M_{T2}^{\max}$ versus $\tilde{m}$ plot and find the location of the kink. This can give us both the mother and DM masses.

- We calculate the theoretical predictions of $M_{T2}^{\max}$ for E_3 type events using the mother and DM masses found in the first step.

- We apply the cut $R_{H_t} > 3$ and find $M_{T2}^{\max}$ with different trial masses ($\tilde{m}$) for events that passed the R_{H_t} cut. If the edge in M_{T2} reduces as a result of the cut, then we conclude that the underlying physics model is Z_3. Otherwise, it is a Z_2 model. Furthermore, if the new $M_{T2}^{\max}$ agrees with the theoretical prediction for E_3 type events found in the second step, then we have additional evidence that it is a Z_3 model.

In the above analysis, we have ignored the E_4 type events. However, including these events would not affect our analysis. Specifically, the $M_{T2}^{\max}$ for E_4 type events are always smaller than that of E_2 and E_3 type events (see Eqs. (3.11) and 3.19) so that they would not affect the upper edges of M_{T2} distribution for events *both* before and after the R_{P_t}/R_{H_t} cut. However, the survival rates for events after the cuts might be modified. In any case, we did not use the survival rates alone to distinguish between Z_2 and Z_3 models.

The above method of separating E_2 and E_3 type events using R_{P_t} or R_{H_t} cut has its limitations. If the DM mass is very light compared to the mother mass, then the emitted extra DM might not carry away as much energy. Thus, in E_3-type events, the visible particles in the decay chain with two DM particles can be closer (relative to the heavy DM case) in energy to those in the other decay chain. In fact, the DM becomes similar to a neutrino in this case so that the R_{P_t} or R_{H_t} distributions for E_3 type events should be similar to those for $E_2 + \nu$-type events, in

turn, not much different from that of E_2 type events (cf. heavy DM case), and the distinguishing power of the R_{P_t} or R_{H_t} cut is reduced. Therefore, in order for the R_{P_t} or R_{H_t} cut to efficiently separate E_2 and E_3 type events (and hence to distinguish between Z_3 and Z_2 models), we need the mass ratio between DM (m_{DM}) mother (M) masses $\frac{m_{DM}}{M}$ to be sizeable[30].

Finally, we note that the cut on ratio of momentum/energy on the two sides of the full event can also be used – either by itself or in conjunction with edges in M_{T2} – for the non-identical visible particles case (discussed in the previous section) in order to distinguish E_2 and E_3-type events. Of course, in that case, just the *identity* of the visible particles was enough to separate E_3 from E_2-type events.

3.5.3 Signal fakes by an (effective) 2nd DM particle

Next, we discuss the strategy to distinguish Z_2 models with two different DM particles) from Z_3 models, similar to the discussion in section 3.4.3. However, now we consider the two decay chains with one and two DM, respectively, in Z_3 models or with the two different DM particles in Z_2 models having identical visible particles (unlike in section 3.4.3). In this case, there is a modification from the case discussed earlier: we obtain one M_{T2} distribution by simply adding M_{T2} distributions for $E'_{2,\,3,\,4}$-type events in Z_2 models (and similarly, $E_{2,\,3,\,4}$-type events in Z_3 models). Let us consider first the case with a single visible particle per decay chain. As mentioned before, E'_2, E'_3, and E'_4-type events, i.e., "sub"-distributions in the case

[30] Of course, we need $m_{DM}/M < 0.5$ in order for the decay chain with two DM to be kinematically allowed.

of Z_2 models, all give a sharp upper edge in the M_{T2} distribution. This observation leads to the expectation of two sharp "kinks" – at the location of the "would-be" (smaller) edges of E_3', and E_4'-type events – in the middle of the *combined* M_{T2} distribution[31], in addition to the overall upper edge resulting from E_2' type events.[32].

Note that we had a similar discussion for Z_3 models in the beginning of section 3.5. However, in the case of Z_3 models only E_2 type events give a sharp upper edge and the other two type events, i.e., E_3 and E_4 give relatively longer tails (albeit with smaller endpoints than E_2-type events) so that two kinks in the combined M_{T2} distribution from E_3 and E_4 type events are not clear. Therefore, clear sharp kink(s) in the M_{T2} distribution would suggest that the events are the result of a Z_2 model (as discussed earlier).

For the case with more than one visible particle in each decay chain, the above idea of using kinks in M_{T2} distribution might fail since the edges of the sub-distributions are not sharp, even in the case of Z_2 models (as discussed in section 3.4.3). Instead, we can do cross-checks like in the case of non-identical visible particle(s) in the two decay chains (discussed in section 3.4.3) i.e., we first measure the masses of mother and DM particles by examining the location of the kink present in the maximum M_{T2} as a function of the trial DM mass for E_2 or E_2'-type events, and then predict the location of edges in the other types of events. Of course, in order to follow this strategy in the present case, one must first separate the events

[31] not to be confused with kink in edge of M_{T2} as a function of trial mass!

[32] The situation is similar to the double edge signal in the case of off-shell intermediate particles studied in Chapter 2

which are mixed, i.e., combination of $E_{2,\,3,\,4}$ in the case of Z_3 models and $E'_{2,\,3,\,4}$ for Z_2 models, into each individual type by applying P_t/H_t ratio cut (as explained in detail in section 3.5.1 for Z_3 models). Note that even mixed events in Z_2 models with a second DM-like particle can be separated by P_t/H_t ratio cut because the E'_3-type events also have an imbalance in the energy/momentum of the visible on the two decay chains due to the difference between m_{DM} and m'_{DM}.[33] Of course, we can also do a similar separation for the case of *one* visible particle in each decay chain (which was just discussed above) and then repeat the strategy which we discussed in section 3.4.3 for the case of visible particle in the two decay chains being non-identical, i.e., consider the shape of the separated M_{T2} distributions in order to distinguish Z_3 from Z_2 models.

[33]Obviously, one cannot then use this cut *on its own* in order to distinguish Z_3 from Z_2 models.

Chapter 4: Energy peak

4.1 Overview

In this chapter, we turn our attention to the energy spectrum of visible decay products. The method here is predicated upon the physical implication of the peak in the energy distribution of visible particles. Again, the signal processes of interest are similar to those in Chapters 2 and 3, i.e., the decay of a heavy mother particle, which is charged under the DM stabilization and SM symmetries, into DM particle(s) along with the relevant SM/visible particle(s). The basic observable here is the energy spectrum of such visible particle(s) as mentioned above.

We again emphasize that this technique can be complementary to the variables described in the previous two chapters in that it takes care of the cases which cannot be covered by either invariant or stransverse mass variables. To be more specific we exemplify the situation in which the decay of a mother particle involves only *two* DM particles and *one* SM/visible particle for Z_3 models. Clearly, the invariant mass discussed in Chapter 2 is *not* a good handle since there exists only one visible particle in each decay chain. Also the M_{T2} method described in Chapter 3 is *not* available since even Z_3 models allow only a single decay topology like Z_2 models so that for both symmetries only a single type of M_{T2} distribution is available.

Before studying the concrete model which will be described later in detail, we first review the recent observation about the peak position in the energy spectrum of a visible particle coming from a two-body decay process. Based on this review, we then generalize the basic idea to the three-body decays and derive new results about the energy spectrum. We point out that the energy peaks can be compared with "reference" values obtained by another observable, one of which is the M_{T2} variable which is thoroughly discussed in Chapter 3. It turns out that for two-body decays the peak position in the energy distribution is the same as the associated reference value while for three-body decays the peak position is smaller than its reference value. These new observations establish the general technique illustrated later in order to discern decays into between one DM particle and two DM particles.

As a realistic model consideration, we employ the decays of bottom partners at the LHC. There we show that the model process of interest satisfies the necessary conditions to ensure the validity of the theory argument mentioned above: 1) the visible decay product, the b quark, is relatively light compared with the expected mass of the bottom partner so that it can be treated as effectively massless, and 2) the bottom partners are predominantly produced via QCD, which guarantees unpolarized production of them. To be more realistic we identify the relevant backgrounds mimicking the signal process. It turns out that they are actually under control along with a suitable and reasonable choice of cuts, and thus one can see that our technique proposed here performs well enough even with backgrounds.

4.2 Theoretical observations on kinematics

As mentioned in the previous section, we begin first by reviewing the relevant theoretical observations about the kinematics of two-body and three-body decays. Specifically, we review the remarks on two-body decays described in [54]. We then generalize this result to three-body decay kinematics and study the features that distinguish it from two-body decay kinematics. We also briefly review applications of the kinematic variable M_{T2} to two-body and three-body decays and discuss the distinct features of the two different decay processes (see Chapter 3 and reference [4]).

For the two-body decay, we assume that a heavy particle A decays into a massless visible daughter b and another daughter X which can be massive and invisible:

$$A \to b\, X. \tag{4.1}$$

On the other hand, for a three-body decay the heavy particle A decays into particles b, X and another particle Y

$$A \to b\, X\, Y\,. \tag{4.2}$$

Like particle X, particle Y can also be massive and invisible, but it is *not* necessarily the same species as particle X.

4.2.1 The peak of the energy distribution of a visible daughter

4.2.1.1 Two-body decay

It is well-known that the energy of particle b in the rest frame of its mother particle A is fixed, which implies a δ function-like distribution, and the simple analytic expression for this energy can be written in terms of the two mass parameters m_A and m_X :

$$E_b^* = \frac{m_A^2 - m_X^2}{2m_A}\,. \tag{4.3}$$

Typically, the mother particle is produced in the laboratory frame at colliders with a boost that varies with each event. Since the energy is not an invariant quantity, it is clear that the δ function-like distribution for the energy as described in the rest frame of the mother is smeared as we go to the laboratory frame. Thus, naively it seems that the information encoded in Eq. (4.3) might be lost or at least not easily accessed in the laboratory frame. Nevertheless, it turns out that such information is retained. We denote the energy of the visible particle b as measured in the laboratory frame as E_b. Remarkably, the location of the peak of the laboratory frame energy distribution is the same as the fixed rest-frame energy given in Eq. (4.3):

$$E_b^{\text{peak}} = E_b^*, \tag{4.4}$$

as was shown in [54, 55].

Let us briefly review the proof of this result while looking ahead to the discussion of the three-body case. As mentioned before, the rest-frame energy of particle

b must be Lorentz-transformed. The energy in the laboratory frame is given by

$$E_b = E_b^* \gamma (1 + \beta \cos\theta^*) = E_b^* (\gamma + \sqrt{\gamma^2 - 1} \cos\theta^*) \,, \tag{4.5}$$

where γ is the Lorentz boost factor of the mother in the laboratory frame and θ^* defines the angle between the emission direction of the particle b in the rest frame of the mother and the direction of the boost $\vec{\beta}$, and where we have used the relationship $\gamma\beta = \sqrt{\gamma^2 - 1}$. If the mother particle is produced *un*polarized, i.e., it is either a scalar particle or a particle with spin produced with equal likelihood in all possible polarization states, the probability distribution of $\cos\theta^*$ is flat, and thus so is that of E_b. Since $\cos\theta^*$ varies between -1 and $+1$ for any given γ, the shape of the distribution in E_b is simply given by a rectangle spanning the range

$$E_b \in \left[E_b^* (\gamma - \sqrt{\gamma^2 - 1}),\ E_b^* (\gamma + \sqrt{\gamma^2 - 1}) \right] . \tag{4.6}$$

It is crucial to note that the lower and upper bounds of the above-given range are always smaller and greater, respectively, than $E_b = E_b^*$ for any given γ, so that E_b^* is covered by every single rectangle. As long as the distribution of the mother particle boost is non-vanishing in a small region near $\gamma = 1$, E^* is the only value of E_b to have this feature. Furthermore, because the energy distribution is flat for any boost factor γ, no other energy value has a larger contribution to the distribution than E_b^*. Thus, the peak in the energy distribution of particle b is unambiguously located at $E_b = E_b^*$.

The existence of this peak can be understood formally. From the fact that the differential decay width in $\cos\theta^*$ is constant, we can derive the differential decay

width in E_b for a fixed γ as follows:

$$\begin{aligned}\left.\frac{1}{\Gamma}\frac{d\Gamma}{dE_b}\right|_{\text{fixed }\gamma} &= \left.\frac{1}{\Gamma}\frac{d\Gamma}{d\cos\theta^*}\frac{d\cos\theta^*}{dE_b}\right|_{\text{fixed }\gamma} \\ &= \frac{1}{2E_b^*\sqrt{\gamma^2-1}}\Theta\left[E_b - E_b^*\left(\gamma-\sqrt{\gamma^2-1}\right)\right]\Theta\left[-E_b + E_b^*\left(\gamma+\sqrt{\gamma^2-1}\right)\right]\end{aligned} \tag{4.7}$$

where the two $\Theta(E_b)$ are the usual Heaviside step functions, which here merely define the range of E_b. To obtain the full expression for any given E_b, one should integrate over all γ factors contributing to this E_b. Letting $g(\gamma)$ denote the probability distribution of the boost factor γ of the mother particles, the normalized energy distribution $f_{\text{2-body}}(E_b)$ can be expressed as the following integral

$$f_{\text{2-body}}(E_b) = \int_{\frac{1}{2}\left(\frac{E_b}{E_b^*}+\frac{E_b^*}{E_b}\right)}^{\infty} d\gamma \frac{g(\gamma)}{2E_b^*\sqrt{\gamma^2-1}}. \tag{4.8}$$

The lower limit in the integral can be computed by solving the following equation for γ:

$$E_b = E_b^*\left(\gamma \pm \sqrt{\gamma^2-1}\right) \tag{4.9}$$

with the positive (negative) signature being relevant for $E_b \geq E_b^*$ ($E_b < E_b^*$). We can also calculate the first derivative of eq. (4.8) with respect to E_b as follows:

$$f'_{\text{2-body}}(E_b) = -\frac{1}{2E_b^*E_b}\text{sgn}\left(\frac{E_b}{E_b^*}-\frac{E_b^*}{E_b}\right) g\left(\frac{1}{2}\left(\frac{E_b}{E_b^*}+\frac{E_b^*}{E_b}\right)\right). \tag{4.10}$$

The solutions of $f'_{\text{2-body}}(E_b) = 0$ give the extrema of $f_{\text{2-body}}(E_b)$, and given the expression $f'_{\text{2-body}}(E_b)$ in Eq. (4.10), these zeros originate from those of $g(\gamma)$. For practical purposes, one can take $g(\gamma)$ to be non-vanishing for particles produced at colliders for any finite value of γ greater than 1 [1]. As far as zeros are concerned, two

[1]It must be noted that due to the finite energy of the collider, there is a kinematic upper limit

possible cases arise for $g(1)$ (corresponding to $E_b = E_b^*$). If it vanishes, $f'_{\text{2-body}}(E_b = E_b^*) \propto g(1) = 0$, which implies that the distribution has a unique extremum at $E_b = E_b^*$. If $g(1) \neq 0$, $f'_{\text{2-body}}(E_b)$ has an overall sign change at $E_b = E_b^*$. As a result, the distribution has a cusp and is concave-down at $E_b = E_b^*$. Moreover, the function $f_{\text{2-body}}(E_b)$ has to be positive to be physical, and has to vanish as E_b approaches either 0 or ∞, which is manifest from the fact that in those two limits the definite integral in Eq. (4.8) is trivial. Combining all of these considerations, one can easily see that the point $E_b = E_b^*$ is necessarily the peak value of the distribution in both cases.

4.2.1.2 Three-body decay

We now generalize the above argument to three-body decays. We denote the energy of the visible particle b measured in the rest frame of the mother particle A as $\bar{E}_b$. We also denote the normalized rest-frame energy distribution of particle b as $h(\bar{E}_b)$. In the two-body decay, this rest-frame energy is single-valued (see Eq. (4.3)), and so the corresponding distribution $h(\bar{E}_b)$ was trivially given by a δ-function. However, when another decay product is introduced, for instance, particle Y in Eq. (4.2), then the energy of particle b is no longer fixed, even in the mother's rest frame: $h(\bar{E}_b) \neq \delta\left(\bar{E}_b - E_b^*\right)$. Although the detailed shape of this rest-frame energy distribution is model-dependent, the kinematic upper and lower endpoints are model-independent. Since particle b is assumed massless, the lower endpoint

for the boost factor γ of the heavy mother particles. However, this kinematic limit is usually very large and can effectively be taken as infinite.

corresponds to the case where energy-momentum conservation is satisfied by particles X and Y alone. On the other hand, the upper endpoint is obtained when the invariant mass of X and Y equals $m_X + m_Y$,which corresponds to the situation where X and Y are produced at rest in their overall center-of-mass frame. Thus, we have

$$\bar{E}_b^{\min} = 0\,, \tag{4.11}$$

$$\bar{E}_b^{\max} = \frac{m_A^2 - (m_X + m_Y)^2}{2m_A}. \tag{4.12}$$

For any fixed γ, the differential decay width in the energy of particle b in the laboratory frame is *no longer* a simple rectangle due to non-trivial $h(\bar{E}_b)$. For any specific laboratory frame energy E_b, contributions should be taken from all relevant values of $\bar{E}_b$ and weighted by $h(\bar{E}_b)$. This can be written as

$$\frac{1}{\Gamma}\frac{d\Gamma}{dE_b}\bigg|_{\text{fixed }\gamma} = \int_{\bar{E}_b^<}^{\bar{E}_b^>} d\bar{E}_b \frac{h(\bar{E}_b)}{2\bar{E}_b\sqrt{\gamma^2-1}}\,, \tag{4.13}$$

where

$$\bar{E}_b^< = \max\left[\bar{E}_b^{\min},\ \frac{E_b}{\gamma+\sqrt{\gamma^2-1}}\right] = \frac{E_b}{\gamma+\sqrt{\gamma^2-1}}\,, \tag{4.14}$$

$$\bar{E}_b^> = \min\left[\bar{E}_b^{\max},\ \frac{E_b}{\gamma-\sqrt{\gamma^2-1}}\right]\,, \tag{4.15}$$

with E_b running from 0 to $\bar{E}_b^{\max}\left(\gamma+\sqrt{\gamma^2-1}\right)$. Again, since the visible particle is assumed massless, $\bar{E}_b^{\min}$ is zero and so the second equality in Eq. (4.14) holds trivially.

Finding an analytic expression for the location of the peak is difficult because of the model-dependence of $h(\bar{E}_b)$, and it follows that the precise location of the

peak is also model-dependent. Nevertheless, we can still obtain a bound on the position of the peak for fixed γ. Suppose that we are interested in the functional value of the energy distribution at a certain value of E_b in the laboratory frame; according to the integral representation given above, the relevant contributions to this E_b come from a range of center of mass energies which go from $\bar{E}_b'$ to $\bar{E}_b''$, where these are defined by

$$\bar{E}_b'(\gamma + \sqrt{\gamma^2 - 1}) = E_b \,, \tag{4.16}$$

$$\bar{E}_b''(\gamma - \sqrt{\gamma^2 - 1}) = E_b \,. \tag{4.17}$$

Each energy contributes with weight described by $h(\bar{E}_b)$, as implied by Eq. (4.13).

Let us assume that $\bar{E}_b'' = \bar{E}_b^{\max}$ and denote the corresponding energy in the laboratory frame as $E_b^{\rm limit}$, given by

$$E_b^{\rm limit} = \bar{E}_b^{\max}(\gamma - \sqrt{\gamma^2 - 1}). \tag{4.18}$$

From these considerations, it follows that all rest-frame energies in the range from $\bar{E}_b' = \frac{E_b^{\rm limit}}{(\gamma+\sqrt{\gamma^2-1})}$ to $\bar{E}_b'' = \bar{E}_b^{\max}$ contribute to a chosen energy in the laboratory frame, $E_b^{\rm limit}$. On the other hand, any laboratory frame energy greater than $E_b^{\rm limit}$ has contributions from $\bar{E}_b' > \frac{E_b^{\rm limit}}{(\gamma+\sqrt{\gamma^2-1})}$ to $\bar{E}_b'' = \bar{E}_b^{\max}$; the relevant range of the rest-frame energy values will shrink so that the peak cannot exceed $E_b^{\rm limit}$:

$$E_b^{\rm peak}\Big|_{\text{fixed }\gamma} < \bar{E}_b^{\max}(\gamma - \sqrt{\gamma^2 - 1}) \leq \bar{E}_b^{\max} \quad \text{for any fixed } \gamma. \tag{4.19}$$

In order to ensure that the first inequality holds even for $\gamma = 1$, we assume in the last equation that $h\left(\bar{E}_b^{\max}\right) = 0$, which is typically the case for a three-body decay. In order to obtain the shape of the energy distribution of particle b in the

laboratory frame, all relevant values of γ should be integrated over as with the two-body kinematics in the previous section. Hence, the laboratory frame distribution reads

$$f_{\text{3-body}}(E_b) = \frac{1}{\Gamma}\frac{d\Gamma}{dE_b} = \int_{\bar{E}_b^<}^{\bar{E}_b^>} d\bar{E}_b \int_{\gamma_{\min}(E_b,\,\bar{E}_b)}^{\infty} d\gamma \frac{g(\gamma)h(\bar{E}_b)}{2\bar{E}_b\sqrt{\gamma^2-1}}\,. \tag{4.20}$$

Since the argument leading to Eq. (4.19) holds for every γ, the superposition of contributions from all relevant boost factors does not alter this observation. Therefore, we can see that irrespective of $g(\gamma)$ and $h(\bar{E}_b)$, the peak position of the energy distribution of particle b in the laboratory frame is *always* less than the maximum rest-frame energy:

$$E_b^{\text{peak}} < \bar{E}_b^{\max}\,. \tag{4.21}$$

To gain intuition on the magnitude of the typical difference between the peak of the energy distribution in the laboratory frame and the maximum rest frame energy, we show the ratio of the two as a function of γ in Figure 4.1. From the figure, it is clear that as the typical γ increases beyond $\gamma = 1$, i.e., as the system becomes more boosted, the location of the peak in the energy distribution becomes smaller. An appreciable shift of order 10% is achieved for a modest boost of order $\gamma - 1 \simeq 10^{-2}$.

It should be noted that all results here for both two-body and three-body decays are valid to leading order in perturbation theory. The presence of extra radiation in the decay will effectively add extra bodies to the relevant kinematics. Specifically, extra radiation can turn a two-body decay into a three-body one, which

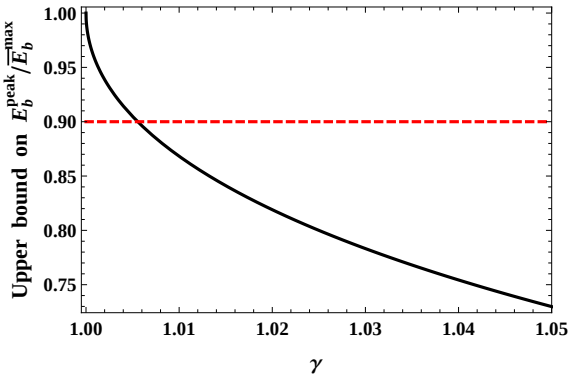

Figure 4.1: Relative separation of the peak of the laboratory energy distribution from the maximal energy in the center-of-mass frame of the three-body decay kinematics as per Eq. (4.21). The horizontal red dashed line marks a 10% variation of the peak energy from the maximal value in the rest frame.

for our investigation would constitute a fake signal of two DM particles being produced in the decay of a heavy new physics particle. Therefore, we have to remark that in some cases, for instance, when the heavy new physics is typically produced with very small boost, the differences between the two scenarios of DM stabilization may be tiny and a study beyond leading order may be necessary. From Figure 4.1 it seems, however, that the typical effect of the presence of two dark matter particles per decay of the heavy new particle is to easily induce an order one effect on the peak position. Therefore, we anticipate that such an effect would be much larger than the expected uncertainty from higher order corrections, which we estimate to be of order 10%.

Before closing this section, we emphasize that we shall use the right-hand sides of Eqs. (4.4) and (4.21) as "reference" values to which the measurements of their respective left-hand side values (extracted from the energy distribution) are to be

compared. In the next section, we show that such a reference value can, in fact, be extracted from an analysis of M_{T2}.

4.2.2 The kinematic endpoint of the M_{T2} distribution

In this section, we quote some of the results provided in Chapter 3 and discuss new observations for later usage. For the M_{T2} analysis, we make further assumptions as follow:

1) all massive decay products, i.e., particles X and Y in Eqs. (4.1) and (4.2), are invisible;

2) the mother particles A are produced in pairs;

3) the entire decay process is symmetric in the sense that the mother particles are pair-produced and then decay to the same decay products, that is

$$pp \to AA\,, \quad A \to X\ b \quad \text{or} \quad A \to b\ X\ Y\,, \tag{4.22}$$

for the two-body decay and the three-body decay, respectively.

The last assumption is especially relevant to make contact with the problem of distinguishing the Z_2 and the Z_3 dark matter interactions, as detailed in the introduction.

As briefly reviewed in Chapter 3, for two-body decays, the M_{T2} distribution has a kinematic endpoint

$$M^{\max}_{T2,2-\text{body}}(\tilde{m}) = C_{2-\text{body}} + \sqrt{C^2_{2-\text{body}} + \tilde{m}^2}\,, \tag{4.23}$$

where the C parameter is given by

$$C_{2-\text{body}} = \frac{m_A^2 - m_X^2}{2m_X}. \tag{4.24}$$

This C parameter can be deduced from Eq. (4.23) by substituting the experimental value of the kinematic endpoint and the chosen trial DM mass. On the other hand, for three-body decays, the M_{T2} distribution has a kinematic endpoint

$$M_{T2,3-\text{body}}^{\max}(\tilde{m}) = C_{3-\text{body}} + \sqrt{C_{3-\text{body}}^2 + \tilde{m}^2}\,, \tag{4.25}$$

where the C parameter is given by

$$C_{3-\text{body}} = \frac{m_A^2 - (m_X + m_Y)^2}{2m_A}. \tag{4.26}$$

Before closing the Section, a critical observation is in order. According to Eqs. (4.23) and (4.25), we see that the observed values of $M_{T2}^{\max}$ as a function of the various chosen trial DM masses ($\tilde{m}$) can be fitted with the same equation in both the two- and three-body cases:

$$M_{T2,\text{obs.}}^{\max} = C + \sqrt{C + \tilde{m}^2}\,, \tag{4.27}$$

where the parameter C can be extracted from the fit. This will be used in the following to extract the C parameter without making any assumption on the number of invisible products in the decay.

The fact that the M_{T2} endpoint can be described with the same parametrization in terms of a generic C parameter, as in Eq. (4.27), is not surprising. In fact, for the two-body case in events near the endpoint each mother needs to have its decay products (b and X) emitted at the same rapidity (although the two mothers A can be at different rapidities) [4]. Analogously for the three-body case, the

two invisible decay products (X and Y) and the particle b produced at the same interaction vertex all need to share the same rapidity. In such a situation, the two invisible particles are kinematically equivalent to a single invisible particle, and so the decay can still be effectively reduced to a two-body decay. In this sense, $M_{T2}^{\max}$ for the three-body case corresponds to the same kinematic configuration that gives the endpoint for the two-body case. However, it must be noted that the C parameter actually provides different information in the two cases. For two-body decays, the C parameter in Eq. (4.24) is the same as the rest-frame energy of particle b in Eq. (4.3), whereas for three-body decays, the C parameter in Eq. (4.26) is the same as the maximum energy of particle b in the rest frame in Eq. (4.12) [2]:

$$C = \begin{cases} E_b^* & \text{for two-body decays} \\ \\ \bar{E}_b^{\max} & \text{for three-body decays.} \end{cases} \tag{4.28}$$

This observation puts us in the position to extract the C parameter from the M_{T2} distribution and compare it with the peak value in the energy distribution of the visible particle so as to test the nature of the decay.

[2] Alternatively one can interpret the C parameter of the three-body decay as the analogy of the two-body case where the mass of the single DM particle is replaced by the mass of the effective single body made of the two DM, i.e. the sum of the mass of the two DM particles, as apparent from the comparison of Eqs. (4.24) and (4.26).

4.3 General Strategy to distinguish Z_2 and Z_3

We now apply the above theoretical observation to the determination of the underlying DM stabilization symmetry. To pinpoint this stabilization symmetry, we study the energy distribution of the particle b from the process defined in Eq. (4.22). In particular, we exploit the relation between this energy distribution and the distribution of the M_{T2} variable in the same process. As will be clear from the following analysis, the correlation between features of the distribution of these two observables will allow us to make a much firmer statement than merely utilizing one of them.

In point of fact, the M_{T2} distribution of the process Eq. (4.22) could itself in principle be a good discriminator between Z_2 and Z_3 models. Indeed, as discussed in Section 4.2.2, the kinematic endpoint in the M_{T2} distribution of the visible particles from a duplicate three-body decay, which is realized under Z_3 symmetry, develops a longer tail than that of two-body decays, the latter being realized under Z_2 symmetry. Therefore, a less sharp fall-off near the endpoint could be a sign of more than one invisible particle in the decay (see Chapter 3 and reference [73] for more details). However, shape analyses of the tail of the M_{T2} distribution are rather delicate, especially in the presence of a background. Besides the issues raised by the backgrounds, there are also some inherent complications in using only the shape of the M_{T2} distribution to determine the underlying stabilization symmetry. For example, the effects of spin correlation could change the shape of the M_{T2} distribution, particularly the behavior near the upper endpoint of the distribution. In other words, a certain "choice" of spin correlation could alter the sharp edge of the M_{T2}

distribution in Z_2 models, mimicking the typical distribution shape characteristic of Z_3 models, and vice versa.

Alternatively, one could try to use the energy distribution of the b particles in events from the process Eq. (4.22). Recall that the distribution of the visible particle energy in their mother particle's rest frame is δ function-like in Z_2 models, whereas the distribution in Z_3 models is non-trivial. Therefore, once the decay products are boosted to the laboratory frame from their mother particle's rest frame, the energy distribution for Z_3 physics is expected to be relatively broader for a given mother particle. However, it is very hard to quantify the width of the resulting energy distributions in both Z_2 and Z_3 models because it is strongly model-dependent. In particular, the shape of the energy distribution in the laboratory frame is governed by the boost distributions of the mother particles, which are subject to uncertainties. Such uncertainties come from the fact that we are not *a priori* aware of the underlying dynamics governing the new physics involved in the process Eq. (4.22), which affects, for instance, the production mechanism of the mother particles.

In order to overcome the difficulties described above, we propose here a combined analysis of the two distributions. The goal is to obtain a more robust technique that is sensitive to the differences between the Z_2 and the Z_3 models but largely independent of the other details of the models. Also, we aim at formulating a method that is less demanding from an experimental standpoint and more stable against the inclusion of experimental errors. The analysis proceeds in two steps as explained in the following.

From the data, one first produces the M_{T2} distribution using a trial DM mass

and extracts the kinematic endpoint $M_{T2,\text{obs.}}^{\max}$. Then, by substituting the measured endpoint into the function given in Eq. (4.27), one obtains the C parameter. As illustrated in Eq. (4.28), the C parameter has different physical implications depending on the stabilization symmetry of the DM. For the Z_2 case, it is the energy of the visible particle in the rest frame of its mother particle, and by virtue of [54, 55], it is expected to be the value of the peak of the energy distribution in the laboratory frame. Alternatively, for a Z_3 model the C parameter is an upper bound to the peak of the energy distribution in the laboratory frame. Therefore, the comparison between the extracted C parameter and the peak position in the b particle energy distribution enables us to determine whether the relevant physics is Z_2 or Z_3. This observation can be summarized as follows:

$$\begin{aligned} E_{b,\text{obs.}}^{\text{peak}} &= C_{\text{obs.}} = \frac{m_{B'}^2 - m_\chi^2}{2m_{B'}} \qquad \text{for } Z_2 \\ E_{b,\text{obs.}}^{\text{peak}} &< C_{\text{obs.}} = \frac{m_{B'}^2 - 4m_\chi^2}{2m_{B'}} \qquad \text{for } Z_3. \end{aligned} \tag{4.29}$$

Some remarks must be made about our proposal. First, the use of the distribution of M_{T2} is needed only to the extent that this is useful to extract the C parameter. In fact, in order to find the reference value needed for the comparison of Eq. (4.29), any other observable that is sensitive to the relevant combination of masses could be used. Second, spin correlation effects do not change the location of the peak in the energy distribution of the b particle as long as the bottom partners are produced unpolarized, as discussed earlier. Additionally, although the overall shape near the endpoint of the M_{T2} distribution could be affected by non-trivial spin correlation effects, the endpoint value is not. Furthermore, substantial errors

in the determination of the M_{T2} endpoint can be tolerated. In fact, as shown in Figure 4.1, the difference between the reference value and the typical peak of the energy distribution in a three-body decay is quite large.

For the above reasons, we believe that compared with other methods which utilize only M_{T2}, the method presented here is more general and more robust in highlighting the different kinematic behavior inherent to the two different stabilization symmetries.

In order to demonstrate the feasibility of the proposed analysis, we work out in detail an application of our method to the case of pair production of partners of the b quark that decay into a b quark and one or two invisible particles in the next section.

4.4 Application to b quark partner decays

In this Section, we study in detail the production of b quark partners, B', and their subsequent decay into b quarks and one or two DM particles. As mentioned in the introduction, b quark partners occur in many well-motivated extensions to the SM. In the following, we apply the results of Sections 4.2 and 4.3 with the underlying goal of "counting" the number of DM particles in the above decay process. Although we employ DM and a b quark partner with specific spin for the purpose of illustrating our technique, we emphasize that our method can be applied for any appropriate choice of spins for the involved particles. In fact, the choice of spins does not alter our results so long as the mother particles are produced unpolarized.

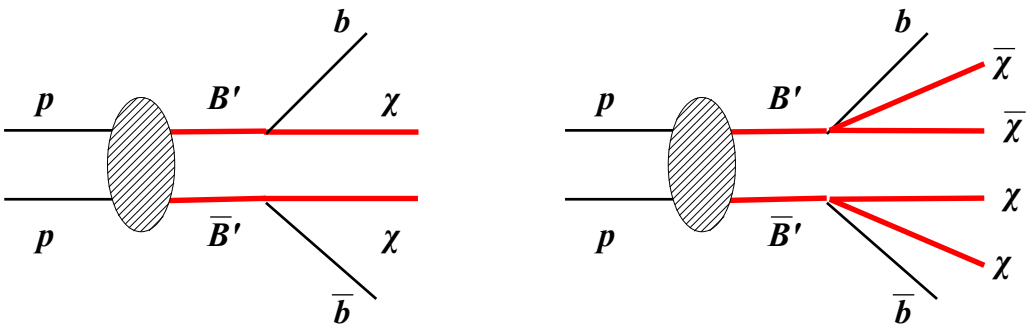

Figure 4.2: The signal processes of interest for Z_2 (left panel) and Z_3 (right panel) stabilization symmetry of the dark matter particle χ.

Because the b quark partners are charged under QCD, the dominant production channel at hadron colliders would be via color gauge interactions, which guarantee that the b quark partners would be produced unpolarized and in pairs. Due to the fact that these particles are produced in pairs, the above results given for M_{T2} are in force. Furthermore, the unpolarized production guarantees that the results of Section 4.2 can be applied to the energy distribution.

In what follows, we consider the QCD pair production of heavy b quark partners at the LHC running at a center-of-mass energy $\sqrt{s} = 14$ TeV, and we take as signal processes:

$$pp \to B'\bar{B}' \to b\bar{b}\chi\chi \qquad \text{for } Z_2\,, \tag{4.30}$$

$$pp \to B'\bar{B}' \to b\bar{b}\chi\chi\bar{\chi}\bar{\chi} \qquad \text{for } Z_3\,, \tag{4.31}$$

where χ is the DM particle. Once produced, we assume that each B' decays into a b quark and either one or two stable neutral weakly-interacting particles (see also Figure 4.2). These processes will appear in the detector as jets from the two b quarks

and missing transverse energy

$$pp \to b\bar{b} + \not{E}_T \qquad \text{for } \textit{both } Z_2 \text{ and } Z_3. \tag{4.32}$$

Note that our program is meant to be carried out only after the discovery of the heavy b quark partner. In fact, our focus is *not* on discovery, but on determining what type of symmetry governs the associated decays of such a particle once the discovery is made, specifically in the $b\bar{b} + \not{E}_T$ channel. In order to achieve this goal, a high integrated luminosity would be required to make a definitive determination of the underlying symmetry. Likewise, compared with the criteria necessary to claim the discovery of such a resonance, a different set of event selection conditions would be likely have to be used in order to make a definitive determination of the underlying stabilization symmetry.

For our proof-of-concept example, we take $m_{B'} = 800$ GeV and $m_\chi = 100$ GeV while noting that searches for scalar b quark partners such as reference [74] are in principle sensitive to our final state. Unfortunately, there is no available interpretation of this search in terms of a fermionic partner; a naive rescaling of the current limits on a scalar partner with mass of about 650 GeV shows that our choice of mass parameters might be on the verge of exclusion. However, we remark that our choice is *only* for the purpose of illustrating our technique, and can just as easily be applied to a heavier B'.

There are several SM backgrounds that are also able to give the same detector signature as our signal. Since we require a double b-tagging, the main backgrounds to our signal are the following three processes: i) $Z + b\bar{b}$, where Z decays into two

neutrinos, ii) $W^{\pm} + b\bar{b}$, where the W decay products are not detected, and iii) $t\bar{t}$ where again the two W's from the top decay go undetected [3]. The first background is irreducible, while the latter two are reducible.

To reduce these backgrounds to a level that allows clear extraction of the features of the b-jet energy and M_{T2} distribution, we put constraints on the following observables:

- $p_{T,\,j_1}$ is the transverse momentum of the hardest jet in the event,
- $\not{E}_T = |-\sum_i \vec{p}_{T,\,i}|$ is the missing transverse energy of the event and is computed summing over all reconstructed objects,
- $S_T = \frac{2\lambda_2}{\lambda_1+\lambda_2}$ is the transverse sphericity of the event. Due to the tendency of QCD to produce strongly directional events, the background processes typically have small sphericity, while decay products of a heavy B' are expected to be significantly more isotropic and hence will preferentially have a larger sphericity [75].

In general, the mismeasurement of the momenta of the observable objects used to compute $\not{E}_T$ can produce an instrumental source of $\not{E}_T$, as opposed to a "physical" source of $\not{E}_T$ which originates from invisible particles carrying away momentum. The mismeasurement of $\not{E}_T$ can grow as objects of larger p_T are found in an event, and it is therefore useful to compare the measured missing transverse energy with some measure of the global transverse momentum of the event. For this reason, we

[3] By undetected we mean that the decay products do not pass our selection criteria or are legitimately undetected.

introduce the quantity [4]

$$f = \not{E}_T / M_{\text{eff}} \quad \text{where} \quad M_{\text{eff}} \equiv \not{E}_T + |p_{T\,j_1}| + |p_{T\,j_2}|\,,$$

which is expected to be small for events where the $\not{E}_T$ comes from mismeasurements, but should be large for events where invisible particles carry away momentum. Furthermore, when the instrumental $\not{E}_T$ originates mostly from the mismeasurement of a single object, the $\not{E}_T$ is expected to point approximately in the direction of one of the visible momenta. Therefore, the events where the $\not{E}_T$ is purely instrumental are expected to have a small

$$\Delta\phi(\not{E}_T, \text{jets}),$$

which is the angle between the direction of the missing transverse momentum and any $\vec{p}_{T\,j}$.

To select signal events and reject background events, we choose the following set of cuts:

$$\text{0 leptons with } |\eta_l| < 2.5 \text{ and } p_{T\,l} > 20 \text{ GeV for } l = e,\ \mu,\ \tau, \tag{4.33}$$

$$\text{2 } b\text{-tagged jets with } |\eta_b| < 2.5 \text{ and } p_{T\,b_1} > 100 \text{ GeV}, \ p_{T\,b_2} > 40 \text{ GeV}, \tag{4.34}$$

$$\not{E}_T > 300 \text{ GeV}, \tag{4.35}$$

$$S_T > 0.4\,, \tag{4.36}$$

$$f > 0.3\,, \tag{4.37}$$

$$\Delta\phi_{\min}(\not{E}_T, b_i) > 0.2 \text{ rad for all the selected } b\text{-jets } b_i\,. \tag{4.38}$$

[4] Sometimes a slightly different quantity $f' = \not{E}_T / \sum_i |p_{T,i}|$ is used in the same context of our f. The two variables have the same meaning and give similar results.

Note that the our cuts are of the same sort used in experimental searches for new physics in final states with large $\not{E}_T$, 0 leptons and jets including 1 or more b-jets (see, for instance, [76]). However, notice that in our analysis, we privilege the strength of the signal over the statistical significance of the observation. As already mentioned, we imagine this investigation being carried out after the initial discovery of a B' has taken place. Hence, we favor enhancing the signal to better study the detailed properties of the interaction(s) of B'. For this reason, we cut more aggressively on $\not{E}_T$ and S_T than in experimental searches and other phenomenological papers focusing on the discovery of B's (see, for example, [77]).

We consider quarks separated by $\Delta R > 0.7$ as jets. With this as our condition on jet reconstruction, the cuts of eq. (4.33)–(4.38) can be readily applied to the signals and to the $Z + b\bar{b}$ background; the resulting cross-sections are shown in Table 4.1. These cross-sections are computed from samples of events obtained using the Monte Carlo event generator `MadGraph5` v1.4.7 [78] and parton distribution functions `CTEQ6L1` [79]. For the sake of completeness, we specify that in generating these event samples we assumed a fermionic B' and a weakly interacting scalar χ. However, as already stressed, we anticipate that different choices of spin for these particles will not significantly affect our final result because the production via QCD gives rise to an effectively unpolarized sample of b quark partners.

The estimate of the reducible backgrounds requires more work, as it is particularly important to accurately model the possible causes that make

$$pp \to t\bar{t} \to b\bar{b} + X \quad \text{and} \quad pp \to W^{\pm} + b\bar{b}$$

Table 4.1: Cross-sections in fb of the signals and the dominant background $Z + b\bar{b}$ after the cuts of Eqs. (4.33)–(4.38). The mass spectrum for the signals is $m_{B'} = 800$ GeV and $m_\chi = 100$ GeV. The line "No cuts" is for the inclusive cross-section of the signal. The line "precuts" gives the cross-section after the cuts $\not{E}_T > 60$ GeV, $p_{T,b} > 30$ GeV, $\eta_b < 2.5, \Delta R_{bb} > 0.7$ that are imposed solely to avoid a divergence in the leading order computation of the background. In the last line, the rate of tagging b quarks is assumed 66% [80].

Cut	Z_2 $(B \to b\chi)$	Z_3 $(B \to b\chi\bar{\chi})$	$Z + b\bar{b}$ $(Z \to \nu\bar{\nu})$
No cuts	159.75	159.75	–
Precuts	139.89	136.73	2927
$p_T^{j_1} > 100$ GeV, $p_T^{j_2} > 40$ GeV	139.64	133.76	971.9
$\not{E}_T > 300$ GeV	101.73	69.01	19.93
$f > 0.3$	89.66	65.21	19.40
$\Delta\phi_{\min} > 0.2$	88.95	64.31	18.81
$S_T > 0.4$	30.03	16.07	1.96
2 b-tagged jets	13.29	7.18	0.87

a background to our $2b+\not{E}_T$ signal. In fact, these processes have larger cross sections than $Z+b\bar{b}$. However, they also typically give rise to extra leptons or extra jets with respect to our selection criteria in Eqs. (4.33)–(4.38). Therefore, in order for us to consider them as background events, it is necessary for the extra leptons or jets to fail our selection criteria. Accordingly, the relevant cross-section for these processes is significantly reduced compared to the total. In fact, we find that $t\bar{t}$ and $W^\pm b\bar{b}$ are subdominant background sources compared to $Z + b\bar{b}$. In what follows, we describe how we estimated the background rate from $t\bar{t}$ and $W^\pm b\bar{b}$.

An accurate determination of the proportion of $t\bar{t}$ and $W^\pm b\bar{b}$ background events that pass the cuts in eq. (4.33)–(4.38) depends on the finer details of the detector used to observe these events. However, the most important causes for the extra jets and leptons in the reducible backgrounds to fail our jet and lepton identification criteria can be understood at the matrix element level. We estimate the rate of

the reducible backgrounds by requiring that at the matrix element level, a suitable number of final states from the $t\bar{t}$ and $W + b\bar{b}$ production fail the selections of Eqs. (4.33)–(4.38) for one of the following reasons:

- the lepton or quark is too soft, i.e., $p_{T,l} < 20$ GeV, $p_{T,j} < 30$ GeV
- or the lepton or quark is not central, i.e. $|\eta_{l,j}| > 2.5$.

Additionally, when any quark or lepton is too close to a b quark, we consider them as having been merged by the detector, and the resulting object is counted as a b quark (i.e., $\Delta R_{bl} < 0.7$, $\Delta R_{bj} < 0.7$), or if any light quark or lepton is too close to a light jet, they are likewise merged, and the resulting object is counted as a light quark (i.e., $\Delta R_{jl} < 0.7$, $\Delta R_{jj} < 0.7$). In the latter case, the light "jet" resulting from a merger must then also satisfy the p_T and η criteria given above for going undetected.

Using our method to estimate the results on the backgrounds in reference [77], the analysis of which was carried out with objects reconstructed at the detector level, we find that our estimates agree with reference [77] within a factor of two. Because we successfully captured the leading effect, we did not feel the necessity of pursuing detector simulations in our analysis.

Estimating the reducible background after the selections in Eqs. (4.33)–(4.38), we find that $t\bar{t}$ and $W + b\bar{b}$ are subdominant compared to $Z + b\bar{b}$. The suppression of the reducible backgrounds, and in particular, of $t\bar{t}$, comes especially from the combination of the S_T and $\not{E}_T$ cuts. This is shown in Figure 4.3, where we plot the $\not{E}_T$ distributions of the three backgrounds under different S_T cuts: $S_T > 0$,

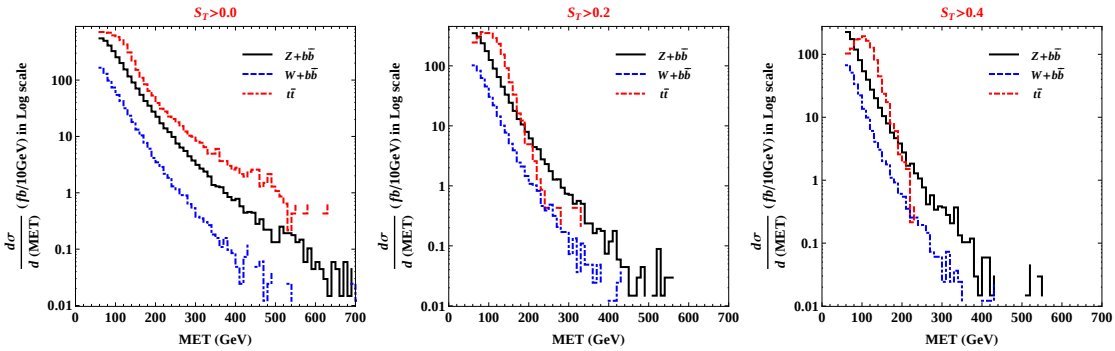

Figure 4.3: $\not{E}_T$ distributions for the three backgrounds ($Z + b\bar{b}$, $W^{\pm} + b\bar{b}$, and $t\bar{t}$) with S_T cuts of increasing magnitude, $S_T > 0.0$, > 0.2, and > 0.4 from the left panel to the right panel. In each plot, the black solid, blue dotdashed, and red dashed curves represent $Z + b\bar{a}b$, $W^{\pm} + b\bar{b}$, and $t\bar{t}$, respectively.

$S_T > 0.2$, and the cut $S_T > 0.4$, which is used in our final analysis. Clearly, one can see that for a $\not{E}_T$ as large as our requirement in Eqs. (4.33)–(4.38), the dominant background is $Z + b\bar{b}$, and that in particular, the $t\bar{t}$ is significantly suppressed by simultaneously requiring a large $\not{E}_T$ and moderate S_T cut (rightmost panel in the figure).

As the first step in our analysis, we compute the M_{T2} distributions expected at the LHC for our two potential cases of new physics interactions, Z_2 and Z_3. The distributions for the two cases are shown in Figure 4.4. Since we found that with the selections of Eqs. (4.33)–(4.38), the $Z + b\bar{b}$ process is the dominant background, as seen in the figure, we consider it the *only* background process. The two distributions have been computed assuming a trial mass $\tilde{m} = 0$ GeV and have an endpoint at 787.5 GeV and 750 GeV for the Z_2 and the Z_3 cases, respectively. Interpreting the distributions under the naïve assumption of one invisible particle per decay of the

B', we obtain from Eq. (4.27) a C parameter that is 383.75 GeV and 375 GeV for Z_2 and Z_3, respectively. These are the reference values that we need for the analysis of the energy distributions [5].

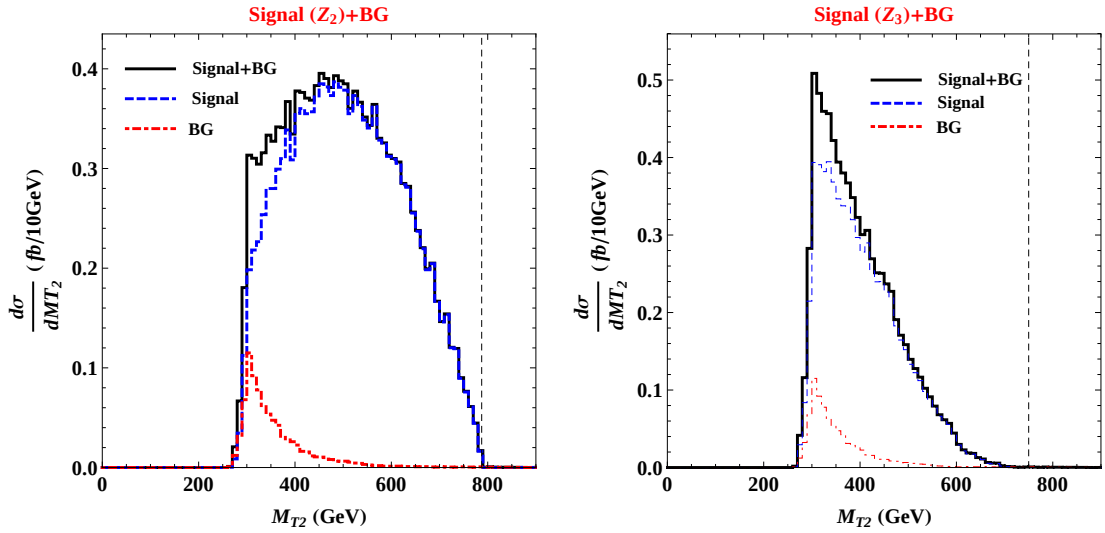

Figure 4.4: M_{T2} distributions after the cuts of Eqs. (4.33)–(4.38). The chosen masses for the new particles are $m_{B'} = 800$ GeV and $m_\chi = 100$ GeV. The left panel is for the Z_2 signal while the right panel is Z_3 (both in blue). In both cases, the background is $Z + b\bar{b}$ (red). In both panels, the black line represents the sum of signal and background. The black vertical dashed lines denote the theoretical prediction for the endpoints.

As the final step in our analysis, we need to compare the obtained reference values with the peaks of the energy distributions. These distributions are shown in

[5] We remark that as apparent from the figure, the signal rate is much larger than that of the background, and therefore the shape of the distribution expected at the LHC largely reflects the features of the signal. In this case, it seems particularly straightforward to extract the endpoint of the distribution. In other cases where the background is larger, the extraction of the endpoint may require a more elaborate procedure, especially for the Z_3 case where the endpoint is much less sharp (see, for example, Chapter 3 and references [8, 81, 82]).

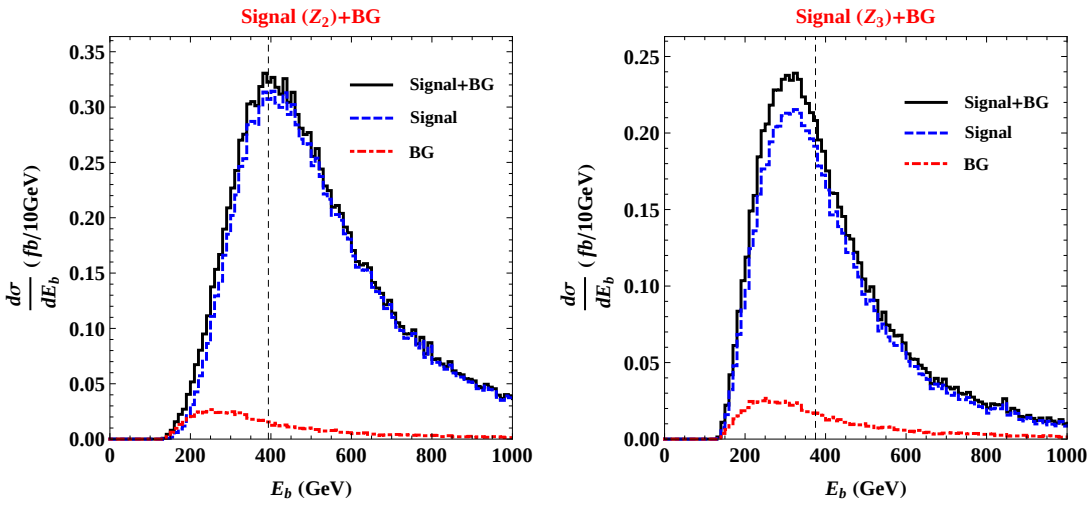

Figure 4.5: Energy distributions of the b quarks after the cuts of Eqs. (4.33)–(4.38). The chosen masses for the new particles are $m_{B'} = 800$ GeV and $m_\chi = 100$ GeV. The left panel is for the Z_2 signal, while the right panel is Z_3 (both in blue). In both cases, the background is $Z + b\bar{b}$ (red). In both panels, the black line represents the sum of signal and background. The black vertical dashed lines denote the reference values extracted from the M_{T2} distributions of Figure 4.4 using Eq. (4.27).

Figure 4.5. We clearly see that the location of the peak in the energy distribution in the Z_2 case coincides with the associated reference value, whereas for the Z_3 case the peak is, as expected, at an energy less than the associated reference value. We remark that in the Z_3 case, the peak of the energy distribution is significantly displaced with respect to the reference value. Therefore, we expect our test of the Z_2 nature of the interactions of the B' to be quite robust under the inclusion of both experimental and theoretical uncertainties, such as the smearing of the peak due to the resolution on the jet energy, the errors on the extraction of the reference value obtained from the M_{T2} analysis, and the shift of the peak that is expected due to radiative corrections to the leading order of the decay of the B'.

Chapter 5: Conclusions

The WIMP is a well-motivated dark matter paradigm since its mass scale is naturally connected to the weak scale. Particle physics also motivates new physics at the weak scale by different reasons like the (famous) gauge hierarchy problem. Given this energy scale, the ongoing LHC experimental program is anticipated to prove the existence of such a dark matter candidate. Once dark matter is discovered, one of the next stages in investigating the DM is to determine its various physical properties such as mass, DM stabilization symmetries, spin, coupling constants and so on. In this thesis, we proposed various ways of achieving such a goal at hadron colliders. In particular, of them we have focused on mass and DM stabilization symmetries.

Various cosmological and astrophysical observations and the relevant theory consideration advocate that the DM particle must be massive so that pinning down its mass is interesting *per se*. Due to its massiveness, the DM particle would be destined to decay into lighter particles, which would lead to inconsistency with the current observation for the DM relic abundance. In order to protect the DM particle from decaying, many new physics models with a DM candidate introduce a new unbroken symmetry under which DM is non-trivially charged while the known/SM

particles are charged neutral so that DM becomes stabilized. Surprisingly enough, in most cases a parity type (Z_2) symmetry is employed. However, we emphasize that in principle any discrete or continuous global symmetries can be used for stabilizing the DM particle. It is therefore important to identify the DM stabilization symmetries in experiment. As a concrete example, we have chosen Z_3 symmetry, which is the simplest non-Z_2, to contrast with the Z_2 symmetry. We then pointed out that the decay of a *single* (Z_3-charged) mother particle contain one or two DM particles whereas a Z_2-charged one does only one.

Since the DM particle is not directly observable by construction, typically its intrinsic properties are deduced by the introduction of various kinematic variables rather than the direct reconstruction. We here employed the invariant mass distribution, the stransverse/M_{T2} distribution and the peak in the energy distribution of visible particles as our main toolkits. We again stress that the three kinematic variables play a complementary role to one another, i.e., cases that are not covered by one variable can be taken care of by others.

Invariant mass: In Chapter 2 we discussed how to determine the DM properties using the invariant mass distribution. Specifically, when a mother particle decay via off-shell intermediate states into the same visible particles along with one and two DM (for the case of Z_3 symmetry), it may be possible to observe a *double-edge* in the distribution of these visible particles (vs. single edge for Z_2 symmetry). In fact, the difference between the location of the edges will be a direct measure of the mass of the dark matter particle for Z_3 models. On the other hand, when the intermediate

particles are on-shell, we also pointed out the possibility of a very distinctive feature appearing in the invariant mass distribution of two visible particles in the case of Z_3 symmetry: a *cusp* dividing the distribution into two regions. This happens when two DM particles emerge from the same chain, with one of these DM particles being situated in-between the two SM particles.

We further generalized the idea of extracting information with the invariant mass variable to the generic decay of a mother particle into any number of invisible particles along with two visible particles. We there utilized full information from the associated invariant mass distribution: 1) overall shape, 2) kinematic (upper) endpoint, 3) location of the peak, and 4) curvature near the peak. They enable us to measure the mass spectrum of the new particles including the DM candidate as well as differentiate the decay topology. We also showed that the relevant invariant mass distribution can be categorized by its endpoint, peak position and curvature. It turned out that typically they suffice for discriminating among the competing decay topologies. In each case, we enumerated the effective mass parameters which can be extracted in experiment. For some of the cases, the shape information of the invariant mass distribution is enough to determine the masses of new particles/DM, including the overall mass scale.

Stransverse mass/M_{T2}: In Chapter 3 we moved to the M_{T2} distribution as the second tool to identify the DM properties. For simplicity, we studied pair production of the same mother, followed by decays to SM particles and DM which involve only *off*-shell intermediate particles (i.e., which are heavier than their mother particle).

Clearly, in a Z_3 model, the events can be classified into three types depending on the total number of DM particles (i.e., two, three or four) vs. only two DM particles for Z_2 model. We showed that the edges of the M_{T2} distributions are different in these three types of events in a Z_3 model, again even if the same mother is produced (vs. only one edge for Z_2 model). This feature allowed us to distinguish Z_3 from Z_2 models. Moreover, we gave predictions for the values of the edges in the two new cases, namely, three and four DM in each event, as functions of the mother and the DM masses. Thus, we can extract the mother and DM masses *separately* using the measurements of these different edges for a Z_3 model. This achievement is especially noteworthy for the case of *single* visible particle in each decay chain since a similar measurement of the mother and DM masses is not possible in a Z_2 model, based solely on using the M_{T2} variable.

We emphasized that there are two subcases in the above analysis, namely, the visible particles in the decay chain with one DM being identical or different (respectively) to those in the decay chain with two DM (for Z_3 models). In the case of the visible particles not being identical, it is easy to separate the events of the three types mentioned above so that one can then plot the respective M_{T2} distributions. However, in the case of the visible particles being identical, one obviously has only a *single* M_{T2} distribution (i.e., combination of the above three types) to begin with. Therefore, we developed a new method to separate out the candidate events with three DM vs. two DM in this case, using the observation that the visible particles on the side with two DM will have smaller energy/momentum that the visible particles on the side with one DM in the same event. This feature is to be compared to

the visible energy/momentum being more "balanced" in the case of one DM on each side. We observed that the above imbalance in the energy/momentum on the two sides *by itself* provides a hint for the appearance of three DM in the event. However, combining it with edges in M_{T2} distributions provides a more powerful discriminator.

Energy peak: In Chapter 4 we turned our gear to the peak in the energy distribution of visible particle(s). We there proposed a new strategy to count the number of DM particles resulting from the decay of a single mother particle, which depends on the nature of the DM stabilization symmetries. To illustrate the technique, we compared a two-body decay of a mother particle into *one* DM and one visible particles with a three-body decay into *two* DM and one visible particles. The latter decay topology is present in Z_3 models but not in Z_2 models.

The technique begins with measuring the kinematic endpoint of the associated M_{T2} distribution (assuming the other decay side undergoes the same decay process), which will be used to be compared with the peak position in the energy distribution of the visible particle. The next theoretical observation is that the peak of the energy distribution of the visible particle in the laboratory frame is the same as the energy measured in the rest frame of the mother particle for the two-body decay, but is smaller than the maximum value in such rest frame energy for the three-body decay. The crux is that the rest frame energy that is used as a reference value in this comparison is precisely the parameter obtained in the above M_{T2} analysis. Combining the above two facts, we showed that the peak of observed energy of the

visible particle being smaller than (vs. same as) the reference value obtained from the M_{T2} endpoint provides evidence for two (vs. one) DM particles in the decay of a mother particle, and thus a Z_3 symmetry can be distinguished from Z_2.

Determining the DM properties by experiment is important to understand dark matter itself as well as dark matter phenomena, and thus provides rich subjects in research. Certainly, other kinematic variables/techniques deserve to be examined along the line of studying the DM properties, and moreover they may probe cases which were not covered by this series of research projects. We also plan to extend this program of study to other DM properties such as spin, coupling constants and so on.

Chapter A: The distribution for the new topology

Most of the intermediate steps in the derivation of the cusp in Eq. (2.25) are similar to the analysis in reference [57] of the reaction in Eq. (2.18), except for the fact that a DM (i.e., massive) particle is situated in-between two SM particles in the new topology (See Eq. (2.21)). Based on the algebra and the notations found in reference [57], we will derive a few useful relations.

Basically, the invariant mass formed by the two SM particles in this topology is given by

$$m_{ca}^2 = (p_c + p_a)^2 = 2E_c E_a(1 - \cos\theta_{ca}) \tag{A.1}$$

where θ_{ca} is the opening angle between two visible particles. Note that this relation is always valid in any frame so that we can rewrite the above relation as

$$m_{ca}^2 = 2E_c^{(B)} E_a^{(B)}(1 - \cos\theta_{ca}^{(B)}). \tag{A.2}$$

Here and henceforth the (particle) superscripts on θ's (in this case B) imply that those angles are measured in the rest frame of the corresponding particle. Using energy-momentum conservation, we can easily obtain the energies for a, DM, and c, which are measured in the rest frame of particle B.

$$E_a^{(B)} = \frac{m_B^2 - m_A^2}{2m_B} \tag{A.3}$$

$$E_{\rm DM}^{(B)} = \frac{m_C^2 - m_B^2 - m_{\rm DM}^2}{2m_B} \tag{A.4}$$

$$E_c^{(B)} = \frac{(m_D^2 - m_C^2)m_B}{m_B^2 + m_C^2 - m_{\rm DM}^2 - \lambda^{1/2}(m_C^2, m_B^2, m_{\rm DM}^2)\cos\theta_{c\,\rm DM}^{(B)}} \tag{A.5}$$

Inserting these relations into Eq. (A.2), we obtain

$$m_{ca}^2 = \frac{2(m_D^2 - m_C^2)m_B}{m_B^2 + m_C^2 - m_{\rm DM}^2 - \lambda^{1/2}(m_C^2, m_B^2, m_{\rm DM}^2)\cos\theta_{c\,\rm DM}^{(B)}} \cdot \frac{m_B^2 - m_A^2}{2m_B}(1 - \cos\theta_{ca}^{(B)}) \tag{A.6}$$

We easily see that the maximum of m_{ca}^2 occurs when $\cos\theta_{c\,\rm DM}^{(B)} = 1$ and $\cos\theta_{ca}^{(B)} = -1$. We want to express the invariant mass m_{ca} in terms of variables which have flat distributions: this is the case for $\cos\theta_{ca}^{(B)}$, but not for $\cos\theta_{c\,\rm DM}^{(B)}$. So, we need to express $\cos\theta_{c\,\rm DM}^{(B)}$ in terms of $\cos\theta_{c\,\rm DM}^{(C)}$ (i.e., the same angle in the rest frame of particle C) for which the distribution is also flat. This relation can be found by calculating $m_{c\,\rm DM}^2$ in the rest frames of particle C and B:

$$m_{c\,\rm DM}^2 = m_{\rm DM}^2 + 2E_c^{(C)}E_{\rm DM}^{(C)} - 2E_c^{(C)}\sqrt{(E_{\rm DM}^{(C)})^2 - m_{\rm DM}^2}\cos\theta_{c\,\rm DM}^{(C)} \tag{A.7}$$

$$= m_{\rm DM}^2 + 2E_c^{(B)}E_{\rm DM}^{(B)} - 2E_c^{(B)}\sqrt{(E_{\rm DM}^{(B)})^2 - m_{\rm DM}^2}\cos\theta_{c\,\rm DM}^{(B)} \tag{A.8}$$

Again, the energy-momentum conservation in the rest frame of C gives the following relations:

$$E_{\rm DM}^{(C)} = \frac{m_C^2 - m_B^2 + m_{\rm DM}^2}{2m_C} \tag{A.9}$$

$$E_c^{(C)} = \frac{m_D^2 - m_C^2}{2m_C} \tag{A.10}$$

Substitution of $E_{\rm DM}$ and E_c in the rest frame of C and B into Eq. (A.7) and Eq.

(A.8) gives the relation between $\cos\theta^{(B)}_{c\mathrm{DM}}$ and $\cos\theta^{(C)}_{c\mathrm{DM}}$:

$$\begin{aligned}\frac{2m_B^2}{m_C^2+m_B^2-m_{\mathrm{DM}}^2-\lambda^{1/2}(m_C^2,m_B^2,m_{\mathrm{DM}}^2)\cos\theta^{(B)}_{c\,\mathrm{DM}}} \\ = \quad 1-\frac{m_C^2-m_B^2+m_{\mathrm{DM}}^2-\lambda^{1/2}(m_C^2,m_B^2,m_{\mathrm{DM}}^2)\cos\theta^{(C)}_{c\,\mathrm{DM}}}{2m_C^2}\end{aligned} \tag{A.11}$$

Next, we introduce the variables u and v:

$$u \equiv \frac{1-\cos\theta^{(C)}_{c\,\mathrm{DM}}}{2}, \quad v \equiv \frac{1-\cos\theta^{(B)}_{ca}}{2} \tag{A.12}$$

and using Eq. (A.11), we express m_{ca}^2 in terms of u and v:

$$m_{ca}^2 = (m_{ca}^{\max})^2(1-\alpha u)v \tag{A.13}$$

where

$$(m_{ca}^{\max})^2 \quad = \quad \frac{2(m_D^2-m_C^2)(m_B^2-m_A^2)}{m_B^2+m_C^2-m_{\mathrm{DM}}^2-\lambda^{1/2}(m_C^2,m_B^2,m_{\mathrm{DM}}^2)}. \tag{A.14}$$

Note that the differential distributions for u and v ($0 \le u, v \le 1$) are also flat:

$$\frac{1}{\Gamma}\frac{\partial^2\Gamma}{\partial u\partial v} = \theta(u)\theta(1-u)\theta(v)\theta(1-v) \tag{A.15}$$

where $\theta(x)$ is the usual step function. Replacing u and v by u and m_{ca}^2 by using Eq. (A.13) gives the differential distribution

$$\frac{1}{\Gamma}\frac{\partial^2\Gamma}{\partial u\partial m_{ca}^2} = \hat{\theta}\left(\frac{m_{ca}^2}{(m_{ca}^{\max})^2(1-\alpha u)}\right)\frac{\hat{\theta}(u)}{(m_{ca}^{\max})^2(1-\alpha u)} \tag{A.16}$$

where a "top-hat" function $\hat{\theta}(x) \equiv \theta(x)\theta(1-x)$. The next step is to integrate over u to find the distribution in m_{ca}^2:

$$\begin{aligned}\frac{1}{\Gamma}\frac{\partial^2\Gamma}{\partial m_{ca}^2} &= \int_{-\infty}^{\infty}\frac{1}{\Gamma}\frac{\partial^2\Gamma}{\partial u\partial m_{ca}^2}du \\ &= \int_0^1 \hat{\theta}\left(\frac{m_{ca}^2}{(m_{ca}^{\max})^2(1-\alpha u)}\right)\frac{1}{(m_{ca}^{\max})^2(1-\alpha u)}du \\ &= \int_0^{u_{\max}}\frac{1}{(m_{ca}^{\max})^2(1-\alpha u)}du\end{aligned} \tag{A.17}$$

for $0 \leq m_{ca} \leq m_{ca}^{\max}$, where

$$u_{\max} = \max\left(1,\ \frac{1}{\alpha}\left[1 - \frac{m_{ca}^2}{(m_{ca}^{\max})^2}\right]\right). \tag{A.18}$$

Now the above integral is easy to evaluate, and we finally obtain the distribution which was given earlier in Eq. (2.25):

$$\frac{1}{\Gamma}\frac{\partial^2\Gamma}{\partial m_{ca}^2} = \begin{cases} \frac{1}{(m_{ca}^{\max})^2\alpha}\ln\frac{m_C^2}{m_B^2} & \text{for} \quad 0 < m_{ca} < \sqrt{1-\alpha}\, m_{ca}^{\max} \\ \\ \frac{1}{(m_{ca}^{\max})^2\alpha}\ln\frac{(m_{ca}^{\max})^2}{m_{ca}^2} & \text{for} \quad \sqrt{1-\alpha}\, m_{ca}^{\max} < m_{ca} < m_{ca}^{\max}. \end{cases} \tag{A.19}$$

Chapter B: The location of $M_{T2}^{\max}$

In this Chapter we will derive the analytic expression for the location of the upper edge in the M_{T2} distribution. We begin with deriving the general expression of the M_{T2} solution for a given set of kinematic configuration, then move on to obtaining the maxima of the balanced/unbalanced M_{T2} solutions, and close with giving the global maximum of the M_{T2} distribution, followed by a simple application.

B.0.1 The general expression for the M_{T2} solution

The usual M_{T2} variable [4] is defined as a generalized transverse mass such that each of pair-produced mother particles decays into visible particles and one dark matter particle of the same type. However, we do not restrict ourselves to such cases, i.e., we extend our consideration to the cases with more than two DM in a full decay chain (e.g., E_3 and E_4 type events in Z_3 models). Nevertheless, in the analysis of M_{T2} variable, we still *hypothesize* that two dark matter particles with equal mass (i.e., one DM per chain) are involved in the full decay process, i.e., we employ the "naive" M_{T2} method (as mentioned at the beginning of section 3.3).

The left diagram of Figure B.1 illustrates the decay process of pair-produced mother particles that we are taking into consideration. Here the "blob" denotes off-

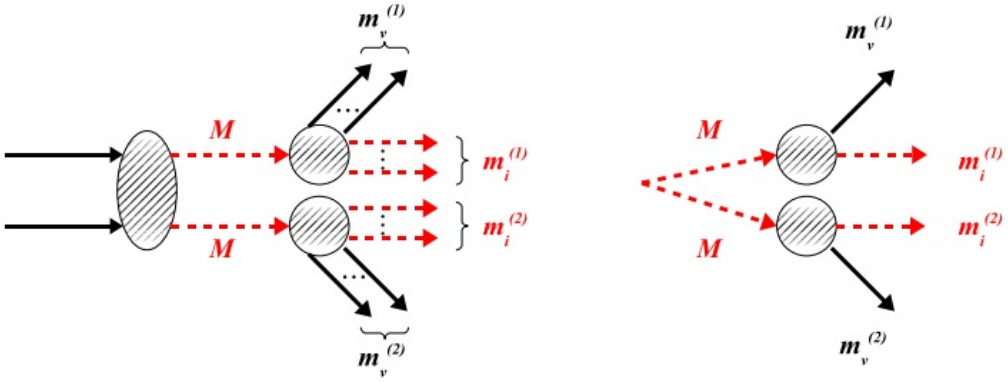

Figure B.1: The left panel illustrates the decay process of interest which pair-produced mother particles go through. M, $m_v^{(a)}$, and $m_i^{(a)}$ $(a = 1,\ 2)$ denote the mass of mother particle, total invariant masses of visible particles and invisible particles in the same decay chain, respectively. The right panel illustrates the effective configuration of such a decay process.

shell intermediate particles or an (on-shell) point interaction. The red dashed lines represent any particles charged under dark matter stabilization symmetry whereas the black solid lines represent any visible/SM particles. M is the mass of the mother particle, which must be charged under DM stabilization symmetry. As mentioned above, each mother particle can decay into the multiple number of invisible/DM particles as well as the multiple number of visible/SM particles, and this extended possibility is explicitly depicted by the multiple number of red dashed and black solid arrows behind the two small blobs. Each visible/invisible multi-particle state can be collapsed effectively to a(n) visible/invisible single particle state by introducing invariant (transverse) mass, which will be manifest in the detailed formulae later. In this sense, $m_v^{(a)}$ and $m_i^{(a)}$ can be understood as the total invariant masses formed by visible or invisible particles belonging to the same decay chain.

For defining the M_{T2} variable one should be noted that we are not aware of the DM mass in advance. Hence, the best we can do is to introduce trial DM mass. Since we perform the naive M_{T2} analysis as mentioned above, i.e., we assume a single type of DM in each decay chain even if the actual physics could be different, we employ only one type of trial DM mass $\tilde{m}$ and construct the M_{T2} variable as follows [4]:

$$M_{T2}\left(\mathbf{p}_T^{v(1)}, m_T^{v(1)}, \mathbf{p}_T^{v(2)}, m_T^{v(2)}; \tilde{m}\right) \equiv \min_{\mathbf{p}_T^{v(1)}+\mathbf{p}_T^{v(2)}+\tilde{\mathbf{p}}_T^{(1)}+\tilde{\mathbf{p}}_T^{(2)}=0} \left[\max\left\{M_T^{(1)}, M_T^{(2)}\right\}\right] \quad \text{(B.1)}$$

Here each transverse mass of the decay product $M_T^{(a)}$ $(a = 1, 2)$ is given by

$$\left(M_T^{(a)}\right)^2 = \left(m_T^{v(a)}\right)^2 + \tilde{m}^2 + 2\left(E_T^{v(a)}\tilde{E}_T^{(a)} - \mathbf{p}_T^{v(a)} \cdot \tilde{\mathbf{p}}_T^{(a)}\right) \quad \text{(B.2)}$$

where $m_T^{v(a)}$, $\mathbf{p}_T^{v(a)}$, and $E_T^{v(a)}$ are the total transverse invariant mass, transverse momentum, and transverse energy of visible particles:

$$\begin{aligned}
\left(m_T^{v(a)}\right)^2 &= \left(t_1^{v(a)} + \cdots + t_n^{v(a)}\right)^2 \\
&= \sum_\alpha \left(m_\alpha^{v(a)}\right)^2 + 2\sum_{\alpha>\beta}\left(E_{\alpha T}^{v(a)} E_{\beta T}^{v(a)} - \mathbf{p}_{\alpha T}^{v(a)} \cdot \mathbf{p}_{\beta T}^{v(a)}\right) \quad \text{(B.3)} \\
\mathbf{p}_T^{v(a)} &= \sum_\alpha \mathbf{p}_{\alpha T}^{v(a)} \quad \text{(B.4)} \\
E_T^{v(a)} &= \sum_\alpha E_{\alpha T}^{v(a)}, \quad \text{(B.5)}
\end{aligned}$$

and $\tilde{\mathbf{p}}_T^{(a)}$ and $\tilde{E}_T^{(a)}$ are the transverse momentum and energy of the (assumed-to-be-one) *trial* DM particle in each decay chain. Here $m_\alpha^{v(a)}$ indicates the mass of αth visible particle in ath decay chain $(a = 1,\ 2)$ and $t_l^{v(a)}$ indicates the (1+2) momentum on the transverse plane which is defined as

$$t_l^{v(a)} \equiv \left(E_{lT}^{v(a)}, \mathbf{p}_{lT}^{v(a)}\right) = \left(\sqrt{\left(\mathbf{p}_{lT}^{v(a)}\right)^2 + \left(m_l^{v(a)}\right)^2}, \mathbf{p}_{lT}^{v(a)}\right), \quad \text{(B.6)}$$

and the metric for this type of momentum is $\mathrm{diag}(1,-1,-1)$. There arise two noteworthy things:

- As far as the range is concerned, the transverse and the regular invariant masses have the same lower and upper limits. Moreover, since the M_{T2} solutions of interest arise at either of the two limits, one may consider the M_{T2} where $m_T^{v(a)}$ are replaced by the regular invariant masses of visible particles $m_v^{(a)}$:

$$\begin{aligned}\left(m_v^{(a)}\right)^2 &= \left(p_1^{v(a)} + \cdots + p_n^{v(a)}\right)^2 \\ &= \sum_\alpha \left(m_\alpha^{v(a)}\right)^2 + 2\sum_{\alpha>\beta}\left(E_\alpha^{v(a)}E_\beta^{v(a)} - \mathbf{p}_\alpha^{v(a)}\cdot\mathbf{p}_\beta^{v(a)}\right). \end{aligned} \quad \text{(B.7)}$$

- As advertised earlier, the entire visible states in the same decay chain can be understood effectively as a single visible particle whose "effective" mass is given by $m_v^{(a)}$. On the other hand, the corresponding "effective" quantity for invisible particles $m_i^{(a)}$ does not seem to be contained in the M_{T2} variable. In fact, the M_{T2} variable depends *implicitly* on $m_i^{(a)}$, which will be cleared shortly.

From these two observations we can reduce the decay of pair-produced mother particles into two multi-particle states (left panel of Figure B.1) to an effective kinematic configuration where there exist two simple 2-body decay chains shown in the right panel of Figure B.1.

For such M_{T2}, there are two types of solution which are called the "balanced" M_{T2} solution and the "unbalanced" M_{T2} solution, and the fact that there always exist some events to give such solutions was proven [4, 7]. The balanced solution arises

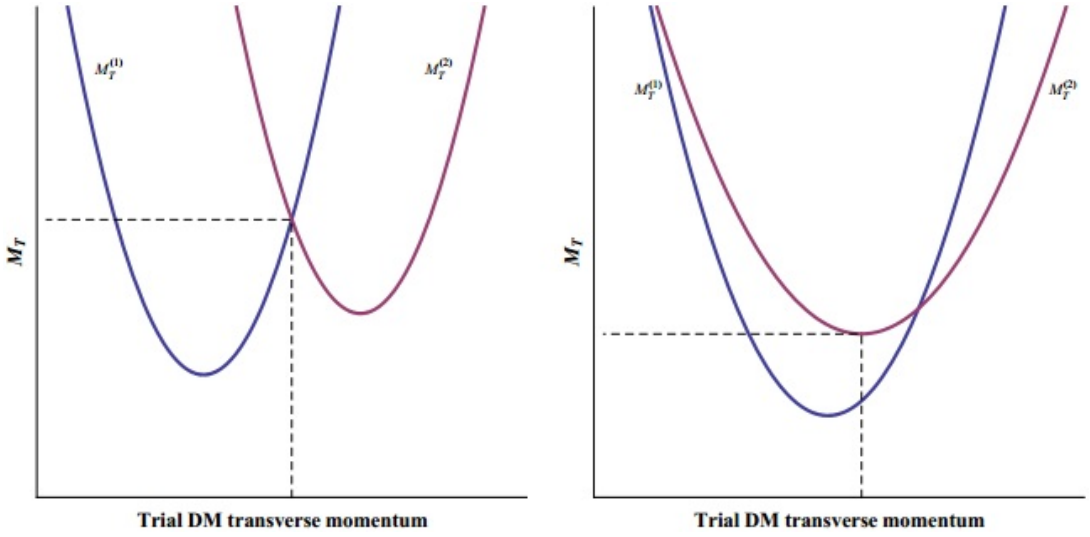

Figure B.2: Graphical configurations to give rise to a balanced M_{T2} solution (the left panel) and an unbalanced M_{T2} solution (the right panel). The dashed line indicates the solution for the M_{T2} variable to take.

when $M_T^{(a)} \geq M_T^{(b)}$ for both $a(= 1,\ 2)$ with the trial DM momentum having the value to accommodate $M_T^{(b)}$ $(b \neq a)$ at their global (or so-called "unconstrained") minimum which will be defined shortly (see the left panel of Figure B.2), and otherwise, the unbalanced solution arises (see the right panel of Figure B.2).[1] The global minima for $M_T^{(1)}$ and $M_T^{(2)}$ are easily evaluated by differentiating Eq. (B.2) with

[1]If the total invariant masses of visible states in both decay chains are the same, only the balanced solutions arise. The reason is because the unconstrained minima for both M_T are identical, there is no possibility that the kinematic configuration like the right panel of Figure B.2 is made. As an example, if there exists only one massless visible particle in each decay chain, the M_{T2} values are always given by the balanced solution.

respect to the trial DM momentum and finding the stationary point [4]:

$$\left(M_T^{(1)}\right)_{\min} = m_v^{(1)} + \tilde{m} \tag{B.8}$$

$$\left(M_T^{(2)}\right)_{\min} = m_v^{(2)} + \tilde{m} \tag{B.9}$$

The balanced and the unbalanced M_{T2} solutions for a given set of the "effective" visible and invisible masses which are shown in the right panel of Figure B.1 are as follows [4, 7]:

$$\left(M_{T2}^{bal}\right)^2 = \tilde{m}^2 + A + \sqrt{\left(1 + \frac{4\tilde{m}^2}{2A - \left(m_v^{(1)}\right)^2 - \left(m_v^{(2)}\right)^2}\right)\left(A^2 - \left(m_v^{(1)} m_v^{(2)}\right)^2\right)} \tag{B.10}$$

$$M_{T2}^{unbal} = \tilde{m} + m_v^{(a)} \quad (a = 1,\ 2) \tag{B.11}$$

for

$$A = E_T^{v(1)} E_T^{v(2)} + \vec{\mathbf{p}}_T^{v(1)} \cdot \vec{\mathbf{p}}_T^{v(2)}. \tag{B.12}$$

Note that the unbalanced solution is simply given by the unconstrained minimum of $M_T^{(a)}$, and for a fixed set of visible and invisible masses the balanced solution is bounded above at

$$A = E^{v(1)} E^{v(2)} + q^{v(1)} q^{v(2)}. \tag{B.13}$$

In fact, if we take an adequate number of events, we can always find some event which corresponds to such an upper bound [7]. Since we are interested in the M_{T2}^{bal} equal to its own upper bound, we henceforth assume that A is understood as Eq. (B.13) unless there arises any confusion. Here $\left(E^{v(a)}\right)^2 = \left(q^{v(a)}\right)^2 + \left(m_v^{(a)}\right)^2$ and $q^{v(a)}$ is

the magnitude of the total momentum of visible particles seen in the rest frame of their mother particle. The explicit expression for $q^{v(a)}$ can be easily determined in terms of the masses of mother, visible, and invisible particles as follows:

$$q_v^{(a)} = \frac{1}{2M}\sqrt{\left\{\left(M+m_v^{(a)}\right)^2-\left(m_i^{(a)}\right)^2\right\}\left\{\left(M-m_v^{(a)}\right)^2-\left(m_i^{(a)}\right)^2\right\}}. \quad \text{(B.14)}$$

One thing to be emphasized is that the dependence of the M_{T2} variable on the effective invisible/DM mass $m_i^{(a)}$ first appear in $q_v^{(a)}$. In other words, M_{T2} is an implicit function of $m_i^{(a)}$ via $q_v^{(a)}$ as mentioned before. Furthermore, we include the possibility that multiple (massive) invisible particles are emitted in each decay chain unlike the previous studies (which considered the cases with two invisible particles having non-identical masses). Hence $m_i^{(a)}$ as well as $m_v^{(a)}$ have their own range once multiple visible and invisible particles are involved in the given decay process. For off-shell intermediate particles the respective ranges are given by (See, for example, [56])

$$\sum_\alpha m_\alpha^{v(a)} = m_{v,\,\min}^{(a)} \le m_v^{(a)} \le m_{v,\,\max}^{(a)} = M - \sum_\beta m_\beta^{i(a)} \quad \text{(B.15)}$$

$$\sum_\beta m_\beta^{i(a)} = m_{i,\,\min}^{(a)} \le m_i^{(a)} \le m_{i,\,\max}^{(a)} = M - \sum_\alpha m_\alpha^{v(a)}. \quad \text{(B.16)}$$

The lower limit corresponds to the situation in which particles described by $p_\alpha^{v(a)}\left(p_\beta^{i(a)}\right)$ are at rest in their center of mass frame so that they move with the same velocity in any frame. The upper limit corresponds to the situation in which particles described by $p_\beta^{i(a)}\left(p_\alpha^{v(a)}\right)$ are at rest in the overall center of mass frame of the final state described by $p_\alpha^{v(a)}$ and $p_\beta^{i(a)}$.

B.0.2 The maximum balanced and unbalanced M_{T2} solutions

For the decay with visible/invisible multi-particle final states, it is obvious that balanced/unbalanced M_{T2} solutions have their own range due to the existence of the range in either $m_v^{(a)}$ or $m_i^{(a)}$ or both of them. As far as the upper edge in the M_{T2} distribution is concerned, either the maximum balanced or the maximum unbalanced solution appears as the global maximum. For the unbalanced solution, one can easily derive the following relationship from Eqs. (B.11) and (B.15).

$$M_{T2}^{\max,unbal} = \tilde{m} + \max\left[m_{v,\max}^{(1)},\ m_{v,\max}^{(2)}\right] \tag{B.17}$$

For the balanced solution, however, it is not easily seen which values of $m_v^{(a)}$ and $m_i^{(a)}$ $(a = 1,\ 2)$ will form the maximum balanced solution because of the complication in the corresponding expression $\left(M_{T2}^{bal}\right)^2$ given in Eq. (B.10). In order to identify those values, we are required to carefully investigate the functional behavior of $\left(M_{T2}^{bal}\right)^2$ according to the changes in $m_i^{(a)}$ and $m_v^{(a)}$, which will be considered in order.

B.0.2.1 The change in $m_i^{(a)}$

To see the dependence of $\left(M_{T2}^{bal}\right)^2$ on $m_i^{(1)}$, we simply take the partial derivative:

$$\frac{\partial\left(M_{T2}^{bal}\right)^2}{\partial\left(m_i^{(1)}\right)^2} = \frac{D}{2X\sqrt{B^3C}} \tag{B.18}$$

where

$$B \equiv 2A - \left(m_v^{(1)}\right)^2 - \left(m_v^{(2)}\right)^2,\ C \equiv A^2 - \left(m_v^{(1)}\right)^2\left(m_v^{(2)}\right)^2,\ X \equiv \sqrt{B + 4\tilde{m}^2} \tag{B.19}$$

$$D \equiv (BC' - B'C)X^2 + 2A'\sqrt{B^3C}X + B'BC \tag{B.20}$$

with the following notations:

$$A' \equiv \frac{\partial A}{\partial \left(m_i^{(1)}\right)^2}, \quad B' \equiv \frac{\partial B}{\partial \left(m_i^{(1)}\right)^2} = 2A', \quad C' \equiv \frac{\partial C}{\partial \left(m_i^{(1)}\right)^2} = 2AA'. \tag{B.21}$$

One can easily see that A, B, and C are always positive for any set of $m_v^{(a)}$ and $m_i^{(a)}$, and that only positive X is allowed by construction. Also, one can easily prove that A' is negative.

The solutions to $D = 0$ are given as follows:

$$X_1 = -\frac{\sqrt{BC}}{A - \left(m_v^{(1)}\right)^2} \tag{B.22}$$

$$X_2 = -\frac{\sqrt{BC}}{A - \left(m_v^{(2)}\right)^2}. \tag{B.23}$$

For $m_v^{(1)} \neq m_v^{(2)}$ it can be proven that either $A - \left(m_v^{(1)}\right)^2$ or $A - \left(m_v^{(2)}\right)^2$ must be positive and the other is positive or negative depending on the parameter space formed by $m_v^{(1)}$ and $m_v^{(2)}$ [7]. Hence, one of the two solutions given above must be negative, which is unphysical, the other is either physically allowed or not. Actually, it turns out that the signs of $A - \left(m_v^{(1)}\right)^2$ and $A - \left(m_v^{(2)}\right)^2$ are connected to the coefficient of X^2 in D in the following way:

$$BC' - B'C = 2A' \left(A - \left(m_v^{(1)}\right)^2\right) \left(A - \left(m_v^{(2)}\right)^2\right). \tag{B.24}$$

Let us assume that $m_v^{(1)}$ is larger than $m_v^{(2)}$. In this case, $A - \left(m_v^{(2)}\right)^2$ is always positive, i.e., X_2 is always unphysical. Since $A' < 0$ as mentioned above, if $A - \left(m_v^{(1)}\right)^2$ is positive as well, then D, which is a quadratic function in X, becomes a parabola bounded above, and the two solutions X_1 and X_2 all are negative, i.e., unphysical. Therefore, $D < 0$ for arbitrary (physically-allowed) X or $\tilde{m}$. On the

other hand, if $A-\left(m_v^{(1)}\right)^2$ is negative, then D turns into a parabola bounded below, and X_1 becomes a physically allowed solution. Therefore, $D<0$ for $0<X<X_1$ and $D>0$ for $X>X_1$. However, in [7] it was shown that X_1 gives rise to

$$M_{T2}^{bal}(X=X_1)=\tilde{m}+m_v^{(1)}, \tag{B.25}$$

which is simply the unbalanced solution for $m_v^{(1)}>m_v^{(2)}$. Moreover, they showed that this implies that X_1 corresponds to the boundary between the balanced domain and the unbalanced domain. In other words, with X being larger than X_1 the balanced solution is reduced to the unbalanced solution. One can make the same argument and lead the same conclusion for the opposite configuration, i.e., $m_v^{(1)}<m_v^{(2)}$. Also, the dependence on $m_i^{(2)}$ can be easily checked by following similar arguments. Based on hitherto observations, we have

$$\frac{\partial\left(M_{T2}^{bal}\right)^2}{\partial\left(m_i^{(a)}\right)^2} < 0 \tag{B.26}$$

$$M_{T2}^{\max,bal} = M_{T2}^{bal}\left(m_i^{(1)}=m_{i,\min}^{(1)},\ m_i^{(2)}=m_{i,\min}^{(2)}\right) \tag{B.27}$$

for any set of $m_v^{(a)}$ $(a=1,\ 2)$.

B.0.2.2 The change in $m_v^{(a)}$

The early work on the dependence of $\left(M_{T2}^{bal}\right)^2$ on $m_v^{(a)}$ was made in [7]. Here we simply provide the final results and mention some modification from the original

expression.

$$\frac{\partial \left(M_{T2}^{bal}\right)^2}{\partial \left(m_v^{(a)}\right)^2} \quad \begin{cases} \leq 0 & \text{for } \tilde{m} < m' \\ \\ \geq 0 & \text{for } \tilde{m} \geq m' \end{cases} \tag{B.28}$$

$$M_{T2}^{\max,bal} = \begin{cases} M_{T2}^{bal}\left(m_v^{(1)} = m_{v,\min}^{(1)},\ m_v^{(2)} = m_{v,\min}^{(2)}\right) \text{ for } \tilde{m} < m' \\ \\ M_{T2}^{bal}\left(m_v^{(1)} = m_{v,\max}^{(1)},\ m_v^{(2)} = m_{v,\max}^{(2)}\right) \text{ for } \tilde{m} \geq m'. \end{cases} \tag{B.29}$$

Here the "kink" location m' can be identified as the true dark matter mass m_{DM} if only a single type of DM is involved [7]. However, in general, it differs from m_{DM} because we do not restrict our consideration to the case with one single-typed DM emitted in each decay chain. Therefore, its expression is written in terms of all parameters (i.e., M, $m_v^{(a)}$, and $m_i^{(a)}$), and it can be calculated by solving the following equation [7]:

$$\sqrt{B + 4m'^2} = \frac{\sqrt{BC}(1 - 2\bar{A})}{2\bar{A}\left(A - (m_v^>)^2\right) + A - (m_v^<)^2} \tag{B.30}$$

where $m_v^>$ and $m_v^<$ denote the heavier and the lighter (invariant) visible masses between the two decay sides, respectively, and $\bar{A}$ is defined as

$$\bar{A} = \frac{\partial A}{\partial (m_v^>)^2}. \tag{B.31}$$

B.0.3 Discussions and application

It is a well-known fact that there arises a "kink" in the $M_{T2}^{\max}$ as a function of the trial mass once there exist more than one visible particle in each decay chain

and its location is at $\tilde{m} = m_{DM}$ for the cases with a single identical DM particle per decay chain. For more extended case, i.e., $m_i^{(1)} \neq m_i^{(2)}$, one can simply solve Eq. (B.30). In turns out, however, that this is not the only way of obtaining the kink location. An alternative and simpler way is to find the intersecting point between the maximum balanced and unbalanced solutions. In other words, the solution to satisfy Eq. (B.30) also satisfies the relation $M_{T2}^{\max,bal} = M_{T2}^{\max,unbal}$. For simplicity, let us assume that $m_{v,\max}^{(1)} > m_{v,\max}^{(2)}$. We then have

$$\left(M_{T2}^{\max,unbal}\right)^2 = \left(\tilde{m} + m_{v,\max}^{(1)}\right)^2 \tag{B.32}$$

and

$$\left(M_{T2}^{\max,bal}\right)^2 = \tilde{m}^2 + A + \sqrt{\frac{C}{B}\left(B + 4\tilde{m}^2\right)} \tag{B.33}$$

where A is evaluated at $m_i^{(a)} = m_{i,\min}^{(a)}$ as discussed before. Letting Eqs. (B.32) and (B.33) be equated and doing some tedious algebra, one can end up with

$$A^2 = \left(m_v^{(1)}\right)^2 \left(m_v^{(2)}\right)^2, \tag{B.34}$$

which is valid only with $m_v^{(a)}$ being their maximum. Note that $M_{T2}^{\max,bal}$ at $\tilde{m} = m'$ arises when $m_v^{(a)} = m_{v,\max}^{(a)}$ from Eq. (B.29). Hence, the above-given relationship holds, and the location of the kink can be evaluated by finding the intersection between the maximum balanced and unbalanced solutions.

This observation, actually, leads us to the expressions for $M_{T2}^{\max,bal}$ and $M_{T2}^{\max,unbal}$. Note that it was proven that the balanced solution contributes to the upper edge of the M_{T2} distribution at $\tilde{m} < m'$ in [7]. Also, it is straightforward to prove that the maximum unbalanced solution is larger than the maximum balanced solution

at $\tilde{m} \geq m'$. Therefore, as long as the values to give the upper edge of the M_{T2} distribution are concerned, it can be (effectively) understood that the maximum balanced solutions occur at $m_v^{(a)} = m_{v,\min}^{(a)}$ and $m_i^{(a)} = m_{i,\min}^{(a)}$ and the maximum unbalanced solutions do at the maximum of the two $m_{v,\max}^{(a)}$ ($a = 1,\ 2$) for any $\tilde{m}$. As an example, if all visible particles are assumed massless, the maximum balanced and unbalanced solutions are given as follows:

$$\begin{aligned} M_{T2}^{\max,bal} &= \sqrt{\frac{\left(M^2 - m_{i,\min}^{(1)2}\right)\left(M^2 - m_{i,\min}^{(2)2}\right)}{4M^2}} \\ &+ \sqrt{\frac{\left(M^2 - m_{i,\min}^{(1)2}\right)\left(M^2 - m_{i,\min}^{(2)2}\right)}{4M^2} + \tilde{m}^2} \end{aligned} \tag{B.35}$$

$$M_{T2}^{\max,unbal} = \tilde{m} + \max\left[m_{v,\max}^{(1)},\ m_{v,\max}^{(2)}\right] = \tilde{m} + M - \min\left[m_{i,\min}^{(1)},\ m_{i,\min}^{(2)}\right] \tag{B.36}$$

Obviously, the upper edge in the M_{T2} distribution is determined by the maximum value among many events for a given trial DM mass.

$$M_{T2}^{\max}(\tilde{m}) = \max_{\text{many events}}[M_{T2}(\tilde{m})] \tag{B.37}$$

Based on the above-discussed understanding, one could expect that taking the maximum between $M_{T2}^{\max,bal}$ and $M_{T2}^{\max,unbal}$ will result in the same value as the above-given Eq. (B.37).

$$M_{T2}^{\max} = \max\left[M_{T2}^{\max,bal},\ M_{T2}^{\max,unbal}\right] \tag{B.38}$$

It turns out, however, it is true only for the case where there exist more than one visible particle on each decay chain. In the case where there is only one visible particle per decay chain, one can prove that the maximum unbalanced solution is

less than the maximum balanced solution for any $\tilde{m}$ so that the $M_{T2}^{\max}$ is simply governed by the $M_{T2}^{\max,bal}\left(m_i^{(a)} = m_{i,\min}^{(a)}\right)$.

Chapter C: The existence of a kink in $M_{T2}^{\max}$ versus $\tilde{m}$

As discussed in Chapter B, it is obvious that for the cases where there is only a single visible particle in each decay chain, the $M_{T2}^{\max}$ as a function of the trial DM mass behaves like a smoothly increasing curve because the upper edge is solely governed by the "balanced" solution in Eq. (B.10). However, if there exist more than one visible particle per decay chain, the competition between the "balanced" and the "unbalanced" solutions, which is explicitly given in Eq. (B.38), gives rise to the possibility of a kink (i.e., no longer smooth) in the plot of $M_{T2}^{\max}$ versus $\tilde{m}$. In fact, this approach, the competition between the two types of solutions, enables us to examine easily whether or not there exists a "kink" on the function of the location of $M_{T2}^{\max}$.

In order to have a kink in $M_{T2}^{\max}$ as a function of $\tilde{m}$, the two functions of the maximum balanced and unbalanced solutions over the trial DM mass, i.e., $M_{T2}^{\max,bal}(\tilde{m})$ and $M_{T2}^{\max,unbal}(\tilde{m})$, must cross each other. From Eqs. (B.10) and (B.11) they are monotonic functions in $\tilde{m}$, and the slope of Eq. (B.10) is not greater than that of Eq. (B.11)(= 1) over the entire range. These two observations tell us that once a cross-over is made, no additional cross-overs are made. Therefore, it is sufficient to check whether or not the relative sizes of their corresponding functional

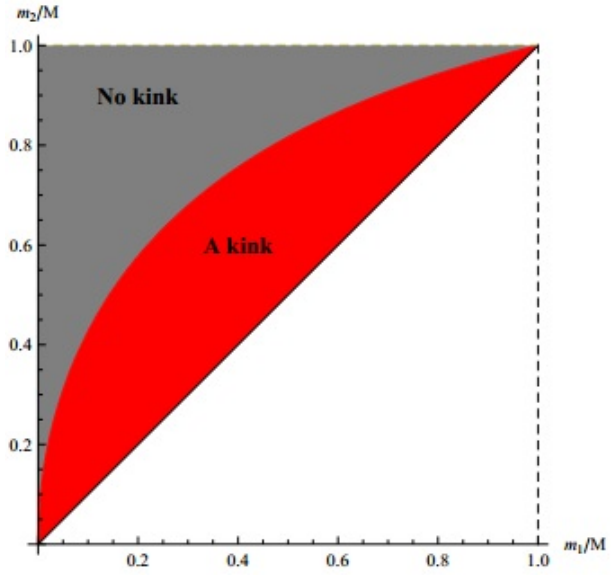

Figure C.1: The kinematic regions to have kink or no kink in the graph of $\frac{m_2}{M}$ versus $\frac{m_1}{M}$.

values at $\tilde{m} = 0$ and $\tilde{m} \to \infty$ are flipped for ensuring such a cross-over. Let us assume that the visible particles are massless for simplicity.[1] From Eqs. (B.35) and (B.36) one can easily prove that $M_{T2}^{\max,unbal}$ is larger than $M_{T2}^{\max,bal}$ at $\tilde{m} \to \infty$, and thus $M_{T2}^{\max,bal}$ should be larger than $M_{T2}^{\max,unbal}$ at $\tilde{m} = 0$ to obtain a kink. Their functional values at $\tilde{m} = 0$ are expressed as follows:

$$M_{T2}^{\max,bal}(\tilde{m}=0) = \sqrt{\frac{(M^2 - m_1^2)(M^2 - m_2^2)}{M^2}} \tag{C.1}$$

$$M_{T2}^{\max,unbal}(\tilde{m}=0) = M - m_1 \tag{C.2}$$

where $m_{i,\min}^{(1)} \equiv m_1$ and $m_{i,\min}^{(2)} \equiv m_2$, and we assumed $m_1 < m_2$ without loss of generality. Therefore, the condition to have a kink is simply

$$\sqrt{\left(1 - \frac{m_1^2}{M^2}\right)\left(1 - \frac{m_2^2}{M^2}\right)} > 1 - \frac{m_1}{M}, \tag{C.3}$$

[1] One can easily apply the same argument for the case of massive visible particles.

which can be further simplified to

$$\frac{m_1}{M} < \frac{m_2}{M} < \sqrt{\frac{2m_1}{M+m_1}}. \tag{C.4}$$

Likewise, one can easily find the condition to have no kink as follows:

$$\frac{m_2}{M} > \sqrt{\frac{2m_1}{M+m_1}}. \tag{C.5}$$

Figure C.1 shows the regions for kink or no kink pictorially; the red area represents all possible kinematic configurations for the existence of a kink while the gray one all possible kinematic configurations for no kink. Elsewhere is not physically allowed due to the assumption that $m_1 < m_2$.

There is a special case where each decay chain emits only one *single*-typed DM particle, i.e., $m_1 = m_2$. The Z_2 models or the E_2 type events of Z_3 models belong to this case. The range to satisfy Eq. (C.5), i.e., the condition to have no kink, is $\frac{m_1}{M} > 1$ or $\frac{m_1}{M} < -2$ both of which are not physically allowed. Therefore, we always obtain a kink in $M_{T2}^{\max}$ as a function of the trial DM mass as expected [7].

As another concrete example, let us take E_3 type events of Z_3 models, where one of the two decay chains emits a single dark matter particle whereas the other one emits two dark matter particles with intermediate particles *off*-shell. Like before, we assume that all DM particles to be emitted in the full decay process have the same mass so that the *minimum* of the effective dark matter mass of the two DM side to give the maximum balanced solution is $m_{DM}^{eff} = 2m_{DM}$, i.e., $m_1 = m_{DM}$ and $m_2 = 2m_{DM}$. From Eqs. (C.4) and (C.5) the conditions to have kink or no kink

become

$$\text{A kink:} \qquad 0 < \frac{m_{DM}}{M} < \frac{\sqrt{3}-1}{2} \tag{C.6}$$

$$\text{No kink:} \qquad \frac{\sqrt{3}-1}{2} < \frac{m_{DM}}{M} < 1, \tag{C.7}$$

which was mentioned in section 3.3.2 and demonstrated in Figure 3.4.

Chapter D: Algorithm to find the upper edge of M_{T2} distribution

In this Chapter, we describe an algorithm to identify the $M_{T2}^{\max}$ for events after the R_{P_t} cut. As we discussed in section 3.5.1.1, in Z_3 models where there is only one visible particle per decay chain, and the visible particles in the decay chains with one DM and two DM are identical, the total M_{T2} distribution becomes a combination of the distributions of E_2 and E_3 events. So the idea is to apply an R_{P_t} cut (a cut on the ratio of P_t's of visible particles on the two decay chains in the same event) to "remove" the E_2 events. This in principle can give us a relatively pure sample of E_3 events, which has a smaller $M_{T2}^{\max}$. But in practice/reality, there is still a small number of E_2 events that survive the R_{P_t} cut. Therefore, the upper edge of M_{T2} distribution for events after the R_{P_t} cut is hard to be determined due to the "contamination" of E_2 type events. This is shown in the right panel of Figure 3.8, which shows clearly that there are small number of events which has M_{T2} beyond the $M_{T2}^{\max}$ of E_3 type events. Here we propose an algorithm to identify/extract the "would-be" $M_{T2}^{\max}$ for E_3 events by removing E_2 contamination events and then do a fitting to the resulting distribution.

First, we need to "subtract" the contaminating events. To do this, we calculate the moving average of the number of events per bin including the last n bins in the

M_{T2} distribution: A_n. The choice of moving average makes this quantity rather stable under statistical fluctuations as we increase n. However, as we increase n to the point below $M_{T2}^{\max}$ for E_3 type events, we start to get a sharp rise on A_n. Based on this, we define $n_{\max}$ to be the bin such that $A_{n_{\max}+1} \geq 2.5 A_{n_{\max}}$. This bin is considered as a rough separation point between "contaminating" E_2 type events and the start of E_3 type events. And we treat $A_{n_{\max}}$ as a rough estimate for the E_2 type events contribution to the number of events per bin.

Next, we pick events with $n > n_{\max}$ and subtract $A_{n_{\max}}$ from the number of events in each bin. This gives us an approximate M_{T2} distribution for pure E_3 type events. Since we do not have an analytical formula for the M_{T2} distribution for E_3 type events, we can only do a fitting for events near and to the left of the bin $n_{\max}$ to find the upper edge of the M_{T2} distribution. We choose two fitting functions, one linear function and one quadratic function, and did the fitting separately. Our final answer for the $M_{T2}^{\max}$ is given by the average of the values obtained by these two fitting methods, and their difference is regarded as the error due to fitting.

Bibliography

[1] See, for example, G. Bertone, D. Hooper and J. Silk, "Particle dark matter: Evidence, candidates and constraints," Phys. Rept. **405**, 279 (2005) [arXiv:hep-ph/0404175].

[2] G. Hinshaw *et al.* [WMAP Collaboration], "Five-Year Wilkinson Microwave Anisotropy Probe (WMAP) Observations:Data Processing, Sky Maps, & Basic Results," arXiv:0803.0732 [astro-ph].

[3] D. G. E. Walker, "Dark Matter Stabilization Symmetries and Long-Lived Particles at the Large Hadron Collider," arXiv:0907.3142 [hep-ph].

[4] C. G. Lester and D. J. Summers, "Measuring masses of semiinvisibly decaying particles pair produced at hadron colliders," Phys. Lett. B **463**, 99 (1999) [arXiv:hep-ph/9906349];

[5] A. J. Barr, C. G. Lester, M. A. Parker, B. C. Allanach and P. Richardson, "Discovering anomaly-mediated supersymmetry at the LHC," JHEP **0303**, 045 (2003) [arXiv:hep-ph/0208214];

[6] A. Barr, C. Lester and P. Stephens, "m(T2) : The Truth behind the glamour," J. Phys. G **29**, 2343 (2003) [arXiv:hep-ph/0304226].

[7] W. S. Cho, K. Choi, Y. G. Kim and C. B. Park, "Gluino Stransverse Mass," Phys. Rev. Lett. **100**, 171801 (2008) [arXiv:0709.0288 [hep-ph]] and

[8] W. S. Cho, K. Choi, Y. G. Kim and C. B. Park, "Measuring superparticle masses at hadron collider using the transverse mass kink," JHEP **0802**, 035 (2008) [arXiv:0711.4526 [hep-ph]].

[9] B. Gripaios, "Transverse Observables and Mass Determination at Hadron Colliders," JHEP **0802**, 053 (2008) [arXiv:0709.2740 [hep-ph]];

[10] A. J. Barr, B. Gripaios and C. G. Lester, "Weighing Wimps with Kinks at Colliders: Invisible Particle Mass Measurements from Endpoints," JHEP **0802**, 014 (2008) [arXiv:0711.4008 [hep-ph]].

[11] A. J. Barr, B. Gripaios and C. G. Lester, "Transverse masses and kinematic constraints: from the boundary to the crease," JHEP **0911**, 096 (2009) [arXiv:0908.3779 [hep-ph]].

[12] C. Lester and A. Barr, "MTGEN : Mass scale measurements in pair-production at colliders," JHEP **0712**, 102 (2007) [arXiv:0708.1028 [hep-ph]].

[13] H. C. Cheng and Z. Han, "Minimal Kinematic Constraints and MT2," JHEP **0812**, 063 (2008) [arXiv:0810.5178 [hep-ph]].

[14] M. Burns, K. Kong, K. T. Matchev and M. Park, "Using Subsystem MT2 for Complete Mass Determinations in Decay Chains with Missing Energy at Hadron Colliders," JHEP **0903**, 143 (2009) [arXiv:0810.5576 [hep-ph]];

[15] P. Konar, K. Kong, K. T. Matchev and M. Park, "Superpartner Mass Measurement Technique Using 1d Orthogonal Decompositions Of The Cambridge Transverse Mass Variable M_{t2}," Phys. Rev. Lett. **105**, 051802 (2010) [arXiv:0910.3679 [hep-ph]];

[16] K. T. Matchev and M. Park, "A general method for determining the masses of semi-invisibly decaying particles at hadron colliders," arXiv:0910.1584 [hep-ph].

[17] P. Konar, K. Kong, K. T. Matchev and M. Park, "Dark Matter Particle Spectroscopy at the LHC: Generalizing MT2 to Asymmetric Event Topologies," JHEP **1004**, 086 (2010) [arXiv:0911.4126 [hep-ph]].

[18] M. M. Nojiri, Y. Shimizu, S. Okada and K. Kawagoe, "Inclusive transverse mass analysis for squark and gluino mass determination," JHEP **0806**, 035 (2008) [arXiv:0802.2412 [hep-ph]];

[19] M. M. Nojiri, K. Sakurai, Y. Shimizu and M. Takeuchi, "Handling jets + missing E_T channel using inclusive m_{T2}," JHEP **0810**, 100 (2008) [arXiv:0808.1094 [hep-ph]];

[20] W. S. Cho, W. Klemm and M. M. Nojiri, "Mass measurement in boosted decay systems at hadron colliders," arXiv:1008.0391 [hep-ph];

[21] M. M. Nojiri and K. Sakurai, "Controlling ISR in sparticle mass reconstruction," arXiv:1008.1813 [hep-ph].

[22] D. R. Tovey, "On measuring the masses of pair-produced semi-invisibly decaying particles at hadron colliders," JHEP **0804**, 034 (2008) [arXiv:0802.2879 [hep-ph]];

[23] G. Polesello and D. R. Tovey, "Supersymmetric particle mass measurement with the boost-corrected contransverse mass," JHEP **1003**, 030 (2010) [arXiv:0910.0174 [hep-ph]].

[24] W. S. Cho, J. E. Kim and J. H. Kim, "Amplification of endpoint structure for new particle mass measurement at the LHC," Phys. Rev. D **81**, 095010 (2010) [arXiv:0912.2354 [hep-ph]].

[25] A. J. Barr, C. Gwenlan, C. G. Lester and C. J. S. Young, "A comment on 'Amplification of endpoint structure for new particle mass measurement at the LHC'," arXiv:1006.2568 [hep-ex].

[26] M. Serna, "A short comparison between m_{T2} and m_{CT}," JHEP **0806**, 004 (2008) [arXiv:0804.3344 [hep-ph]].

[27] T. Cohen, E. Kuflik and K. M. Zurek, "Extracting the Dark Matter Mass from Single Stage Cascade Decays at the LHC," JHEP **1011**, 008 (2010) [arXiv:1003.2204 [hep-ph]].

[28] H. C. Cheng, J. F. Gunion, Z. Han, G. Marandella and B. McElrath, "Mass Determination in SUSY-like Events with Missing Energy," JHEP **0712**, 076 (2007) [arXiv:0707.0030 [hep-ph]].

[29] H. C. Cheng, D. Engelhardt, J. F. Gunion, Z. Han and B. McElrath, "Accurate Mass Determinations in Decay Chains with Missing Energy," Phys. Rev. Lett. **100**, 252001 (2008) [arXiv:0802.4290 [hep-ph]];

[30] H. C. Cheng, J. F. Gunion, Z. Han and B. McElrath, "Accurate Mass Determinations in Decay Chains with Missing Energy: II," Phys. Rev. D **80**, 035020 (2009) [arXiv:0905.1344 [hep-ph]];

[31] H. C. Cheng, Z. Han, I. W. Kim and L. T. Wang, "Missing Momentum Reconstruction and Spin Measurements at Hadron Colliders," arXiv:1008.0405 [hep-ph]; Y. Bai and H. C. Cheng, "Identifying Dark Matter Event Topologies at the LHC," arXiv:1012.1863 [hep-ph].

[32] M. Burns, K. Kong, K. T. Matchev and M. Park, "A General Method for Model-Independent Measurements of Particle Spins, Couplings and Mixing Angles in Cascade Decays with Missing Energy at Hadron Colliders," JHEP **0810**, 081 (2008) [arXiv:0808.2472 [hep-ph]].

[33] P. Konar, K. Kong and K. T. Matchev, "$\sqrt{\hat{s}}_{min}$: A Global inclusive variable for determining the mass scale of new physics in events with missing energy at hadron colliders," JHEP **0903**, 085 (2009) [arXiv:0812.1042 [hep-ph]];

[34] P. Konar, K. Kong, K. T. Matchev and M. Park, "RECO level $\sqrt{s}_{min}$ and subsystem $\sqrt{s}_{min}$: improved global inclusive variables for measuring the new physics mass scale in missing energy events at hadron colliders," arXiv:1006.0653 [hep-ph].

[35] M. M. Nojiri, K. Sakurai and B. R. Webber, "Reconstructing particle masses from pairs of decay chains," JHEP **1006**, 069 (2010) [arXiv:1005.2532 [hep-ph]].

[36] B. Webber, "Mass determination in sequential particle decay chains," JHEP **0909**, 124 (2009) [arXiv:0907.5307 [hep-ph]].

[37] T. Han, I. W. Kim and J. Song, "Kinematic Cusps: Determining the Missing Particle Mass at the LHC," arXiv:0906.5009 [hep-ph];

[38] I. W. Kim, "Algebraic Singularity Method for Mass Measurement with Missing Energy," Phys. Rev. Lett. **104**, 081601 (2010) [arXiv:0910.1149 [hep-ph]].

[39] D. R. Tovey, "Transverse mass and invariant mass observables for measuring the mass of a semi-invisibly decaying heavy particle," JHEP **1011**, 148 (2010) [arXiv:1008.3837 [hep-ph]].

[40] A. J. Barr and C. G. Lester, "A Review of the Mass Measurement Techniques proposed for the Large Hadron Collider," arXiv:1004.2732 [hep-ph].

[41] G. Jungman, M. Kamionkowski and K. Griest, "Supersymmetric dark matter," Phys. Rept. **267**, 195 (1996) [arXiv:hep-ph/9506380].

[42] H. S. Lee, "Lightest U-parity Particle (LUP) dark matter," Phys. Lett. B **663**, 255 (2008) [arXiv:0802.0506 [hep-ph]].

[43] H. C. Cheng and I. Low, "TeV symmetry and the little hierarchy problem," JHEP **0309**, 051 (2003) and

[44] H. C. Cheng and I. Low, "Little hierarchy, little Higgses, and a little symmetry," JHEP **0408**, 061 (2004) [arXiv:hep-ph/0405243].

[45] G. Servant and T. M. P. Tait, "Is the lightest Kaluza-Klein particle a viable dark matter candidate?," Nucl. Phys. B **650**, 391 (2003);

[46] H. C. Cheng, J. L. Feng and K. T. Matchev, "Kaluza-Klein dark matter," Phys. Rev. Lett. **89**, 211301 (2002) [arXiv:hep-ph/0207125].

[47] K. Agashe, A. Falkowski, I. Low and G. Servant, "KK Parity in Warped Extra Dimension," JHEP **0804**, 027 (2008).

[48] The ATLAS Collaboration, CERN-LHCC-99-015.

[49] The CMS Collaboration, J. Phys. G: Nucl. Part. Phys. 34 995-1579 (2007).

[50] D. G. E. Walker, "Dark Matter Stabilization Symmetries from Spontaneous Symmetry Breaking," arXiv:0907.3146 [hep-ph].

[51] K. Agashe and G. Servant, "Warped unification, proton stability and dark matter," Phys. Rev. Lett. **93**, 231805 (2004) [arXiv:hep-ph/0403143].

[52] K. Agashe and G. Servant, "Baryon number in warped GUTs: Model building and (dark matter related) phenomenology," JCAP **0502**, 002 (2005) [arXiv:hep-ph/0411254].

[53] E. Ma, "Z_3 Dark Matter and Two-Loop Neutrino Mass," Phys. Lett. B **662**, 49 (2008) [arXiv:0708.3371 [hep-ph]].

[54] K. Agashe, R. Franceschini and D. Kim, "A simple, yet subtle 'invariance' of two-body decay kinematics," arXiv:1209.0772 [hep-ph].

[55] Similar results appeared in the cosmic rays physics literature, see, for example, F. W. Stecker, "Cosmic gamma rays," *NASA Special Publication* **249** (1971) .

[56] E. Byckling and K. Kajantie, Particle Kinematics (John Wiley & Sons, 1973).

[57] D. J. Miller, P. Osland and A. R. Raklev, "Invariant mass distributions in cascade decays," JHEP **0603**, 034 (2006) [arXiv:hep-ph/0510356].

[58] S. Kraml and A. R. Raklev, "Same-sign top quarks as signature of light stops at the LHC," Phys. Rev. D **73**, 075002 (2006) [arXiv:hep-ph/0512284].

[59] L. T. Wang and I. Yavin, "Spin Measurements in Cascade Decays at the LHC," JHEP **0704**, 032 (2007) [arXiv:hep-ph/0605296].

[60] J. Alwall *et al.*, "MadGraph/MadEvent v4: The New Web Generation," JHEP **0709**, 028 (2007) [arXiv:0706.2334 [hep-ph]].

[61] W. Cho, D. Kim, K. Matchev and M. Park, to appear.

[62] Y. Bai and H. -C. Cheng, "Identifying Dark Matter Event Topologies at the LHC," JHEP **1106**, 021 (2011).

[63] M. Blanke, D. Curtin and M. Perelstein, "SUSY-Yukawa Sum Rule at the LHC," Phys. Rev. D **82**, 035020 (2010);

[64] A. Rajaraman and F. Yu, "A New Method for Resolving Combinatorial Ambiguities at Hadron Colliders," Phys. Lett. B **700**, 126 (2011);

[65] P. Baringer, K. Kong, M. McCaskey and D. Noonan, "Revisiting Combinatorial Ambiguities at Hadron Colliders with M_{T2}," JHEP **1110**, 101 (2011).

[66] I. Hinchliffe, F. Paige, M. Shapiro, J. Soderqvist and W. Yao, "Precision SUSY measurements at CERN LHC," Phys. Rev. D **55**, 5520 (1997);

[67] K. Matchev, F. Moortgat, L. Pape and M. Park, "Precise reconstruction of sparticle masses without ambiguities," JHEP **0908**, 104 (2009).

[68] A. J. Barr, B. Gripaios and C. G. Lester, "Measuring the Higgs boson mass in dileptonic W-boson decays at hadron colliders," JHEP **0907**, 072 (2009) [arXiv:0902.4864 [hep-ph]].

[69] K. M. Zurek, "Multi-Component Dark Matter," Phys. Rev. D **79**, 115002 (2009) [arXiv:0811.4429 [hep-ph]];

[70] F. Chen, J. M. Cline and A. R. Frey, "Nonabelian dark matter: models and constraints," Phys. Rev. D **80**, 083516 (2009) [arXiv:0907.4746 [hep-ph]];

[71] D. Feldman, Z. Liu, P. Nath and G. Peim, "Multicomponent Dark Matter in Supersymmetric Hidden Sector Extensions," Phys. Rev. D **81**, 095017 (2010) [arXiv:1004.0649 [hep-ph]];

[72] M. Cirelli and J. M. Cline, "Can multistate dark matter annihilation explain the high-energy cosmic ray lepton anomalies?," arXiv:1005.1779 [hep-ph].

[73] G. F. Giudice, B. Gripaios, R. Mahbubani, "Counting dark matter particles in LHC events," [arXiv:1108.1800 [hep-ph]].

[74] "Search for supersymmetry in final states with missing transverse energy and 0, 1, 2, 3, or at least 4 b-quark jets in 8 TeV pp collisions using the variable α_T," CMS Collaboration *CMS-PAS-SUS-12-028* (2012) .

[75] R. K. Ellis, W. J. Stirling, and B. Webber, "QCD and collider physics," *Camb.Monogr.Part.Phys.Nucl.Phys.Cosmol.* **8** (1996) 1–435.

[76] CMS Collaboration, "Search for supersymmetry in events with b-quark jets and missing transverse energy in pp collisions at 7 TeV," *ArXiv e-prints* (Aug., 2012) , arXiv:1208.4859 [hep-ex]

[77] J. Alwall, J. L. Feng, J. Kumar and S. Su, "B's with Direct Decays: Tevatron and LHC Discovery Prospects in the $b\bar{b}$ + MET Channel," Phys. Rev. D **84**, 074010 (2011) [arXiv:1107.2919 [hep-ph]].

[78] J. Alwall, M. Herquet, F. Maltoni, O. Mattelaer, and T. Stelzer, "MadGraph 5: going beyond," *Journal of High Energy Physics* **6** (June, 2011) 128, arXiv:1106.0522 [hep-ph].

[79] J. Pumplin, D. Stump, J. Huston, H. Lai, P. M. Nadolsky, *et al.*, "New generation of parton distributions with uncertainties from global QCD analysis," *JHEP* **0207** (2002) 012, arXiv:hep-ph/0201195 [hep-ph]

[80] CMS Collaboration, "Identification of b-quark jets with the CMS experiment," *ArXiv e-prints* (Nov., 2012) , arXiv:1211.4462 [hep-ex]

[81] M. Blanke, D. Curtin and M. Perelstein, "SUSY-Yukawa Sum Rule at the LHC," Phys. Rev. D **82**, 035020 (2010) [arXiv:1004.5350 [hep-ph]].

[82] D. Curtin, "Mixing It Up With MT2: Unbiased Mass Measurements at Hadron Colliders," arXiv:1112.1095 [hep-ph].